technische universität
dortmund

Dissertation

Spin Dynamics in Indirect Band-Gap Quantum Wells and Quantum Dots

submitted in partial fulfillment of the requirements for the degree of

Dr. rer. nat.

to the Faculty of Physics

TU Dortmund University, Germany

by

Janina Rautert

Dortmund, September 28, 2020

Accepted by the Faculty of Physics of the TU Dortmund University, Germany

Day of the oral examination: December 11, 2020

Examination board:
Prof. Dr. Dmitri R. Yakovlev
Prof. Dr. Dieter Suter
Prof. Dr. Frithjof Anders
JProf. Dr. Armin Lühr

Contents

Summary

In this thesis, semiconductor quantum wells (QWs) and quantum dots (QDs) with an indirect band gap in momentum space are investigated with regard to their fine structure and the related spin dynamics. Indirect nanostructures are being developed because of their very long recombination times, which make them interesting for spintronic applications. Here, the focus is on a fascinating but barley studied, quantum mechanical property: The absence of exchange interaction, which, despite the spatial proximity of electron and hole, is caused by their distance in momentum space.
Polarized photoluminescence measurements show that due to the lack of exchange interaction, the fine structures of indirect excitons in the studied GaAs/AlAs QW and (In,Al)As/AlAs QDs are fully degenerate. Depending on the ratio of the exciton recombination time and the spin relaxation time, different related effects are observed as spin dynamics between dark and bright states, optical orientation and the hyperfine interaction of the X electron with the nuclei. The comparison of experimental results with theoretical models reveals important structure parameters as the heavy-hole g factor, the spin relaxation time and the hyperfine constant of the X electron. Moreover, the impact of the high energetic direct state on the indirect QD excitons, which limits their optical orientation, is investigated.

Zusammenfassung

In dieser Arbeit werden Halbleiter-Quantentröge und Quantenpunkte (englisch: quantum wells and dots, QWs and QDs) mit einer indirekten Bandlücke im Impulsraum hinsichtlich ihrer Feinstruktur und den damit verbundenen Spin-Dynamiken untersucht. Indirekte Nanostrukturen werden aufgrund ihrer sehr langen Rekombinationszeiten entwickelt, die sie für spintronische Anwendungen interessant machen. Hier liegt der Fokus auf einer faszinierenden, aber kaum untersuchten quantenmechanischen Eigenschaft: Das Fehlen der Austauschwechselwirkung, die, trotz der räumlichen Nähe von Elektron und Loch, durch deren Abstand im Impulsraum verursacht wird.
Mittels polarisationsaufgelöster Messungen der Photolumineszenz wird gezeigt, dass die Feinstruktur der indirekten Exzitonen im GaAs/AlAs QW und in den (In,Al)As/AlAs QDs auf Grund der fehlenden Austauschwechselwirkung vollständig entartet ist. Abhängig vom Verhältnis der Exzitonenrekombinationszeit und der Spinrelaxationszeit werden verschiedene, damit zusammenhängende Effekte wie die Spin-Dynamik zwischen dunklen und hellen Zuständen, optische Orientierung und die Hyperfeinwechselwirkung des X-Elektrons mit den Kernen beobachtet. Vergleiche der experimentellen Ergebnisse mit theoretischen Modellen liefern wichtige Strukturparameter wie den Schwerloch-g-Faktor, die Spinrelaxationszeit und die Hyperfeinkonstante des X-Elektrons. Darüber hinaus wird der Einfluss des direkten Zustands auf die indirekten QD-Exzitonen untersucht, welcher unter anderem in der Begrenzung ihrer optischen Orientierung besteht.

1 Introduction

Quantum wells and quantum dots with an indirect band gap are interesting from the perspective of applied and basic physics. On the one hand, the enhanced spin lifetime might be attractive for future spintronic devices, on the other hand, the lack of electron-hole exchange interaction in nanostructures that are indirect in momentum space is a fascinating, but largely unexplored quantum mechanical effect. In the present work, the focus is on the investigation of the physical processes in these semiconductor heterostructures. However, history has shown that basic research and technology are interdependent and can therefore be considered equally important for the scientific progress.

In the past decades, semiconductors have had an impressive success story, thanks to their wide range of applications like detectors, light sources (diode, laser), integrated circuits, photovoltaics and data storage [1]. The investigation of semiconductors started already in the first half of the 19th century with independend experiments of T. J. Seebeck and M. Faraday, who discovered the thermal properties of semiconductors [2], [3]. About one hundret years later, the development of the band-structure theory was driven by F. Bloch, who described the movement of an electron in a periodic potential by a quantum mechanical wave function [4], and by R. Kronig and W. Penney with their potential model of a crystal [5]. The theoretical description of the field-effect transistor, proposed by J. E. Lilienfeld in 1925, lead to the fabrication of the first transistor in 1947 by W. Shockley, J. Bardeen and W. Brattain. The rapid development of transistors and related electronic devices is the foundation of our modern technology.
At about the same time of Lilienfelds invention, the second important property of the electron, apart from charge, was discovered: Spin. Prominent features of the spin are the polarization of electromagnetic radiation, the binary character of the electron spin and the Pauli exclusion principle [6]. With the concept of spin it is possible to explain for example the structure of the periodic table of elements or the magnetism of solids. Two practical applications of spin are the magnetic resonance imaging in medicine or the giant magneto-resistance effect for data storage. Nowadays, the focus is on the usage of the spin as information carrier in quantum bits or spin transistors on integrated circuit chips [7]. One major challenge of this field is a high storage time of the spin state, which is characterized by the spin lifetime time and the coherence or dephasing time.
The persistent trend of downsizing the dimensions of transistors leads to the improvement of semiconductor growth techniques and opened the door to a new field of research. Heterostructures like quantum wells (QWs), quantum wires and quantum dots (QDs) show interesting physics like the quantization of states and the 2D electron gas (in QWs) and also offer a wide range of applications [8]. Today, QWs are used for lasers, transistors, detectors and solar cells, QDs for diodes, displays, and single-photon sources, to mention only a few. Another application is the usage of electron spins in QDs as quantum bits [9]. Due to spatial confinement in all directions, the most important spin relaxation mechanisms are suppressed and theoretical calculations imply that the relaxation time in

QDs might reach milliseconds [10] [11]. However, the relativly short recombination time of several nanoseconds in direct QDs [12] can be a limiting factor for the spin lifetime. In this regard, T. S. Shamirzaev started to investigate QDs and QWs with an indirect band gap in momentum space in 2003 [13]. In these structures the direct recombination is forbidden, which can lead to extremely long recombination times up to hundreds of microseconds[14]. Since about 2011, the studies of indirect structures were expanded in collaboration with the 'Experimentelle Physik E2' group at the Technical University of Dortmund.

In this thesis, a GaAs/AlAs QW and an (In,Al)As/AlAs QD ensemble, both with indirect band gaps in momentum space, are investigated. The focus is on the spin dynamics and the effects caused by the lack of electron-hole exchange interaction.
Chapter 2 provides the theoretical background, which is necessary to follow the discussions of the experiments. This includes the term of quantization, the descriptions of the fine structure, the indirect band gap and the relevant spin interactions in QWs and QDs. Moreover, three theoretical models, which were developed for the description of the studied samples, are presented. These models cover the exciton recombination in the QD ensemble, the spin dynamics in the indirect QW and the hyperfine interaction of the indirect QD exciton.
Descriptions of the experimental setups and techniques are given in chapter 3. A particular focus is on the polarization measurements, since they are the basis of nearly all works presented in this thesis. The studied samples are introduced in chapter 4. In addition to the structural descriptions, background knowledge on previous research is imparted.
In chapter 5, the experimental results of the indirect GaAs/AlAs QW are presented. As the QW is also indirect in real space (type-II structure), the exciton recombination time is much longer than the spin relaxation time. As a result, it is possible to study the spin dynamics between optically dark and bright exciton spin states, which are energetically close to each other due to the lack of electron-hole exchange interaction. These spin dynamics are reflected in the dependencies of the circular and linear polarization degree from magnetic field, time and temperature. The comparison of the experimental results with the theoretical model reveals important structure parameters like the heavy-hole g factor and the spin relaxation time of the electron.
In chapter 6, the studies of the QD ensemble are described. This structure contains QDs with direct and indirect band gaps in momentum space. The transition between these two types of dots can be determined by the ΓX-mixing energy in the PL spectrum of the ensemble. This transition is also reflected in the spectral dependence of the exciton recombination time and the strong decrease of the electron-hole exchange splitting at this energy. The ensemble structure of the QD sample allows the targeted, resonant excitation of direct and indirect dots, which is used to study the optical orientation and alignment of the dots. The optical orientation of the exciton spin is reduced by different effects as the hyperfine interaction of the X electron with the nuclear spins. Finally, the spin relaxation time of the indirect exciton is measured under selective excitation.
Conclusions for both structures can be found in chapter 7. Since the number of measurements exceeded the scope of this work, some interesting but still incomplete studies are presented in the Outlook (chapter 8), which might encourage future experiments in order to complete the understanding of these structures.

2 Physical background

2.1 Carrier spins in quantum wells and quantum dots

2.1.1 Quantization

Quantum-mechanical effects, like the quantization of states and the wave nature of particles, become important when the mean free path of the particle becomes smaller than its de Broglie wavelength λ_B. For electrons (holes) in a semiconductor, λ_{dB} is given by

$$\lambda_{dB} = \frac{h}{p} = \frac{h}{\sqrt{3m^* k_B T}}, \tag{2.1}$$

where h is the Planck constant, p the momentum and m^* the effective mass of the electron (hole), k_B the Boltzmann constant and T the temperature [15]. At room temperature ($T = 300$ K), the effective mass of an electron in the conduction band of gallium arsenide (GaAs) is $0.063m_0$ and $0.023m_0$ in indium arsenide (InAs) [16], where m_0 is the free electron mass. Thus, the de Broglie wavelengths in these materials are 25 nm and 41 nm. In the fabrication of semiconductor heterostructures, the combination of materials with different band gaps, the so called 'band-gap engineering', is used to create potential walls which reduce the mean free path of the carriers below λ_{dB}. These nanostructures are characterized by the number of dimensions in which the size of the structure is smaller than λ_{dB}. Quantum wells (QWs) are 2-dimensional and quantum dots (QDs) are 0-dimensional objects.
The quantized energy levels of the carriers can be calculated by the 'particle in a box' model. For instance, in a QW with the thickness L_z, the electron (hole) is described by a wave function which fulfills the Schrödinger equation for a confining potential along the axis z (growth direction) with infinite potential walls. In this case, the energies are given by [15]

$$E_n = \frac{\hbar^2}{2m^*} \left(\frac{n\pi}{L_z} \right)^2, \tag{2.2}$$

where n is the number of the energy level. Note that electrons and holes are not necessarily confined in the same material, as it is the case for type-I heterostructures. In type-II structures, the ground states of electrons and holes are in adjacent layers. Descriptions of type-I and type-II heterostructures are given in section 2.2.

2.1.2 Exciton fine structure

The complex of an electron and a hole, bound by the Coulomb interaction, is an exciton. In a QW or QD, the quantized energy levels of the exciton usually experience further splittings, which are related to the spins of the carriers. Spin is the intrinsic angular momentum or magnetic moment of a particle in units of the reduced Planck constant

$\hbar$, which is usually omitted. Electrons have a spin of $s = \pm 1/2$ with the projections $m_\mathrm{s} = \pm 1/2$ along the z axis. In case of a valence-band electron, the spin of 1/2 is coupled with the orbital angular momentum $l = 1$ (due to the p-type wave function), resulting in the total angular momenta $j = 1/2$, with the projections $m_\mathrm{j} = \pm 1/2$, and $j = 3/2$ with $m_\mathrm{j} = \pm 1/2$ and $m_\mathrm{j} = \pm 3/2$. Optical transitions from the valance to the conduction band states can be induced by polarized light in compliance with the dipole selection rules: Circularly polarized light causes a change of $\Delta m = \pm 1$. For example, when the system is excited with σ^+ polarized light ($\Delta m = +1$), valence-band electrons with $m_\mathrm{j} = -3/2$ can be lifted to the conduction-band states with $m_\mathrm{s} = -1/2$ [1].
The excitation of an electron to the conduction band leaves behind an empty place in the valence band, a 'hole'. Therefore, the excitation with σ^+ polarized light, which removes an electron with $m_\mathrm{j} = -3/2$ from the valence band, can also be understood as the creation of a hole with $m_\mathrm{j} = +3/2$. A hole with $j = 3/2$ is a 'light' hole for $m_\mathrm{j} = \pm 1/2$ and a 'heavy' hole in case of $m_\mathrm{j} = \pm 3/2$. The two $j = 1/2$ states, or 'split-off' states, of the hole are shifted by Δ_so to higher energies. As it is $\Delta_\mathrm{so} = 0.334$ eV in GaAs and $\Delta_\mathrm{so} = 0.41$ eV in InAs [17], the split-off states are disregard in the following.
For an exciton, the spin states are given by the four different combinations of the electron and hole spin projections. In case of a heavy hole, the possible exciton states are $m = (m_\mathrm{s} + m_\mathrm{j}) \in \{+1, -1, +2, -2\}$. Since the selection rules for dipoles allow only optical transitions with $\Delta m = \pm 1$, the exciton states with $|m| = 1$ are optically active ('bright') and the states with $|m| = 2$ are optically inactive ('dark').

Further considerations about the spin states are strongly related to the symmetry of the host structure. The different symmetries can be described with the help of their point groups. QWs with a symmetric potential, grown on a substrate with Zincblende structure along the [001] axis, as well as high symmetric QDs are assigned to the D_{2d} point group, while QWs and QDs with the lower symmetry are described by the C_{2v} point group [18], [19]. In the D_{2d} symmetry, the heavy- and light-hole states split (at the Γ point) and the heavy hole becomes the ground state of the valence band [20]. When the symmetry of the structure is lowered from D_{2d} to C_{2v}, the heavy- and light-hole states mix [21].
For an exciton, the multiplet of states is split into an energetic fine structure by the electron-hole exchange interaction, which couples the spins of the two carriers, and by the Zeeman effect in a magnetic field. Details about the electron-hole exchange interaction and the Zeeman effect can be found in Sec. 2.1.3. A schematic presentation of the fine-structure splitting is given in Fig. 2.1, which is adapted from Ref. [18]. It is important to note that the mixing of heavy and light holes is neglected here. In the absence of exchange interaction ($E_\mathrm{exch} = 0$) and magnetic fields ($B = 0$), the four exciton spin states are degenerated. However, in a QW or QD with C_{2v} symmetry, the isotropic part of the exchange interaction splits the bright ($|\pm 1\rangle$) and dark states ($|\pm 2\rangle$) by an energy of δ_0 and the dark substates get mixed and split by δ_2. In addition, the anisotropic exchange interaction causes the mixing of the bright states and splits the two linearly polarized superpositions, $|X\rangle = \frac{1}{\sqrt{2}}(|+1\rangle + |-1\rangle)$ and $|Y\rangle = \frac{1}{i\sqrt{2}}(|+1\rangle - |-1\rangle)$, by δ_1. (In the following, the prefactors $1/((i)\sqrt{2})$ are omitted.) In case of the higher D_{2d} symmetry, the bright exciton states remain degenerated, which is indicated by the blue lines.

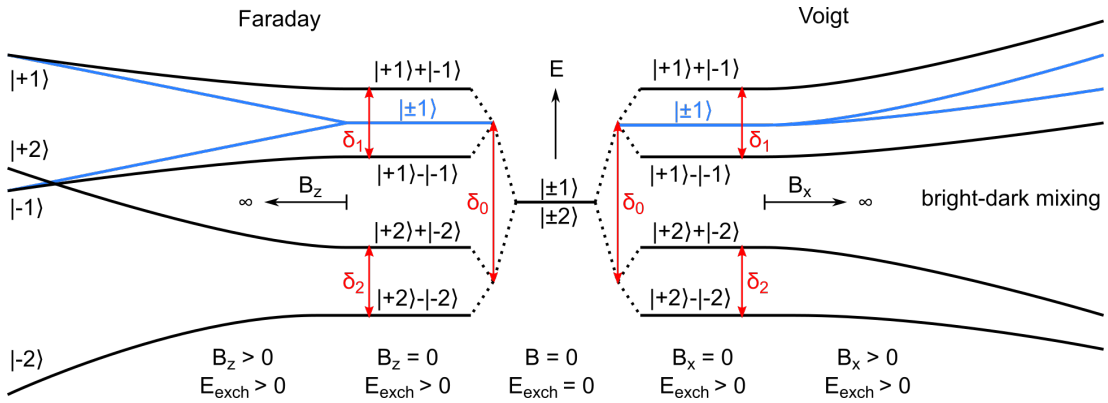

Figure 2.1: Schematic presentation of the exciton fine structure for a QW or QD with C_{2v} symmetry in a magnetic Faraday (B_z) or Voigt (B_x) field. The blue lines show the bright states in case of the higher D_{2d} symmetry. The prefactors $1/((i)\sqrt{2})$ of the mixed states are omitted. Without electron-hole exchange interaction ($E_{\mathrm{exch}} = 0$) all spin states are degenerated. The red arrows indicate the electron-hole exchange splittings of bright (δ_1) and dark states (δ_2) and the splitting between them (δ_0). For $B_z \to \infty$ the mixed exciton spin states become pure, while for $B_x \to \infty$ bright and dark states are completely mixed. The relations of the g factors are $g_z^{(\mathrm{h})} > g_z^{(\mathrm{e})} > 0$ and $g_x^{(\mathrm{e})} > g_x^{(\mathrm{h})} > 0$. Dashed lines are guides for the eye. Adapted from Ref. [18].

Further splitting of the exciton spin states is caused by the Zeeman effect. A magnetic field $\boldsymbol{B} = (B_x, B_y, B_z)$ splits the two degenerated spin states of the electron (e) and the hole (h) in dependence of the carrier g factor. As a result the four related exciton (Ex) spin states split as well. The Zeeman effect for the carrier $i \in \{\mathrm{e}, \mathrm{h}, \mathrm{Ex}\}$ is described most generally by the Hamiltonian [22]

$$H_{\mathrm{Z}}^{(i)} = \frac{1}{2}\mu_{\mathrm{B}} \sum_{\alpha\beta} g_{\alpha\beta}^{(i)} \sigma_{\alpha}^{(i)} B_{\beta}, \tag{2.3}$$

where μ_{B} is the Bohr magneton, α, $\beta = x, y, z$ are Cartesian coordinates, $g_{\alpha,\beta}$ are the components of the g-factor tensor and σ_{α} are the Pauli matrices of the carrier.
The energies $E_{\pm1}$ and $E_{\pm2}$, given by Eq. (2.4) and Eq. (2.5), describe the bright and dark exciton spin states of the fine structure, taking into account the electron-hole exchange interaction and Zeeman splitting. The mixing of light- and heavy-hole states, which can be relevant for C_{2v} QWs, is disregarded here. $E_{\pm1}$ and $E_{\pm2}$ strongly depend on the g factor tensors of electron and hole. For simplicity, it is assumed that only the diagonal tensor components with $\alpha = \beta$ contribute. Here, the relations $g_z^{(\mathrm{h})} > g_z^{(\mathrm{e})} > 0$ and $g_x^{(\mathrm{e})} > g_x^{(\mathrm{h})} > 0$ are applied, which describe the relevant case for the presented studies. In

Faraday geometry (see Sec. 3.1), the energies for the C_{2v} point group are given by [18]

$$E_{\pm 1} = +\frac{1}{2}\left(\delta_0 \pm \sqrt{\delta_1^2 + \left[\mu_\mathrm{B}\left(g_z^{(\mathrm{e})} - g_z^{(\mathrm{h})}\right) B_z\right]^2}\right), \tag{2.4}$$

$$E_{\pm 2} = -\frac{1}{2}\left(\delta_0 \pm \sqrt{\delta_2^2 + \left[\mu_\mathrm{B}\left(g_z^{(\mathrm{e})} + g_z^{(\mathrm{h})}\right) B_z\right]^2}\right). \tag{2.5}$$

The exciton energies for the D_{2d} point group can be obtained by setting $\delta_1 = 0$. In a strong longitudinal magnetic field, $B_z \to \infty$, the Zeeman splitting of the bright (dark) exciton states overcomes the electron-hole exchange splitting δ_1 (δ_2) and the mixing of the states is suppressed. As a result, the pure, circularly polarized excitons states are formed: $|{+1}\rangle \pm |{-1}\rangle \to |{\pm 1}\rangle$ ($|{+2}\rangle \pm |{-2}\rangle \to |{\pm 2}\rangle$). This is illustrated on the left side of Fig. 2.1. When a transverse magnetic field $B_{x,y} > 0$ is applied, the rotational symmetry in the xy plane is lost, which leads to the mixing of bright and dark states. In this case, the dark states become optically active. For $B_{x,y} \to \infty$, the four exciton states are given by $|{+1}\rangle \pm |{-1}\rangle + |{+2}\rangle \pm |{-2}\rangle$ (prefactors omitted) and have the same oscillator strength. The exact energies and states of the fine structure in a transverse field are not relevant for this thesis. They can be looked up in Ref. [18].

2.1.3 Spin interactions and characteristic times

The control of spins, including creation, manipulation and detection, requires knowledge about the interactions of the spins with their environment during the exciton lifetime / recombination time τ_r. The interactions relevant for this thesis are given in Fig. 2.2, which is adapted from Ref. [22].
Electromagnetic radiation is the key element which provides access to the spin systems of a semiconductor. In the context of this thesis, the absorption of circularly polarized $\sigma^\pm$ light is connected with the creation (injection) of $|{\pm 1}\rangle$ excitons and the detection of $\sigma^\pm$ polarized light is usually caused by the recombination of $|{\pm 1}\rangle$ excitons. The time between creation and recombination is the exciton recombination time τ_r, which is determined by the overlap of the wave functions of electron and hole. Within τ_r, the average spin of the excitons can relax towards its equilibrium state. The speed of this relaxation is characterized by the spin relaxation time τ_s and is determined by the respective spin relaxation mechanisms of the system. Thus, the total spin of the system is lost after the spin lifetime T_s, limited by the exciton recombination time and the spin relaxation time [6]

$$\frac{1}{T_\mathrm{s}} = \frac{1}{\tau_\mathrm{s}} + \frac{1}{\tau_\mathrm{r}}. \tag{2.6}$$

The polarization degree ρ characterizes the state of a spin system. If all spins are aligned along z, the polarization degree is 1 (or 100%), if the spins are aligned randomly, ρ is 0 (0%). Under steady-state conditions, the polarization degree is determined by the ratio of τ_r and τ_s

$$\rho = \frac{\rho_\mathrm{i}}{1 + \tau_\mathrm{r}/\tau_\mathrm{s}}, \tag{2.7}$$

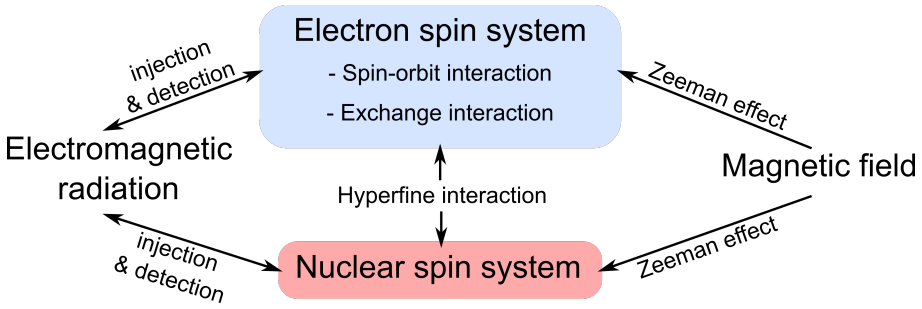

Figure 2.2: Relevant interactions within the electron spin system and with external systems: Electron spins are coupeld to the angular momentum via spin-orbit interaction and to other electron spins via exchange interaction. Electron spins and nuclear spins interact via hyperfine interaction. In a magnetic field, both spin systems are influenced by the Zeeman effect. Injection and detection of spin polarization can be realized by optical excitation and spectroscopy. Adapted from Ref. [22]

where ρ_i is the initial polarization degree of the studied state [6].
Since the spin of a carrier causes a magnetic moment, an external magnetic field B induces the spin precession around the field direction with the Larmor frequency $\Omega = \mu_\mathrm{B} g B/\hbar$, where μ_B is the Bohr magneton, g the g factor of the carrier and $\hbar$ the reduced Planck constant. In case of a transverse magnetic field ($B \perp z$), the precession of the spins causes the decrease of the spin polarization, if the Larmor precession is faster than the spin lifetime T_s. This effect is known as Hanle effect and the magnetic field dependence of the polarization degree is given by

$$\rho(B) = \frac{\rho(0)}{1 + (\Omega T_\mathrm{s})^2}, \tag{2.8}$$

where $\rho(0)$ is the steady-state polarization in absence of a magnetic field [6], see Eq. (2.7). Moreover, a longitudinal field ($B \parallel z$) lifts the degeneracy of the two electron (and hole) spin states. The splitting is given by $\Delta E_\mathrm{Z} = \hbar\Omega$ and is known as the Zeeman effect, see also Eq. (2.3).

As mentioned above, the spin relaxation time τ_s can be limited by several different mechanisms, see Fig. 2.2. Spin transfer from the electron to the nuclear system, known as dynamical nuclear polarization, is mediated by the hyperfine interaction. In this thesis, only the effect of the nuclear spin system on the electron spin is considered. Effects on or within the nuclear spin system are disregarded. A single electron usually interacts with a high number of nuclear spins that act as an effective magnetic field, the Overhauser field B_N [22]. As a result, the total spin of the electron system can be fully or partially depolarized by the nuclear fields. This effect can be counteracted by a longitudinal magnetic field. The corresponding dependence of the circular polarization degree from the field strength is the so called 'polarization recovery curve' (PRC). In Sec. 2.5, the hyperfine interaction between the nuclear system and an electron in the X valley of the conduction band is discussed in more detail.
Within the electron-spin system, the spin-orbit interaction and the exchange interaction need to be considered. Two effective spin-relaxation mechanisms, which base on the spin-

orbit interaction, are the Elliott-Yafet and the Dyakonov-Perel mechanisms. As a result, the spin-orbit coupling is the main channel for spin relaxation in bulk semiconductors or heterostructures with at least one axis for the electron movement. In QDs, however, the spatial confinement in all three dimensions leads to the suppression of these mechanisms, which prolongs the spin-relaxation time. [6].
The exchange interaction is a quantum mechanical effect, which appears when identical particles interact with each other. It can be described by a correction term, the exchange term, in the potential that describes the interaction between the particles. The exchange interaction between electrons is the result of the Coulomb interaction and the Pauli principle [23]. In case of excitons, it couples the spins of electron and hole and leads to the splitting and mixing of the four exciton spin states, as it is described in Sec. 2.1.2. Moreover, it can cause efficient spin relaxation by the Bir-Aronov-Pikus mechanism [22].

Another characteristic parameter of the temporal spin evolution is the decoherence time τ_d, which describes the time until the polarization of a single excited state is out of phase with respect to the exciting wave [24]. Since a change of phase can occur from any scattering event, decoherence times can be quite short. However, they range between several picoseconds to several microseconds [6]. The dephasing time, which describes the decay of phase for an ensemble of spins, is considerably shorter than the decoherence time.
The conservation of both the optically induced spin orientation and its phase are major tasks in the field of spintronic.

2.2 Direct and indirect band gaps

In semiconductor physics, the expressions 'direct' and 'indirect' can be understood in two different ways. In both cases, they describe the type of the band gap and the way electron and hole recombine. A transition from the valence band to the conduction band and reverse can be direct or indirect in real and / or in momentum space [25]. In the latter case, direct transitions are characterized by the absorption / emission of energy in form of photons, while indirect transitions require also the change of momentum. In real space, an indirect transition occurs if electrons and holes are spatially separated. The terms 'direct' and 'indirect' can also be applied for the exciton state or the structure (QW or QD) that provides the (in)direct band gap as ground state. Expressions that are used in this context are '(in)direct QD / QW' and '(in)direct exciton'.
The indirect band gap in momentum space is a property of the respective semiconductor material itself, while the indirect band in real space is the result of a heterostructure made of at least two different materials. However, in both cases the mismatch of the electron and hole wave functions leads to the increase of exciton recombination time. The two different situations are discussed in the following, starting with indirect band gaps in momentum space.

Electrons in a fully occupied valence band of a semiconductor are bound to the ions of the crystal. When an electron is excited from the valence band to the conduction band, it can move within the crystal lattice, where it experiences a periodic potential caused by the ions of the material. This is taken into account by the effective mass m^* of the electron (hole) in the dispersion relation of the energy E. Since m^* depends on the

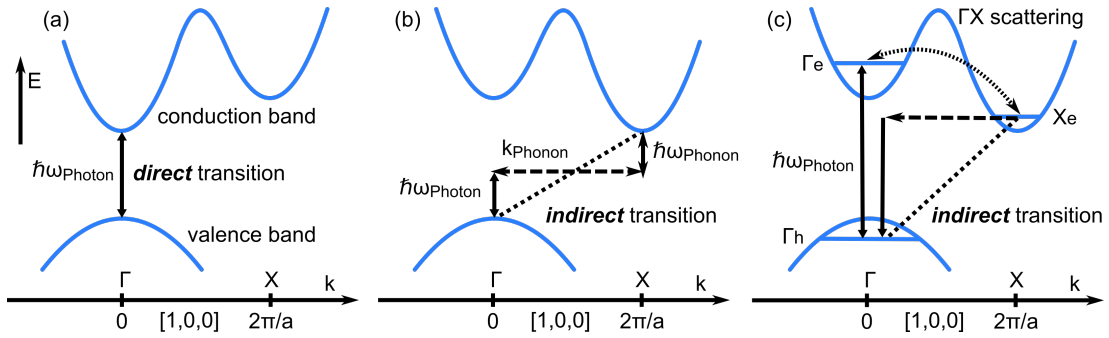

Figure 2.3: Schematic representations of the conduction and valence bands of a semiconductor in momentum space. The valence band minimum is at the Γ point ($k = 0$). **(a)** Direct band-gap semiconductor with the lowest point of the conduction band at the Γ point. **(b)** Indirect band-gap semiconductor with the lowest point of the conduction band at the X point ($k = 2\pi/a$). The transition requires the absorption / emission of a photon and a phonon with suitable energies and momentum. **(c)** Excitation and recombination of electron (e) and hole (h) in a QD with an indirect band gap in momentum space. Horizontal lines represent the quantized energy levels of the nanostructure. The electron is optically excited to the Γ valley and can scatter to the X valley (dotted arrow) via phonon interaction. The change of momentum, which is necessary for the indirect recombination, is caused by scattering at the heterointerface (dashed arrow) [26], [27].

direction of the electron wave vector $\boldsymbol{k}$, it is usually a tensor. In a 3-dimensional crystal, the effective-mass tensor of a carrier is given by

$$\left(\frac{1}{m^*}\right)_{ij} = \frac{1}{\hbar^2}\frac{\partial^2 E}{\partial k_i \partial k_j}, \tag{2.9}$$

with $i, j = x, y, z$ [1].
Since the electron (wave) scatters at the ions of the lattice, the allowed directions of $\boldsymbol{k}$ are limited by the Laue equations, which describe the conditions for constructive interference of the scattered wave. A geometrical description of the Laue condition in momentum space is the boundary of the so called Brillouin zone, which is determined by the structure of the crystal lattice. The Brillouin zone has a number of important symmetry points, like the Γ point at $\boldsymbol{k} = (0, 0, 0)$ and the six X points at $(0, 0, \pm k)$, $(0, \pm k, 0)$ and $(\pm k, 0, 0)$ with $k = 2\pi/a$ for an fcc lattice with lattice constant a. Close to these symmetry points, the dispersion relations of the conduction and valence bands can be described by the quadratic functions

$$E_{\mathrm{CB}}(k) = E_{\mathrm{g}} + \frac{\hbar^2 k^2}{2m_{\mathrm{e}}^*}, \quad E_{\mathrm{VB}}(k) = \frac{\hbar^2 k^2}{2m_{\mathrm{h}}^*}, \tag{2.10}$$

where E_{g} is the energy gap, or band gap, between the conduction (CB) and the valence (VB) band. m_{e}^* and m_{h}^* are the effective masses of the electron and the hole.
The full description of the energy dispersion for a semiconductor material is called band structure. A strongly simplified representation is given in Fig. 2.3. Depending on the energy minima, 'valleys', in the band structure, the transitions between the conduction

and the valence band can be direct or indirect in momentum space. A direct transition is shown in Fig. 2.3 (a). Since the minima of both bands are at the Γ point, the transition requires an energy of $\Delta E \geq E_\mathrm{g}$, which can be provided by a photon with $\hbar\omega_\mathrm{Photon} \geq E_\mathrm{g}$, while the momentum remains unchanged. The corresponding exciton, formed by an electron in the Γ valley of the conduction band and a hole in the Γ valley of the valence band, is a direct exciton or a 'Γ exciton'.
The situation is different when the minimum of the conduction band is located at the X point, see (b). Such a band gap is called indirect. In this case, the difference in momentum needs to be compensated by another particle, e.g. by a phonon, which can absorb / deliver energy and momentum. This condition leads to the increase of the recombination time from about one nanosecond to several microseconds [28], [29]. The photoluminescence (PL), emitted during the indirect recombination process, has a reduced photon energy and is called phonon-assisted line or phonon replica. The exciton, formed by an electron in the X valley of the conduction band and a hole in the Γ valley of the valence band, is an indirect exciton or 'X exciton'. For the studied structures, the growth axis z of the semiconductor materials is parallel to the (001) direction of the crystals. The two corresponding X valleys, for which $\boldsymbol{k}$ is aligned parallel and antiparallel to the z direction, are denoted as X_z valleys, while the perpendicularly (in the sample plane) aligned valleys are the X_x and the X_y valleys.
The mismatch of the electron and hole wave functions in heterostructures with indirect band gaps in momemtum space does not only lead to the reduction of the exciton recombination rate but also to the suppression of the electron-hole exchange interaction [30]. The experimental verification of this theoretically predicted effect and the investigation of its impact on the spin dynamics are major tasks of this thesis.

The previous considerations concerning indirect band gaps in momentum space are restricted to bulk semiconductors. In a quantized system, k is no longer a good quantum number but is smeared out to a range of Δk. According to Heisenberg's uncertainty principle, it is $\Delta k \Delta x > 1/2$, where Δx is the size of the heterostructure. Thus, for a hole in the Γ valley and an electron in the X valley, the indirect character of the transition is lost for $\Delta k > 2\pi/a$. This inequality is satisfied for $\Delta x < a/(4\pi)$, i.e. for a heterostructure that is smaller than the lattice constant itself. Therefore, it can be stated that the indirect band gap is preserved in the studied QW and QD structures.
Figure 2.3 (c) shows the schematic band structure of a QD with an indirect band gap in momentum space. The quantized energy levels Γ_e, Γ_h and X_e of electron and hole are indicated by the horizontal blue lines. (Their extension in k space is only for illustration and should not be related to the energy dispersion.) When the electron is excited to the Γ valley by a photon, it can either recombine directly with the hole or relax to the X valley by gaining momentum via phonon scattering (dotted arrow). The recombination process can be described as the virtual electron transition (horizontal, dashed arrow) from the X to the Γ valley with the simultaneous, spin-conserving emission of the excess momentum, resulting in the optical transition at the Γ point [31], [32], [33]. For (In,Al)As/AlAs QDs it was found that loss of momentum occurs mainly due to scattering at the heterointerface [26], [27] instead of scattering with phonons. Therefore the PL spectrum of the X-exciton transition shows only one intense feature, a zero-phonon (ZP) line, also known as no-phonon (NP) line. For the studied QW structures, however, the loss of momentum is caused by phonon scattering (see Sec. 4.1.1), as it is illustrated in Fig. 2.3 (b).

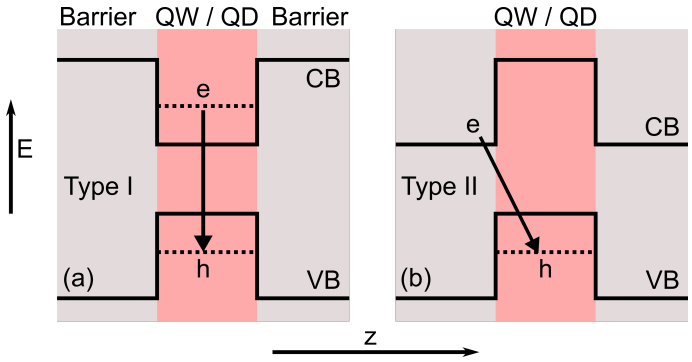

Figure 2.4: Real-space band structure of a QW / QD with **(a)** type-I alignment and **(b)** type-II alignment. In (a) the energy minima of the valence (VB) and the conduction band (CB) are located in the same material. The recombination of electron (e) and hole (h) is direct in real space. In (b) the valence and conduction band minima are in adjacent materials. The recombination of the separated carriers is indirect in real space.

An indirect band gap in real space can be created in a heterostructure with at least two different semiconductor materials. The energies of the valence and conduction bands are determined by the electron affinities of the material. For adjacent layers, three different situations can occur. If the energies of the valence and the conduction bands of the first material are both within the band gap of the second material, one speaks of a type-I heterostructure. If only one band, valence or conduction band, of the first material is within the band gap of the second material, one speaks of a type-II heterostructure. A type-III or broken-gap structure is obtained when the band gaps of the two materials do not overlap at all.
A scheme of the structures that are relevant for this thesis, type-I and type-II, is given in Fig. 2.4. In (a) a type-I structure with two type-I interfaces is shown. For this band lineup, electrons and holes will localize in the middle layer, while the two outer layers serve as barriers for the carriers. Since the wave functions of electron and hole overlap in real space, the recombination is direct. Figure 2.4 (b) shows a type-II structure. Here, electrons and holes localize in adjacent materials, which reduces the overlap of the carrier wave functions. As a result, the exciton recombination time can be increased up to several hundreds of nanoseconds [34].

Note: In order to avoid confusion in the following sections, the term 'indirect' will be used only in context with transitions that are indirect in momentum space.

2.3 Recombination in a quantum dot ensemble

The recombination of excitons in QDs, especially in single QDs, is often described by a monoexponential decay of the PL intensity shortly after the laser pulse. However, a closer look reveals that usually conditions like the redistribution between dark and bright exciton states or Coulomb correlations lead to a nonexponential decay [35], [36], [37]. In an ensemble of QDs the differences in size, shape and composition of the dots lead to a

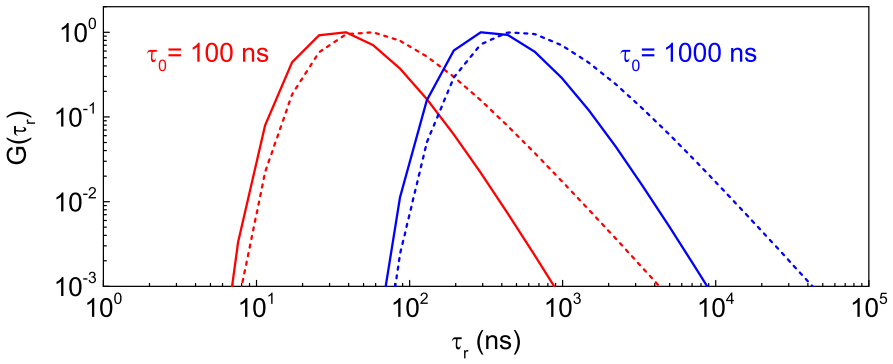

Figure 2.5: Distribution function $G(\tau_r)$ of the exciton recombination time τ_r, as it is defined in Eq. (2.13), with $\tau_0 = 100$ ns (red curves) and $\tau_0 = 1000$ ns (blue curves). The parameter γ, which determines the width of $G(\tau_r)$, is changed from 3 (solid curves) to 2 (dashed curves).

distribution $G(\tau_r)$ of the exciton recombination time τ_r, which causes the nonexponential decay [38]. This is also the case for the studied indirect (In,Al)As/AlAs QDs, as it is shown in Ref. [13], [39]. In these dots, the recombination is mediated by the scattering of electrons at the QD surface. It is demonstrated in the appendix of Ref. [28] that the recombination time of the nonexponential decay is proportional to

$$\tau_r \propto \exp(d/a + d/L), \tag{2.11}$$

where a is the lattice constant and L the QD height. The roughness of this heterointerface is characterized by the thickness d of the diffused layer between the (In,Al)As QD and the AlAs matrix.

The width of the distribution $G(\tau_r)$ can be seen as the dispersion of τ_r, which is given by the square root of τ_r. Thus, the study of the distribution function $G(\tau_r)$ can provide interesting information about the nature of the heterointerface. For example, for several QDs with the same size (energy), the narrowing of $G(\tau_r)$ should be connected with the broadening of the diffused layer [28]. In principle, nonexponential decay in QDs is well described by a 'stretched' exponential function, $I(t) = I_0 \cdot \exp(-(t/\tau_r)^\beta)$ [40] (derived from the Kohlrausch function [41]), where I is the PL intensity at the time t, I_0 the initial intensity, τ_r the time constant and β qualitatively characterizes the width of $G(\tau_r)$.

However, as the exact derivation of $G(\tau_r)$ from β is difficult, another approach was developed to describe the recombination in indirect QDs. That approach is pesented in Ref. [28], where the PL intensity is given by the integral over the monoexponential function weighted with the distribution function $G(\tau_r)$:

$$I(t) = \int_0^\infty G(\tau_r) \exp\left(-\frac{t}{\tau_r}\right) \mathrm{d}\tau_r. \tag{2.12}$$

The distribution function is determined phenomenologically to the nonsymmetrical expression

$$G(\tau_\mathrm{r}) = \frac{C}{\tau_\mathrm{r}^\gamma} \exp\left(-\frac{\tau_0}{\tau_\mathrm{r}}\right), \tag{2.13}$$

where C is a constant and τ_0 the characteristic time of the recombination process. The parameter γ is inversely proportional to the effective width of $G(\tau_\mathrm{r})$. Figure 2.5 shows four different examples of $G(\tau_\mathrm{r})$ for $\tau_0 = 100$ ns (red) and $\tau_0 = 1000$ ns (blue) with $\gamma = 3$ (solid lines) and $\gamma = 2$ (dashed lines). The constant C is arbitrarily chosen to 10^{-8}.

2.4 Spin dynamics in an indirect GaAs/AlAs quantum well

In this section, the kinetic spin model is presented, which was developed to describe the spin dynamics in the indirect GaAs/AlAs QW that is studied in this thesis. The model was introduced in Ref. [31] to describe the magnetic field and temperature dependencies of the PL intensity and is expanded in Refs. [42] and [43] to describe the circular and linear polarization degree. In the two following subsections, the most important aspects of this model are summarized.

2.4.1 Circular polarization dynamics

In a QW with an indirect band gap in momentum space, the exciton ground state is formed by an electron in the X valley and a heavy hole in the Γ valley. (For the result of the model it does not matter whether the electron is located in the X_x, the X_y or the X_z valley.) The exciton spin states arise from the electron spin states labeled with $s = |\pm 1/2\rangle$ and the heavy-hole spin states $j = |\pm 3/2\rangle$. As the electron-hole exchange interaction is suppressed for indirect excitons [30], [44], the spin Hamiltonian consists only of the Zeeman terms for the electron and the heavy hole. For a magnetic field $\boldsymbol{B}$ with an arbitrary direction, the spin Hamiltonian is given by

$$\hat{\mathcal{H}} = g_\mathrm{e}\mu_\mathrm{B}\boldsymbol{B}\cdot\hat{s} + \frac{g_\mathrm{hh}}{3}\mu_\mathrm{B}B_z\hat{J}_z, \tag{2.14}$$

with the Bohr magneton μ_B, the electron spin operator $\hat{s}$ and the z component of the heavy-hole angular-momentum $\hat{J}_z$. Here, it is assumed that the g factor of the X electron, g_e, is isotropic, since the wide band gap at the X point weakens the spin-orbit contribution to the g factor [45], [46], [47]. Therefore, it is $g_\mathrm{e} = g_x^{(\mathrm{e})} = g_z^{(\mathrm{e})}$. In contrast, the heavy hole g factor is highly anisotropic and the in-plane components of the heavy hole g factor can be neglected [48]. Thus, it is $g_\mathrm{hh} = g_z^{(\mathrm{hh})}$ and $g_x^{(\mathrm{hh})} = 0$ and only the B_z component of the magnetic field is relevant for the Zeeman energy of the hole.
In Faraday geometry ($\boldsymbol{B} \parallel z$), the spin states of the exciton quadruplet are given by $|s = \pm 1/2, j = \pm 3/2\rangle$ and the selection rules for the radiative recombination of the X exciton are equal to the rules for the Γ exciton:

$$\begin{aligned} \text{Bright:}\ & |+1/2, -3/2\rangle \text{ active in } \sigma^-, \\ & |-1/2, +3/2\rangle \text{ active in } \sigma^+, \\ \text{Dark:}\ & |+1/2, +3/2\rangle \text{ and } |-1/2, -3/2\rangle\,. \end{aligned} \tag{2.15}$$

The energies of the four spin levels are given by:

$$E_{|\pm 1/2,\pm 3/2\rangle} = {}^1\!/_2(\pm g_\mathrm{e} \pm g_\mathrm{hh})\mu_\mathrm{B} B_z. \tag{2.16}$$

In case of $B_z = 0$, the spin levels of the exciton are degenerated. For $B_z > 0$, the degeneracy is lifted by the Zeeman splitting and the energetic order of the spin levels depends on the g factors of electron and hole.
If the magnetic field is tilted from Faraday geometry, the transverse contribution of the field destroys the rotational symmetry of the system, which causes the mixing of the two basic electron spin states (heavy-hole spin states) and thus, the mixing of bright and dark exciton states [18]. For the sake of simplicity, it is assumed that the hole spins are not affected by the transverse field due to their small in-plane g factors [48]. The mixing of the basic electron spin states in a magnetic field, tilted by the angle θ from Faraday geometry, can be described by

$$\begin{aligned} |+1/2\rangle_B &= C\,|1/2\rangle_z + D\,|-1/2\rangle_z\,, \\ |-1/2\rangle_B &= -D\,|1/2\rangle_z + C\,|-1/2\rangle_z\,, \end{aligned} \tag{2.17}$$

with the coefficients $C = \cos(\theta/2)$ and $D = \sin(\theta/2)$.
In Voigt geometry ($\theta = 90°$), it is $C = D$ and the contributions of the basic spin states are the same for both mixed electron spin states. Therefore, all four exciton states $|sj_z\rangle = |s\rangle_\mathbf{B}\,|j_z\rangle_z$ become radiative and show the same oscillator strength. According to Eq. (2.14), the energy levels of the four exciton spin states form two degenerated doublets with:

$$E_{|\pm 1/2\rangle_B} = \pm 1/2 g_\mathrm{e}\mu_\mathrm{B} B, \quad \text{with } B \perp z. \tag{2.18}$$

For an arbitrary geometry ($0° < \theta < 90°$), the system is in a transition stage between the described situations for Faraday and Voigt geometry. Thus, there are two 'brighter' states with higher oscillator strength and two 'darker' states with lower oscillator strength.

The σ^+ and σ^- polarized PL intensities I_+ and I_-, emitted by the four exciton levels, are given by the occupancies f_{sj} of these levels, the radiative recombination time τ_rad and the coefficients C and D:

$$I_{+/-} \propto \frac{C^2}{\tau_\mathrm{rad}} f_{-+/+-} + \frac{D^2}{\tau_\mathrm{rad}} f_{++/--}. \tag{2.19}$$

For simplification, the notation for the exciton spin state $|\pm 1/2, \pm 3/2\rangle$ is sometimes shortened to $|\pm\pm\rangle$. The circular polarization degree ρ_c is then defined by the occupancy numbers of all four spin states:

$$\rho_\mathrm{c} = \frac{C^2(f_{-+} - f_{+-}) + D^2(f_{++} - f_{--})}{C^2(f_{-+} + f_{+-}) + D^2(f_{++} + f_{--})}. \tag{2.20}$$

The occupancies f_{sj} are determined by the rates $W_{s,s'}$ and $W_{j,j'}$ of the electron and heavy-hole spin flips $s' \to s$ and $j' \to j$, the radiative and nonradiative recombination times, τ_rad and τ_nr, the coefficients C and D and the generation rate G_{sj} for excitons in

the $|s, j\rangle$ state. They can be expressed by the kinetic equations

$$\frac{df_{sj}}{dt} + (W_{\bar{s},s} + W_{\bar{j},j})f_{sj} - W_{s,\bar{s}}f_{\bar{s}j} - W_{j,\bar{j}}f_{s\bar{j}} + Rf_{sj} = G_{sj}(t), \tag{2.21}$$

where R is the recombination operator

$$\begin{aligned} Rf_{-+/+-} &= \left(\frac{1}{\tau_{\mathrm{nr}}} + \frac{C^2}{\tau_{\mathrm{rad}}}\right) f_{-+/+-}, \\ Rf_{++/--} &= \left(\frac{1}{\tau_{\mathrm{nr}}} + \frac{D^2}{\tau_{\mathrm{rad}}}\right) f_{++/--}. \end{aligned} \tag{2.22}$$

In case of Zeeman splitting, the spin-flip rates of the electron (heavy hole), from the higher to the lower energy level and vice versa, differ by the Boltzmann factor α (β). Therefore, the individual rates depend from the energetic order of the states, which in turn depends from the g factors of electron and heavy hole. For $g_{\mathrm{hh}} \geq 0$ and $g_{\mathrm{e}} \geq 0$, which is the case for the studied GaAs QW, the ratios of the rates are given by

$$\begin{aligned} W_{\frac{1}{2},-\frac{1}{2}} &= W_{-\frac{1}{2},\frac{1}{2}} \underbrace{\exp\left(-\frac{g_{\mathrm{e}}\mu_{\mathrm{B}}B}{k_{\mathrm{B}}T}\right)}_{\alpha}, \\ W_{\frac{3}{2},-\frac{3}{2}} &= W_{-\frac{3}{2},\frac{3}{2}} \underbrace{\exp\left(-\frac{g_{\mathrm{hh}}\mu_{\mathrm{B}}B_z}{k_{\mathrm{B}}T}\right)}_{\beta}, \end{aligned} \tag{2.23}$$

where k_{B} is the Boltzmann constant and T the temperature. Thus, the spin-flip rate from the lower to the higher energy level can approach zero in a strong magnetic field B_z and / or in case of a low temperature. In the following, the spin-flip rates downwards in energy are denoted as $W_{-\frac{1}{2},\frac{1}{2}} \equiv w_{\mathrm{e}}$ and $W_{-\frac{3}{2},\frac{3}{2}} \equiv w_{\mathrm{h}}$ and the spin-flip rates upwards in energy are given by $W_{\frac{1}{2},-\frac{1}{2}} \equiv \alpha w_{\mathrm{e}}$ and $W_{\frac{3}{2},-\frac{3}{2}} \equiv \beta w_{\mathrm{h}}$. The spin-flip rates are inversely proportional to the spin-relaxation times of electron and heavy hole

$$w_{\mathrm{e}} = \tau_{\mathrm{s,e}}^{-1} \quad \text{and} \quad w_{\mathrm{h}} = \tau_{\mathrm{s,hh}}^{-1}. \tag{2.24}$$

For the sake of simplicity, it is assumed that the spin-relaxation times are independent of the temperature and the strength of the magnetic field. Indeed, their power-law dependencies [49], [50], [51] are weak compared to the exponential dependence of the Boltzmann factors. In analogy to (2.24), the radiative and nonradiative recombination times are expressed as the recombination rates

$$w = \tau_{\mathrm{rad}}^{-1} \quad \text{and} \quad w' = \tau_{\mathrm{nr}}^{-1}. \tag{2.25}$$

The kinetic equations in (2.21) can be simplified in special cases: For steady-state experiments it is $df_{sj_z}/dt = 0$. With non-resonant excitation all spin levels are excited equally, therefore the generation rate is $G_{sj_z} = G$. In Faraday geometry it is $C = 1$ and $D = 0$, while it is $C^2 = D^2 = 1/2$ for Voigt geometry. The analytical solutions for steady-state excitation with equal generation rates in all four spin states and an arbitrary magnetic

field direction are presented below. The occupancies are given by

$$\begin{aligned} f_{--} &= \frac{G + w_\mathrm{e} f_{+-} + w_\mathrm{h} f_{-+}}{\tilde{w}' + \alpha w_\mathrm{e} + \beta w_\mathrm{h}}, \quad f_{-+} = \frac{(w_{+-} + \beta W)\tilde{G}_{-+} + \beta W \tilde{G}_{+-}}{w_{-+}w_{+-} + (w_{+-}\alpha + w_{+-}\beta)W}, \\ f_{++} &= \frac{G + \alpha w_\mathrm{e} f_{-+} + \beta w_\mathrm{h} f_{+-}}{\tilde{w}' + w_\mathrm{e} + w_\mathrm{h}}, \quad f_{+-} = \frac{(w_{-+} + \alpha W)\tilde{G}_{+-} + \alpha W \tilde{G}_{-+}}{w_{-+}w_{+-} + (w_{+-}\alpha + w_{+-}\beta)W}, \end{aligned} \tag{2.26}$$

with

$$\tilde{w}' = w' + D^2 w \quad \text{and} \quad \tilde{w} = (C^2 - D^2)w + w', \tag{2.27}$$

and

$$\begin{aligned} w_{-+} &= \tilde{w} + \tilde{w}' \left(1 + \frac{\alpha w_\mathrm{e}}{\tilde{w}' + w_\mathrm{e} + w_\mathrm{h}} + \frac{w_\mathrm{h}}{\tilde{w}' + \alpha w_\mathrm{e} + \beta w_\mathrm{h}}\right), \\ w_{+-} &= \tilde{w} + \tilde{w}' \left(1 + \frac{w_\mathrm{e}}{\tilde{w}' + \alpha w_\mathrm{e} + \beta w_\mathrm{h}} + \frac{\beta w_\mathrm{h}}{\tilde{w}' + w_\mathrm{e} + w_\mathrm{h}}\right), \\ W &= w_\mathrm{e} w_\mathrm{h} \left(1 + \frac{1}{\tilde{w}' + \alpha w_\mathrm{e} + \beta w_\mathrm{h}} + \frac{1}{\tilde{w}' + w_\mathrm{e} + w_\mathrm{h}}\right), \end{aligned} \tag{2.28}$$

and the effective generation rates

$$\begin{aligned} \tilde{G}_{+-} &= G \left(1 + \frac{\alpha w_\mathrm{e}}{\tilde{w}' + \alpha w_\mathrm{e} + \beta w_\mathrm{h}} + \frac{w_\mathrm{h}}{\tilde{w}' + w_\mathrm{e} + w_\mathrm{h}}\right), \\ \tilde{G}_{-+} &= G \left(1 + \frac{w_\mathrm{e}}{\tilde{w}' + w_\mathrm{e} + w_\mathrm{h}} + \frac{\beta w_\mathrm{h}}{\tilde{w}' + \alpha w_\mathrm{e} + \beta w_\mathrm{h}}\right). \end{aligned} \tag{2.29}$$

The model can be extended by allowing small deviations from the selection rules described in (2.15). They can be caused by a symmetry reduction from the D_{2d} to the C_{2v} point group, which leads to the mixing of heavy- and light-hole states. As a result, the two bright states become active both in the σ^+ and the σ^- polarization. Thus, the symmetry reduction causes the decrease of the circular polarization degree by the factor ξ. Another reason for the deviation from the selection rules can be the simultaneity of a spin-flip and a recombination process, both triggered by a phonon. In this case the dark states become active and Eq. (2.20) is rewitten to

$$\rho_\mathrm{c} = \xi \frac{f_{-+} - f_{+-} + C_\mathrm{d}(f_{--} - f_{++})}{f_{-+} + f_{+-} + C_\mathrm{d}(f_{--} + f_{++})}, \tag{2.30}$$

for $\theta = 0°$ (Faraday geometry). Here, the factor C_d takes into account that a fraction of excitons in the $|{--}\rangle$ state recombines under emission of σ^+ polarized light and excitons in the $|{++}\rangle$ state can recombine under emission of σ^- polarized light.

2.4.2 Linear polarization dynamics

In a QW, nonequivalent interfaces and strain lead to a symmetry reduction from the D_{2d} to the C_{2v} point group [45], [22], which causes the mixing of heavy- and light-hole states [52], [21], [53]. The mixing repeals the isotropy of the in-plane orbital Bloch functions $|X\rangle$ and $|Y\rangle$ at the valence band maximum, which leads to the emission of

linear polarized light in the (xy) set of axes [54], [55]. In the following, this intrinsic linear polarization is referred to as ρ_{int}. The heavy-hole light-hole mixing also leads to a finite in-plane g factor of the heavy hole [6], which lifts the degeneracy of the hole sublevels with $j = \pm 3/2$ in a transverse magnetic field. Moreover, the application of the transverse magnetic field mixes not only the electron- but also the hole-spin states. As a result, the $|{+}{+}\rangle$ and $|{-}{-}\rangle$ states become vertically polarized and the $|{+}{-}\rangle$ and $|{-}{+}\rangle$ states become horizontally polarized.
The kinetic equations (2.21), describing the occupancies of the indirect exciton spin levels, can also be applied for the calculation of the field-induced linear polarization degree. To take into account the intrinsic polarization ρ_{int}, the recombination operator R must be rewritten to

$$Rf_{++/--} = \left(\frac{1+\rho_{\mathrm{int}}}{2\tau_{\mathrm{rad}}} + \frac{1}{\tau_{\mathrm{nr}}}\right) f_{++/--}, \tag{2.31}$$

$$Rf_{+-/-+} = \left(\frac{1-\rho_{\mathrm{int}}}{2\tau_{\mathrm{rad}}} + \frac{1}{\tau_{\mathrm{nr}}}\right) f_{+-/-+}, \tag{2.32}$$

and the linear polarization degree, measured in the (xy) axes set, is given by

$$\rho_{\mathrm{l}} = \frac{(1+\rho_{\mathrm{int}})(f_{++}+f_{--}) - (1-\rho_{\mathrm{int}})(f_{+-}+f_{-+})}{(1+\rho_{\mathrm{int}})(f_{++}+f_{--}) + (1-\rho_{\mathrm{int}})(f_{+-}+f_{-+})}. \tag{2.33}$$

In principle, the dynamics of the linear polarization degree can be obtained by calculating Eq. (2.33) with the time-depended solutions $f_{sj}(t)$ of the kinetic equations (2.21) for pulsed excitation $G(t)$. In addition, a simplified model is introduced in which the linear polarization degree is described by

$$\rho_{\mathrm{l}}(t) = 4 s_{\mathrm{e}}(t) s_{\mathrm{h}}(t), \tag{2.34}$$

with s_i as the mean spin component of the electron ($i = \mathrm{e}$) / hole ($i = \mathrm{h}$). In the following, the hole states $J_z = \pm 3/2$ are given by the pseudospin states $j = \pm 1/2$. Therefore, s_{e} and s_{h} both range between $+1/2$ and $-1/2$. The temporal development of the mean spin $s_i(t)$ from the initial mean spin s_i^0 to the thermal spin polarization $\langle s_i \rangle$ is determined by the effective spin relaxation time $\tilde{\tau}_{s,i}$ and given by:

$$s_i(t) = \left(s_i^0 - \langle s_i \rangle\right) e^{-t/\tilde{\tau}_{\mathrm{s},i}} + \langle s_i \rangle. \tag{2.35}$$

Thus, the dynamics of the linear polarization degree can be described by

$$\rho_{\mathrm{l}}(t) = 4\left[\left(s_{\mathrm{e}}^0 - \langle s_{\mathrm{e}} \rangle\right) e^{-t/\tilde{\tau}_{\mathrm{s,e}}} + \langle s_{\mathrm{e}} \rangle\right]\left[\left(s_{\mathrm{h}}^0 - \langle s_{\mathrm{h}} \rangle\right) e^{-t/\tilde{\tau}_{\mathrm{s,h}}} + \langle s_{\mathrm{h}} \rangle\right]. \tag{2.36}$$

The initial mean spin s_i^0 can arise during the energy relaxation process of electrons and holes directly after their generation. It is given by

$$s_i^0 = -\frac{1}{2}\tanh\left(\frac{\rho_i^0 \Delta_i}{2 k_{\mathrm{B}} T}\right), \tag{2.37}$$

where p_i^0 is the initial spin polarization and Δ_i is the Zeeman splitting of the electron / hole levels. The thermal spin polarization $\langle s_i \rangle$, which sets in for long delay times after the generation, is defined by

$$\langle s_i \rangle = -\frac{1}{2} \tanh\left(\frac{\Delta_i}{2k_\mathrm{B}T}\right), \tag{2.38}$$

and the effective spin relaxation time $\tilde{\tau}_{s,i}$ of the electron / hole is given by the sum of the spin-flip rates to the lower and the higher spin levels

$$\frac{1}{\tilde{\tau}_{\mathrm{s},i}} = \sum_{m=\pm 1/2} W^{(i)}_{m,\bar{m}}. \tag{2.39}$$

In case of an intrinsic linear polarization ρ_int, the dynamics of the linear polarization degree can be approximated by

$$\tilde{\rho}_\mathrm{l}(t) \approx \frac{\rho_\mathrm{l}(t) + \rho_\mathrm{int}}{1 + \rho_\mathrm{int}\rho_\mathrm{l}(t)}. \tag{2.40}$$

2.5 Hyperfine interaction with the X electron

The hyperfine interaction is the interaction between the spins of charge carriers and the spins of the nuclei. In QDs it is the most important channel for carrier-spin relaxation, since the spin-orbit interaction is weak for the localized carriers [6]. Moreover, the coupling between the charge carrier and the nucleus is enhanced by the localization, which leads to a stronger interaction. The strength of the interaction can be described by the hyperfine coupling constant A, which depends on the wave function of the carrier at the nucleus. For Γ electrons, with s type wave functions, these values are well known. In contrast, there are no such values for X electrons up to now. Moreover, the investigation of the hyperfine interaction in the X valley is interesting, since the related wave function deviates from the pure s type [56].
In Ref. [57], the hyperfine coupling constant A is calculated for X electrons in the vicinity of In, Al and As atoms. Moreover, a model is introduced, which describes the experimental PRC and Hanle curves for the case of anisotropic hyperfine interaction. The underlying theory is summarized in this section.

In general, the hyperfine interaction between a charge carrier and a nucleus is described by the following Hamiltonian [58]:

$$\mathcal{H}_\mathrm{hf} = 2\mu_\mathrm{B}\mu_I \mathbf{I}\left[\frac{8\pi}{3}\mathbf{s}\delta(\mathbf{r}) + \frac{\mathbf{l}}{r^3} - \frac{\mathbf{s}}{r^3} + 3\frac{\mathbf{r}\,(\mathbf{sr})}{r^5}\right], \tag{2.41}$$

with the Bohr magneton μ_B, the magnetic moment of the nucleus $\mu_I = g_I\mu_\mathrm{N}$ (where g_I is the g factor and μ_N the nuclear magneton), the nuclear spin $\boldsymbol{I}$, the electron spin $\mathbf{s}$, the vector between the nucleus and the electron $\mathbf{r}$ and the angular momentum $\hbar\mathbf{l} = \mathbf{r} \times \mathbf{p}$ with the linear momentum $\mathbf{p}$. The main contribution to the hyperfine interaction is delivered by the Fermi contact interaction, which is represented by the first term of the Hamiltonian. However, this term only contributes if the probability density at $r = 0$

is non-zero, which is only the case for s-type wave functions. The three other terms describe the dipole-dipole interaction, which depends on the distance between the carrier and the nucleus. Since the hyperfine interaction is short range, cross contributions from neighbor atoms can be neglected [59].
For the studied case of a X electron in a (In,Al)As QD it is assumed that the three valleys, X_x, X_y and X_z, are split from each other and their mixing is negligible [60]. Moreover, the large band gap at the X point leads to a weak spin-orbit interaction [47]. The shape of the electron Bloch wave function is determined by symmetry considerations, which depend on the type of the nucleus. For the In and Al cations (c) and the As anion (a) the functions are derived from the Supplemental Material of Ref. [61]. For the X_z electron they are given by

$$\Psi_c(\mathbf{r}) = \alpha_P \mathcal{P}_z(\mathbf{r}) + \alpha_T \mathcal{D}_{xy}, \tag{2.42a}$$

$$\Psi_a = \alpha_S \mathcal{S}(\mathbf{r}) + \alpha_D \mathcal{D}_{z^2}. \tag{2.42b}$$

$\mathcal{S}(\mathbf{r})$, $\mathcal{P}_i(\mathbf{r})$ (with $i = x, y, z$) and $\mathcal{D}_i(\mathbf{r})$ (with $i = xy, yz, xz, x^2 - y^2, z^2$) are products of radial functions and tesseral harmonics, which refer to the s, p and d types of the atomic orbitals. The coefficients α_S, α_P, α_D and α_T are real. For the X_x and the X_y electrons the corresponding wave functions are obtained from (2.42) by rotating the coordinate system.
For X_z-valley electron, the Hamiltonian can now be rewritten to

$$\mathcal{H}_{\mathrm{hf}} = A_{\mathrm{n}}^{\perp}(I_x s_x + I_y s_y) + A_{\mathrm{n}}^{\parallel} I_z s_z. \tag{2.43}$$

The hyperfine coupling constants $A_{\mathrm{n}}^{\perp}$ and $A_{\mathrm{n}}^{\parallel}$, for the axes perpendicular and parallel to the valley, depend on the coefficients α_S, α_P, α_D and α_T. The index n labels the different nuclei In, Al and As. In the following, the focus will be on the As atoms, since the $\mathcal{S}(\mathbf{r})$ function contributes only for the electrons at these atoms. $A_{\mathrm{As}}^{\perp}$ and $A_{\mathrm{As}}^{\parallel}$ are given by

$$A_{\mathrm{As}}^{\perp} = (25.7\alpha_S^2 - 3.2\alpha_D^2 - 1.4\alpha_S\alpha_D)A_0, \tag{2.44a}$$

$$A_{\mathrm{As}}^{\parallel} = (25.7\alpha_S^2 + 6.4\alpha_D^2 + 2.7\alpha_S\alpha_D)A_0, \tag{2.44b}$$

The coefficients are calculated by density-functional theory (DFT) with the WIEN2k package [62] to $\alpha_S = 0.50$ and $\alpha_D = 0.63$ for AlAs and $\alpha_S = 0.49$ and $\alpha_D = 0.41$ for InAs [57]. A_0 is a constant. Although it can be seen that the main contribution is caused by the Fermi contact interaction in the s shell, the weaker dipole-dipole interaction in the d shell leads to a distinct anisotropy of the hyperfine interaction, which is given by

$$\varepsilon = A_{\mathrm{As}}^{\perp}/A_{\mathrm{As}}^{\parallel}. \tag{2.45}$$

For the X valley in an $In_{0.7}Al_{0.3}As$ alloy, it is $A_{\mathrm{As}}^{\perp} = 5.19A_0$, $A_{\mathrm{As}}^{\parallel} = 8.33A_0$ and $\varepsilon = 0.62$. An analogous calculation can be performed for a Γ electron at the As atom. Since its wave function is mainly of the s type, the hyperfine coupling constant is given by $A_{\mathrm{As}}^{\Gamma} = 25.7\alpha_S^2 A_0$. DFT calculations yield $\alpha_S = 0.76$ for AlAs and $\alpha_S = 0.70$ for InAs.

For the $In_{0.7}Al_{0.3}As$ alloy it is $A^{\Gamma}_{As} = 13.25A_0$. Thus, for the Γ electron, the hyperfine coupling with the As nuclei is about 1.6 to 2.6 times stronger than for the X electron. In experiments A^{Γ}_{As} was determined to 43.5 μeV [63]. Thus, it is $A_0 = 3.3$ μeV and for the X electron $A^{\perp}_{As} = 17.0$ μeV and $A^{\parallel}_{As} = 27.3$ μeV are expected.

In principle, the hyperfine coupling of an electron and a nucleus causes the Lamor precession of the electron spin around the direction of the nuclear spin and the precession of the nuclear spin around the hyperfine field of the electron. In a QD, the electron interacts with large number of nuclei, whose spin directions fluctuate randomly. When integrated over a long period of time, the average magnetic field of the nuclei is zero. However, on small time scales (ns range) the fluctuations lead to an effective nuclear magnetic field B_N with random magnitude and direction. The distribution of B_N follows a Gaussian function with the center at

$$B_N = \frac{A^{\parallel}_{As}}{g_e \mu_B} \sqrt{\frac{I(I+1)}{3}\frac{V_0}{V}}. \tag{2.46}$$

Here, g_e is the electron g factor, I is the nuclear spin, V_0 is the volume of the primitive cell and V is the QD volume. Note that B_N is the strength of the nuclear field along the direction of the respective X_α valley with $\alpha = x, y, z$. The variance of the nuclear field is given by

$$\langle (B^{\alpha}_N)^2 \rangle = \Delta^2_\alpha B^2_N, \tag{2.47}$$

with $\Delta^2_\alpha = A^{\alpha}_{As}/A^{\parallel}_{As}$.
The precession of the electron around the nuclear field is $\sqrt{N}$ times faster than the precession of the nuclei around the electron spin, when N is the number of nuclei that are involved in the interaction. For $N \gg 1$, the fluctuations of the nuclear field can be considered as 'frozen' for the electron [64]. If the exciton relaxation time is much longer than the precession of the electron spin around the direction of the total magnetic field $\boldsymbol{B}^* = \boldsymbol{B} + \boldsymbol{B}_N$, the projection of the spin on the z axis is reduced to

$$\rho_z = \rho_0 \left\langle \cos^2\theta \right\rangle = \rho_0 \left\langle \frac{B^{*2}_z}{B^{*2}_x + B^{*2}_y + B^{*2}_z} \right\rangle = \rho_0 \left\langle \frac{b^2_z}{b^2_x + b^2_y + b^2_z} \right\rangle, \tag{2.48}$$

where ρ_0 is the spin polarization without nuclear fields, θ the angle between the total magnetic field and the z axis and $\boldsymbol{b} \equiv \boldsymbol{B}^*/B_N$. Equation (2.48) shows that an external magnetic field ($B > B_N$), directed along the z axis, can stabilize the spin polarization ($\rho_z = \rho_0$). The dependency $\rho_z(B_z)$ is the 'polarization recovery curve' (PRC). In contrast, a magnetic field along the x (or y) axis can lead to the complete suppression of the spin polarization ($\rho_z = 0$), the well known Hanle effect. The related dependency $\rho_z(B_x)$ is the Hanle curve.
In an ensemble of QDs, strength and direction of B_N vary from dot to dot. The integration of ρ_z over the Gaussian distribution leads to

$$\rho_z(B/B_N) = \frac{\rho_0}{\sqrt{8\pi^3}\Delta_x\Delta_y\Delta_z} \iiint \mathrm{e}^{\beta} \cdot \frac{b^2_z}{b^2_x + b^2_y + b^2_z} \mathrm{d}b_x \mathrm{d}b_y \mathrm{d}b_z, \tag{2.49}$$

with

$$\beta = \begin{cases} -\dfrac{b_x^2}{2\Delta_x^2} - \dfrac{b_y^2}{2\Delta_y^2} - \dfrac{(b_z - B/B_\mathrm{N})^2}{2\Delta_z^2}, & \text{for } B \parallel z, \\ -\dfrac{(b_x - B/B_\mathrm{N})^2}{2\Delta_x^2} - \dfrac{b_y^2}{2\Delta_y^2} - \dfrac{b_z^2}{2\Delta_z^2}, & \text{for } B \parallel x. \end{cases}$$

The numeric solution of Eq. (2.49) describes the PRC for $B \parallel z$ and the Hanle curve for $B \parallel x$. Note that the half widths at half maximum (HWHM) of the polarization curves, $B_{1/2}$, are not equal to B_N but it is [65]

$$B_\mathrm{N} = B_{1/2}/(2\varepsilon). \tag{2.50}$$

3 Experimental Details

All experiments presented in this work are based on the optical excitation of excitons and the detection of the photoluminescence (PL), which is emitted during their subsequent recombination. The basic structure of the PL setup consists of a laser, which is focused on a sample in a cryostat, a lens to collect and collimate the PL, a second lens to focus the PL on the slit of a monochromator and a detector, which transforms the PL intensity into an electrical signal. More specific setups allow to measure the PL intensity in dependence of spectral energy, excitation energy, temperature, magnetic field strength and angle, polarization, and, in case of pulsed excitation, in dependence of time.
The experiments can be described by four different categories, which are presented in Sec. 3.1. Since a large part of this work deals with the circular and linear polarization degree of excitons, the required measurement techniques are explained independently from the surrounding setups in Sec. 3.2. Then the different setups that were used for this work are described. Here, it makes sense to differentiate between macro- (Sec. 3.3) and microscopic experiments (Sec. 3.4), as switching between these two methods requires the most changes. Steady-state and time-resolved methods are discussed for both types of experiments.

3.1 Basic experimental categories

In order to distinguish between different types of experiments, it is useful consider the following cases:

1) Macroscopic and microscopic measurements: With one exception, all experiments in the present work are macroscopic, which means that they can be performed without the help of microscopic tools. In these measurements, the diameter of the laser spot and the position of the studied area on the sample are not relevant for the results. However, for the microscopic measurements, presented in Section 6.4.2, these parameters are very crucial and must be controllable in the micrometer range. The microscopic technique is described in section 3.4.

2) Nonresonant and resonant / selective excitation: Resonant excitation means that the photon energy of the laser beam is equal to the energy gap of the studied transition, while the nonresonant excitation is connected with the energy relaxation from the excited to the studied energy level. As it is demonstrated in Sec. 4.1.2 and Sec. 4.2.1, the QW and the QD layers of the studied samples are embedded between two 20-nm-thick AlAs layers, which serve as energetic barriers with a band gap of about 2.30 eV. For an effective, non-resonant excitation, a photon energy above this barrier is chosen, usually 3.49 eV. In case of the (In,Al)As/AlAs QD ensemble, with a broad distribution of QD sizes, it is possible and useful to excite a fraction of dots resonantly with a photon energy between 1.52 eV (GaAs substrate) and 2.30 eV (AlAs barrier). However, for excitation

energies above the ΓX transition energy $E_{\Gamma X}$, the resonant excitation of the direct exciton is accompanied by the energy relaxation of the electron from the Γ to the X valley. Therefore, the excitation of the X exciton is not resonant and the expression 'resonant excitation' is changed to 'selective excitation' as it is possible to select the size of the QDs via the excitation energy.

3) Steady-state and time-resolved experiments: In general, a system is in a steady state if the parameters that describe or influence the state are time independent. A parameter that describes the state of a QD is, for example, the PL intensity, and one influencing parameter is the ambient temperature. In a steady-state experiment, all influencing parameters are kept constant during the measurement and it is assumed that the measured parameter is constant too. The measurement can be repeated for different values of an influencing parameter. If the laser intensity is constant during the measurement, one speaks of continuous-wave (cw) excitation. However, it should be noted that steady-state experiments are also possible with pulsed excitation if the PL intensity is averaged over a period that is much longer than the time between two laser pulses.
In a time-resolved experiment, an influencing parameter is changed while a descriptive parameter is measured at successive times after the change. In the time-resolved experiments presented in this thesis, the changed parameter is the laser intensity, realized by pulsed excitation. The time-resolved measurement of the PL intensity enables the determination of the exciton recombination time.

4) Faraday and Voigt geometry: The direction of the magnetic field B with respect to the sample growth axis z is an important parameter in spin physics. Therefore, some expressions for the alignment need to be introduced. It is assumed that the exciting light beam is always parallel to z. In the so-called 'Faraday geometry', the direction of B is parallel to z ($B \parallel z$). In this case, the perpendicular components of B to z are zero and it is $B = B_z$. The angle θ between B and z is zero. One also speaks of a 'longitudinal' field. In 'Voigt geometry', the direction of B is perpendicular to z ($B \perp z$). In this case, the parallel component B_z is zero and it is either $B = B_x$ or $B = B_y$. The angle θ between B and z is 90°. One also speaks of a 'transverse' field. Thus, the equivalent expressions are:

Faraday geometry, $B \parallel z$, $B_{\parallel}$, $B = B_z$, $\theta = 0°$, longitudinal field
and
Voigt geometry, $B \perp z$, $B_{\perp}$, $B = B_{x,y}$, $\theta = 90°$, transverse field

Magnetic field directions that differ from the Faraday or Voigt geometry are described by the angle θ between B and z.

3.2 Polarization measurements

3.2.1 Polarized light

This section summarizes basic (textbook) knowledge about polarized light and its detection. A detailed description of the topic can be found in Ref. [66].

Light, propagating along an axis z, is circularly polarized if the vector of the electrical field E is rotating with constant amplitude and frequency around z. The two possible rotation directions define the two types of circularly polarized light: σ^+ and σ^-. Linearly polarized light is characterized by an E vector with an oscillating amplitude along a fixed axis, which is perpendicular to z. Elliptical polarization is a mixture of circular and linear polarization, while unpolarized light shows no periodical behavior of the E vector.
Polarized light can always be decomposed into two components with perpendicular E vectors. First, the two directions perpendicular to the z axis are defined as x and y axes. The rotating E vector of circular polarized light can be decomposed into two perpendicular vectors E_x and E_y with equal amplitudes, which are oscillating along x and y with a phase shift of $\pi/2$ (90°) to each other. Linear polarized light, with an E vector oscillating along a random but fixed direction, can be decomposed into two beams with perpendicular E vectors. The amplitudes of E_x and E_y can be different but they are oscillating in phase.

The polarization degree of light can be determined with the help of wave plates and Glan-Thompson prisms. These optical devices are made of a birefringent (double refracting) material, such as quartz, in which the refractive index of light depends on the direction of the E vector with respect to the optical axis of the material. When a light beam is propagating along this optical axis it exhibits no double refraction, since the E vector is always perpendicular to the optical axis. The index of refraction for this 'ordinary' beam is n_o. However, when the light beam is not parallel to the optical axis, there are usually two components of the light: One with a perpendicular and one with a parallel E vector to the optical axis. The latter is the 'extraordinary' beam, which exhibits a refractive index of n_e instead of n_o. The different indices lead to different velocities inside the material and thus to a phase shift of the components. Moreover, the two components can split into different directions if the beam hits the surface under an angle. Phase shift and splitting depend on the thickness of the birefringent material.
In wave plates, the optical axis is parallel to the two main surfaces of the plate. For a quarter-wave plate, the thickness of the material is chosen so that the phase shift between the ordinary and the extraordinary component is equal to $\pi/2$. In case of a half-wave plate the phase shift is π. It is now defined that the wave plate is in the 0° position when the optical axis is aligned along the y direction. When a circular polarized light beam passes a quarter-wave plate, which is in the 0° position, the E_y vector experiences a phase shift of $\pi/2$ and is now in phase with the E_x vector. The transmitted light is linear polarized and E is oscillating along the diagonal between x and y. E can be aligned along the x or y axis by rotating the quarter-wave plate to $+45°$ or $-45°$, depending on the type of circular polarized light.
When a linear polarized light beam, with $E_x = E_y$ (diagonal), passes a half-wave plate, which is in the 0° position, the E_y vector experiences a phase shift of π. Thus, the diagonally oscillating vector E is rotated by 90°. Generally, an angle of φ between the optical axis of the half-wave plate and the direction of E causes a rotation of E by 2φ.
A Glan-Thompson prism is a birefringent cuboid with the optical axis parallel to its smaller entrance and exit surfaces. The cuboid has a diagonal cut, which is chosen so that the ordinary beam is totally reflected while the extraordinary beam is transmitted with almost no reflection or refraction. If the optical axis is directed along the y axis,

linear polarized light with $E = E_y$ is transmitted and light with $E = E_x$ is reflected. In order to measure the circular polarization degree of a light beam, it is send through a system consisting of a quarter-wave plate and a Glan-Thompson prism. If the quarter-wave plate is set to +45° and the optical axis of the Glan-Thompson prism is aligned along the y axis, only σ^+-polarized light is completely transmitted, while σ^--polarized light is completely blocked. The −45° setting of the quarter-wave plate leads to the opposite result. Linearly polarized light of any polarization angle delivers a constant transmission for both settings. The light intensity I, measured for the +45° setting is denoted as I_+ and as I_- for the −45° setting. The circular polarization degree is given by

$$\rho_\mathrm{c} = \frac{I_+ - I_-}{I_+ + I_-}. \tag{3.1}$$

The determination of the linear polarization degree can be carried out with a half-wave plate and a Glan-Thompson prism or with two quarter-wave plates and a Glan-Thompson prism. Here, only the first method is discussed. If the half-wave plate is set to 0° and the Glan-Thompson prism is aligned along the y axis, the system will only transmit the 'vertically polarized' component with $E = E_y$, while the 'horizontally polarized' component E_x is blocked. The ±45° settings of the half-wave plate lead to the opposite result. Circular polarized light delivers a constant transmission for both settings. The light intensity, measured for the 0° setting is denoted as I_0 and as I_{90} for the ±45° settings. For the complete description of the linear polarization, it is necessary to measure the PL intensity also in the -22.5° (I_{135}) and the +22.5° (I_{+45}) settings of the half-wave plate. Otherwise, the examination of diagonal polarized light would result in a polarization degree of 0. Thus, the full linear polarization degree is given by

$$\rho_\mathrm{l} = \frac{\sqrt{(I_0 - I_{90})^2 + (I_{45} - I_{135})^2}}{I_0 + I_{90}}. \tag{3.2}$$

The set of $(I_0 + I_{90})$, $(I_0 - I_{90})$, $(I_{45} - I_{135})$ and $(I_+ - I_-)$ is known as 'Stokes parameter'.

3.2.2 Optical orientation and magnetic field induced polarization

In PL experiments, the knowledge of ρ_c and ρ_l alone does not necessarily provide information about the physical origin of the polarization. For simplification, let's consider a laser as light source and an excitonic two-level energy system in which the two energy levels have the opposite polarization, i.e. either σ^+ and σ^- or vertical and horizontal polarization. The polarization of the PL can now stem from two different sources:
1) The polarization of the laser light is fully or partly preserved by the two-level system and the emitted PL has the same polarization as the laser light. For example the laser emits σ^+ polarized light and excites the σ^+ state of the exciton. If the exciton spin remains unchanged until the recombination occurs ($\tau_\mathrm{s} > \tau_\mathrm{r}$), the polarization is preserved. This effect is called 'optical orientation'. In case of linear polarized light, the effect is called 'optical alignment' [67].
2) Unpolarized laser light excites both states of the two-level system equally. If the energy levels are split by ΔE and it is $\tau_\mathrm{r} > \tau_\mathrm{s}$ and $\Delta E > k_\mathrm{B}T$, where T is the temperature of the system, the lower state is preferred and the emitted PL shows the polarization of

the lower level. In case of circular polarized states, the splitting can be caused by the Zeeman effect in an external, longitudinal magnetic field. This effect is called 'magnetic field induced' polarization [68], [69]. In case of linear polarization, the splitting might be caused by the anisotropic exchange splitting in asymmetric QDs.
Both sources of polarization can occur simultaneously. To determine the degrees of optical orientation and magnetic field induced polarization of the circularly polarized PL, it is necessary to measure the circular polarization degrees, ρ_c^+ and ρ_c^-, for σ^+ and σ^- polarized excitation:

$$\rho_c^+ = \frac{I_+^+ - I_-^+}{I_+^+ + I_-^+}, \quad \rho_c^- = \frac{I_+^- - I_-^-}{I_+^- + I_-^-}, \tag{3.3}$$

where I_b^a is the intensity of the σ^b polarized PL under excitation with σ^a polarized laser light. Then the optical orientation degree ρ_{oo} and the magnetic field induced polarization degree $\rho_{c,B}$ are given by [70]

$$\rho_{oo} = \frac{\rho_c^+ - \rho_c^-}{2}, \quad \rho_{c,B} = \frac{\rho_c^+ + \rho_c^-}{2}. \tag{3.4}$$

The circular polarization degree ρ_c, as it is defined in Eq. (3.1), is the sum of ρ_{oo} and $\rho_{c,B}$. Therefore, there are two conditions that simplify the measurement: 1) If the sample is excited with unpolarized light, it is $\rho_{oo} = 0$ and $\rho_{c,B} = \rho_c$. Usually, this is also the case with nonresonant excitation, since it can be expected that the polarization of the laser light is lost during the energy relaxation. 2) If the external magnetic field is zero, the magnetic field induced polarization is zero too. Thus, it is $\rho_{c,B} = 0$ and $\rho_{oo} = \rho_c^+ = -\rho_c^-$. For linearly polarized PL, the optical alignment is defined analogously to Eq. (3.3).

3.3 Macro Setups: Steady-state and time-resolved photoluminescence

The basic setup, which was used for all macroscopic PL measurements, is shown in Fig. 3.1. Laser, detection system and synchronization system vary for different kinds of measurements. The details are given in this section.

Steady-state experiments on (In,Al)As/AlAs QDs, which are presented in chapter 6, were performed in the labs of the Ioffe Institute in Saint Petersburg and at the Technical University of Dortmund. Although several components of the setups differ from one another, the measuring principles are the same. Since most of these measurements were carried out at the Ioffe Institute, the method used here is given first and the method used in Dortmund, if different, is given in brackets.
The sample was placed in a cold-finger closed-cycle cryostat (liquid helium bath cryostat), in which the temperature can be reduced to 10 K ($\sim$ 1.6 K). A tunable cw Ti:sapphire laser was used for the selective excitation. The laser beam was almost parallel to the z axis of the sample. A small angle in between reduced the intensity of the reflected laser light. The PL was dispersed by a double monochromator (0.5 m monochromator) and detected by an avalanche photodiode (a liquid nitrogen-cooled charge-coupled-device (CCD) camera). For polarization measurements, the laser light was circularly / linearly

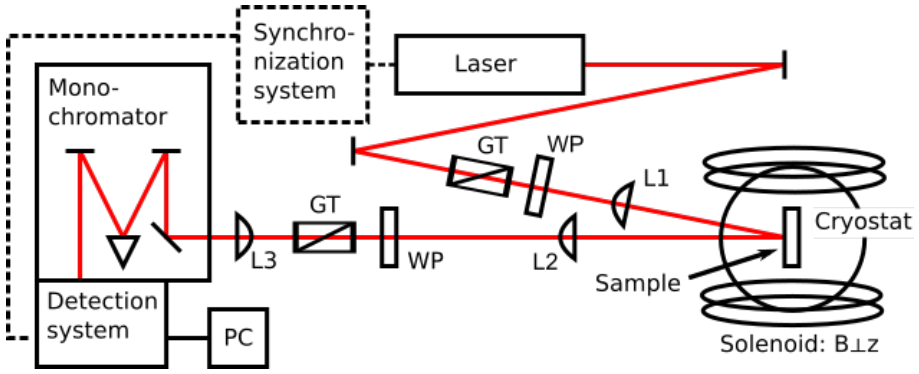

Figure 3.1: Basic setup for macroscopic PL measurements. The laser beam (red) is focused by lens L1 onto the sample, which is placed in a cryostat. A magnetic field can be applied by the surrounding solenoids (here: Voigt geometry). The PL is collected by lens L2 and focused onto the entrance slit of the monochromator. The intensity of the dispersed PL is measured by the detection system. The polarization of the laser beam and the PL can be selected by a wave plate (WP) and a Glan-Thompson Prism (GT) each. In case of time-resolved measurements, the detection system is synchronized with the pulsed laser, which is indicated by the dashed part of the setup.

polarized by a Glan-Thompson prism and a quarter- / half-wave plate. The polarized PL was selected by a photoelastic modulator and a quarter-wave plate (Glan-Thompson prism and a quarter- / half-wave plate). Magnetic fields up to 100 mT (10 T) were applied by an electromagnet (a superconducting split-coil solenoid). The direction of the field could be changed continuously between the parallel and the perpendicular alignment to the growth axis z of the sample.
The GaAs/AlAs QW structure was studied in Dortmund under nonresonant excitation only. For this purpose the third harmonic of a pulsed, Q-switched Nd:YVO_4 laser with a photon energy of 3.49 eV, a repetition rate of 2 kHz and a pulse duration of 5 ns was used. For the steady-state experiments, the setup was structured as described above for the QD sample, see also Fig. 3.1. The results are presented in chapter 5.

Time-resolved measurements were performed at the Technical University of Dortmund. For this purpose, the setup is supplemented by a synchronization system to trigger the detection system, see dashed part of Fig. 3.1. For the nonresonant excitation of the (In,Al)As/AlAs QD ensemble, a pulsed, Q-switched Nd:YVO_4 laser with a photon energy of 3.49 eV and a pulse duration of 5 ns was used. The laser beam was almost parallel to the z axis of the sample. The sample was placed in a liquid helium bath cryostat with superconducting split-coil solenoids. Thus, it was possible to decreased the temperature down to 1.6 K and to increase the magnetic field up to 10 T. To change the direction of the magnetic field from Faraday ($B \parallel z$) to Voigt geometry ($B \perp z$), the cryostat was rotated by 90° with respect to the sample.
The PL of the (In,Al)As/AlAs QD ensemble was dispersed by a 0.5 m monochromator and detected by a gated CCD camera. A function generator created a trigger signal with a frequency of 2 kHz to synchronize the laser and the gated CCD camera. In order to measure the PL intensity as a function of the time after the laser pulse, the temporal

delay t_{delay} between the trigger signal and the begin of recording was varied between 0 ns and 500 μs. The exposure time t_{gate} was optimized with regard to signal intensity and time resolution for the different values of t_{delay}. The highest possible resolution of the camera is 1 ns. For a PL spectrum measured after a delay of t_{delay} and an exposure time of t_{gate}, the characteristic time is $t = t_{\mathrm{delay}} + \frac{1}{2}t_{\mathrm{gate}}$ with $\Delta t = \pm\frac{1}{2}t_{\mathrm{gate}}$. The results of the time-resolved experiments on the (In,Al)As/AlAs QD ensemble are presented in Sec. 6.2.
For the GaAs/AlAs QW, the time-resolved PL intensity was measured with a photomultiplier tube (PMT), which was connected to a multichannel analyzer (MCA) with a time resolution of 30 ns. The MCA was synchronized with the Nd:YVO_4 laser via a function generator. The function generator delivered a start signal for the MCA, which counted the number of events in 64 subsequent time windows. The duration of these time windows t_{gate} was varied between 30 and 10000 ns. The accumulation time for one decay curve was usually between 5 and 15 minutes. The results are presented in Sec. 5.4.

The time-resolved measurements under selective excitation of the (In,Al)As/AlAs QD ensemble, presented in Sec. 6.6.2, were performed with a picosecond optical parametric amplifier (OPA), pumped by a Pharos laser. The output wavelength of the OPA could be tuned between 315 and 2700 nm and the pulse duration was 3.3 ps. The repetition rate was 30 kHz and could be reduced down to 1 Hz by a pulse picker. Since the laser system was not in the same room as the rest of the experimental setup, the laser beam was guided by a fiber to the setup. This multimode fiber (300-1200 nm) had a length of about 50 m and a diameter of 400 μm. In order to synchronize laser and CCD camera, the laser beam was passed through a glass plate, whereby a small fraction was deflected onto a photodiode. The voltage rise, caused by the photocurrent in the diode, was used as trigger signal ($t = 0$) for the gated CCD camera.

3.4 Microphotoluminescence of single quantum dots

The technique of microphotoluminescence (μPL) measurements is applied when the PL to be examined is emitted from a range of several μm diameter. This includes e.g. the study of micropillars or larger nanostructures like nanoplatelets. It can also be used to detect the PL from single QDs in an ensemble of QDs, as it is demonstrated in Sec. 6.4.2. For this purpose, the sample must be prepared in such a way that the local density of QDs is reduced. In the studied case, this is archived by the creation of mesa structures via Ar^+ ion dry etching and electron-beam lithography.
Figure 3.2 shows an image of a mesa, which was made by a scanning electron microscope. The mesas sit on top of the GaAs buffer layer of the QD sample and have a cylindrical shape with a diameter of $200 - 500$ nm. In order to protect the structure from oxidation, it was covered with dielectric Si_3N_4 directly after the etching. The amount of QDs on a mesa structure can be estimated by the QD density and the size of the mesa. For sample RC 1517 with a density of $1.2 \cdot 10^{10}$ cm^{-2} this results in approximately 4 to 24 dots per mesa.
The sample was placed in a microcryostat and cooled down to 8 K by helium-gas flow. The laser beam was focused to a spot of 10 μm diameter by a 50 Mitutoyo microscope objective with an numerical aperture of 0.42. In order to position the laser spot exactly on

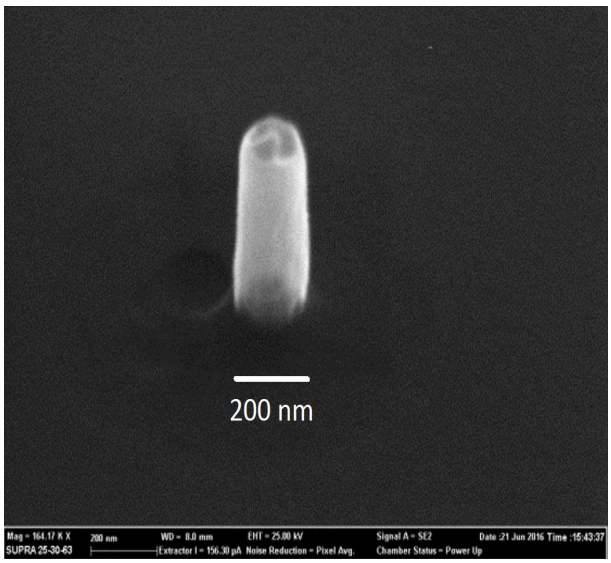

Figure 3.2: Single mesa structure of the (In,Al)/AlAs QD sample recorded with a scanning electron microscope.

the mesa, the sample was shifted by an Attocube XYZ piezodriver. For the measurement of time-integrated PL spectra a continuous-wave laser with a photon energy of 3.07 eV was used. Linear polarized PL was selected by an achromatic half-wave plate and a Glan-Taylor prism. For the time-resolved measurements a pulsed semiconductor laser with a photon energy of 3.07 eV and a repetition rate of $30-50$ MHz was used. To study the PL dynamics of single QDs, spectral lines were chosen with a tunable bandpass filter. The emission was detected by a Si single-photon avalanche diode with a temporal resolution of 40 ps.

4 Sample properties

This chapter summarizes the previously known structural and physical properties of the studied samples, the ultrathin GaAs/AlAs QW and the (In,Al)As/AlAs QD ensemble, both with indirect band gaps in momentum space. Although the studied QW and the QD ensemble have structural similarities like the GaAs substrate and the AlAs matrix, which is causing the confinement along the z direction, they differ in material composition and spatial degrees of freedom. In Ref. [26], it is demonstrated that the (In,Al)As/AlAs QDs have type-I band alignment, while the GaAs/AlAs QW is of type-II [14]. The logical link between the two structures might be the InAs/AlAs QW with type-I alignment [14], which is studied in Sec. 5.1 together with the GaAs/AlAs QW. In the cited references it is also shown that the X_{xy} valley is the lowest point of the conduction band in all three structures. To give an overview about the sample properties, the growth details and the current states of research for the GaAs/AlAs QW and (In,Al)As/AlAs QD structures are presented in the following sections.

4.1 GaAs/AlAs quantum well with type-II alignment

4.1.1 Previous research on similar structures

Around 1990 the band structures of GaAs/AlAs QWs and superlattices were studied with regard to their dependence on the size of the GaAs and the AlAs layers. A type-II structure is achieved, if the GaAs layer is smaller than 35 Å [71] [72], provided that the AlAs layer is thicker than 15 Å [73]. Then, the holes are located in the GaAs layer at the Γ point of the valence band, while in AlAs, an indirect semiconductor, the lowest state of the conduction band is the X_{xy} state. If the size of the AlAs layer is reduced below 60 Å, the energy levels of X_{xy} and X_z cross and X_z becomes the ground state [74]. To distingish between these two cases, the shapes of the PL spectra were studied: The recombination of the X_{xy} electron is mainly phonon-assisted and accompanied by several phonon replicas in the spectrum, while the recombination of the X_z electron is caused by the mixing with the Γ-electron state in GaAs and thus characterized by a strong zero-phonon line [75]. A further decrease of the AlAs layer size enhances the ΓX_z mixing, resulting in the decrease of the recombination time [32]. However, for both types of excitons the recombination time is much longer than for direct band-gap excitons. In case of the X_{xy} exciton it can reach several hundreds of microseconds [76].
Moreover, in a GaAs/AlAs QW with type-II alignment, a strong increase of the spin-relaxation time was observed with respect to type-I structures, which was attributed to the reduction of the exchange interaction [77]. As the strength of the exchange interaction depends on the distance between electron and hole, the fine structure splitting δ_0 depends on the structure sizes. This relation was determined for GaAs and AlAs layers between 10 and 45 Å by means of optically detected magnetic resonance, revealing bright-dark splittings between 0.6 to 20 μeV [78]. Further studies on the fine structure of GaAs/AlAs

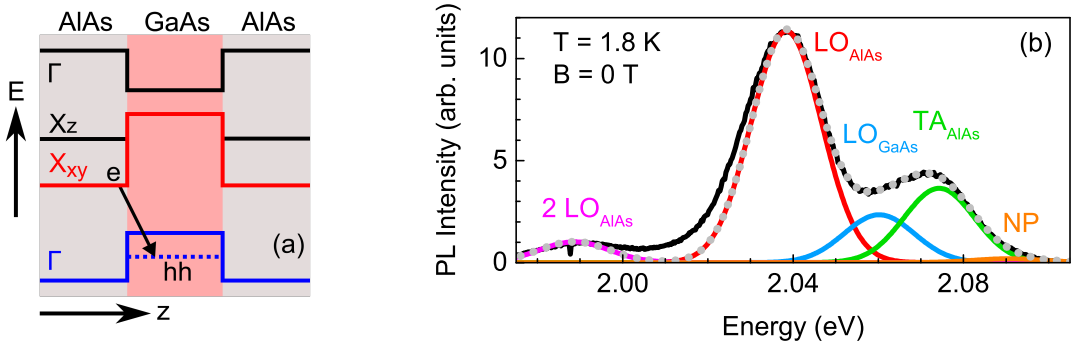

Figure 4.1: **(a)** Schematic representation of the studied type-II GaAs/AlAs QW with the band structure. The diagonal arrow marks the indirect recombination of the electron in the X_{xy} valley (red) of the conduction band in the AlAs layer and the heavy hole at the Γ valley (blue) of the valence band in the GaAs layer. **(b)** PL spectrum of the ultrathin GaAs/AlAs QW (black line) consisting of the no-phonon line (NP) and the phonon replicas of $\mathrm{LO_{AlAs}}$, $\mathrm{TA_{AlAs}}$ and $\mathrm{LO_{GaAs}}$ phonons. The PL lines are identified by the energetic positions of the Gaussian functions that are fitted to the spectrum. The sum of the Gaussian curves is given by the grey, dotted line.

superlattices with the X_z exciton as ground state followed. Theses studies demonstrate the heavy-hole light-hole mixing in quantum-beats experiments [79], [80] or focus on the anisotropic exchange splitting [81]. However, the redistribution of excitons between bright and dark states has not been thoroughly investigated up to now.

4.1.2 Growth details and first results of the studied sample

The studied GaAs/AlAs quantum well structure was grown by molecular-beam epitaxy on top of a (001)-oriented, semi-insulating GaAs substrate and a 200 nm thick GaAs buffer layer. The QW consists of two monolayers of GaAs, embedded between two 50-nm-thick AlAs layers. The upper AlAs layer is covered by a 20 nm thick cap layer of GaAs to protect it from oxidation. Further details can be found in Ref. [14], where it is also demonstrated that the structure has a type-II band alignment and the lowest point of the AlAs conduction band is found in the X_{xy} valley. This is illustrated in Fig. 4.1 (a). The exciton recombination dynamics of the studied ultrathin GaAs/AlAs QW was investigated in 2016 in strong magnetic fields [31]. These studies also provide an overview of the composition of the PL spectrum and give insight into the fine structure of the QW. The results of this work are summarized below.
The PL spectrum of the ultrathin GaAs/AlAs QW under nonresonant excitation with $E_{\mathrm{exc}} = 3.49$ eV is shown in Fig. 4.1 (b) by the black line. It turns out that the spectrum contains strong contributions from several phonon replicas in addition to the weak no-phonon line (NP) at $E = 2.091$ eV, which is typical for X_{xy} excitons [75]. For the identification of the replicas, five Gaussian functions with the same full width at half maximum (FWHM = 16 meV) are fitted to the spectrum. In AlAs, the phonon energies at the X point are 12 meV for transversal acoustic phonons ($\mathrm{TA_{AlAs}}$) and 48 meV for longitudinal optical phonons ($\mathrm{LO_{AlAs}}$). In GaAs, the $\mathrm{LO_{GaAs}}$ phonons have an energy of 30 meV [82]. Thus, the highest PL peak at $E = 2.039$ eV (red) is identified as the

LO_{AlAs} phonon replica and the second highest PL line at $E = 2.074$ eV (green) can be assigned to the TA_{AlAs} phonons. Between these two peaks another PL signal is found at $E = 2.060$ eV (blue), which can be identified as the LO_{GaAs} phonon replica. At $E = 1.989$ eV a two-phonon process with LO_{AlAs} phonons (magenta) is observed. The sum of the Gaussian fits is shown by the dotted grey line. Its mismatch with the PL signal at lower energies, indicates that further multi-phonon processes might play a role. The broadening of the lines is explained by the roughness of the interface between QW and barrier and also by deviations in the material composition of the QW [14], [83].
For low temperatures ($T < 7$ K), the application of a high magnetic field in Faraday geometry ($B \parallel z$) leads to a strong decrease of the integrated PL intensity and to the increase of the exciton recombination time. However, the influence of the magnetic field can be eliminated by increasing the sample temperature. These effects were explained in the framework of the model presented in 2.4, which describes the spin dynamics between the dark and bright fine-structure levels of the X exciton. The comparison of theory and experimental data allowed the estimation of the longitudinal heavy-hole g factor $g_{hh} \geq 2.5$ as well as the determination of the radiative recombination time $\tau_{rad} = 0.34$ ms of bright excitons and the nonradiative recombination time $\tau_{nr} = 8.5$ ms of bright and dark excitons [31].

4.2 (In,Al)As/AlAs quantum dot ensemble

4.2.1 Growth details

Two (In,Al)As/AlAs QD ensembles with quite similar properties, sample AG 2890 and sample RC 1517, are studied in this thesis. The main difference between them is the amount of QD layers. Since sample RC 1517 contains only one layer, it is suitable for the μPL measurements in Sec. 6.4.2 in which PL lines from single QDs are detected. For all other measurements sample AG 2890 with 20 QD layers and a considerably higher PL intensity is used. A detailed description of the growth procedure of the two studied QD samples is given in Ref. [26]. The information relevant to this work is summarized below.

The studied samples are made from the III-V compound semiconductor materials indium arsenide (InAs) and aluminium arsenide (AlAs) by molecular-beam epitaxy. InAs and the barrier material AlAs intermix during the growth procedure. The InAs fraction x in the $In_xAl_{(1-x)}As$ QDs is determined by the temperature and interruption time during the molecular beam epitaxy. Between 440 and 510 °C the increasing growth temperature T_g leads to the decrease of the InAs fraction in the dots due to the enhanced intermixing with AlAs. For $T_g > 510$ °C, x decreases further, now mainly due to the evaporation of In atoms. Therefore, in the low temperature regime, higher intermixing is connected with a higher effective volume of the QDs, while further increase of the In concentration leads to the decrease of the size. Since the PL energy is mainly determined by the size of the dots, it is possible to set the central energy of the emission spectrum via the growth temperature. Moreover, the interruption of the growth process causes an increase of the average dot diameter and the size dispersion with time.
The nominal In concentration is $x = 0.64$ for sample RC 1517 and $x = 0.70$ for sample AG 2890. However, within a single lenticular QD the spatial distribution of InAs is not uniform. The exact distribution is unknown but it is assumed that the maximum

concentration is located at the center, close to the bottom of the dot. Looking at a cut surface through the dot along the growth axis z, the decrease of the concentration can be described by a two-dimensional Gaussian function.
Note that the QDs of both samples are nominally undoped.
The dots are grown on an AlAs layer, sitting on top of the GaAs substrate. The latter has a (001)-orientation, which determines the growth direction z of the whole system. The materials crystallize in the zincblende structure. In sample RC 1517, the density of the dots is $1.2 \cdot 10^{10}$ cm^{-2} and the average size is (16.3 ± 8.6) nm. For sample AG 2890, the density is $3 \cdot 10^{10}$ cm^{-2} and the average size is about 15 nm. The QD layer is covered with another AlAs layer. The two surrounding AlAs layers form the QD barriers, leading to a type-I QD system. While sample RC 1517 contains only one QD layer between its 70-nm-thick barriers, AG 2890 is made from 20 QD layers separated each by 20-nm-thick AlAs barriers to prevent the electronic coupling between adjacent layers. To prevent the oxidation of the top AlAs layer, both samples are covered with a GaAs cap layer. Additionally, a SiO_2 antireflection coating enhances the PL emission of RC 1517.

4.2.2 Previous state of research

The investigation of the (In,Al)As/AlAs QD ensembles, which are studied in this thesis, got off ground in 2008. Already in 2002 the group of P. Dawson measured mircosecond PL dynamics for InAs/AlAs QDs and initially attributed it to the recombination of electrons and holes in different QDs [84] and later to the recombination of electron-hole pairs in type-II QDs [85]. However, in 2008 it was shown by T. S. Shamirzaev et al. that the band alignment of the dots is actually of type I [86].
As described in the growth details, the QDs of the ensemble differ in size by several nanometers. Under nonresonant excitation with energies above the AlAs barrier, all QDs are excited and the size dispersion is reflected in a broad emission spectrum, shown by the red line in Fig. 4.2 (a). The carrier transfer from the AlAs barrier to the (In,Al)As QDs and the role of the wetting layer were studied in 2010. It was found that the capture time of several picoseconds is independent from the dot size or composition. Therefore, the probability of occupation is the same for all QDs [27]. The QD size and composition, which determine the energetic structure, were studied in dependence of the growth conditions and it was shown, that the ground state of the conduction band can change from the Γ to the X valley [39], [26].
The transition from the Γ to the X valley can be explained with the help of Fig. 4.2 (b), which shows the energies of the different band minima (valleys) in dependence of the QD size. For the largest QDs, the Γ valley of the conduction band (red line, Γ_{CB}) is lower in energy than the X valley (blue line) and forms the ground state of the excited electron. This is shown on the left side of (b). For these dots the transition between electron and hole is direct in momentum space (orange arrows), since the hole is located in the Γ valley of the valence band (red line, Γ_{VB}) for all QD sizes. The decrease of the QD size leads to the energetic increase of all bands due to the stronger confinement. According to Eq. (2.2), the slope of the bands depends on the effective mass m^* of the respective carrier. As the effective mass of the Γ electron is low compared to the effective mass of the X electron (see Tab. 6.1), the energy of Γ_{CB} increases stronger and crosses the X valley for a specific dot size [87]. The corresponding excitation energy is the ΓX-transition energy $E_{\Gamma X}$. Here, the mixing of Γ and X states takes place and the electron can scatter from

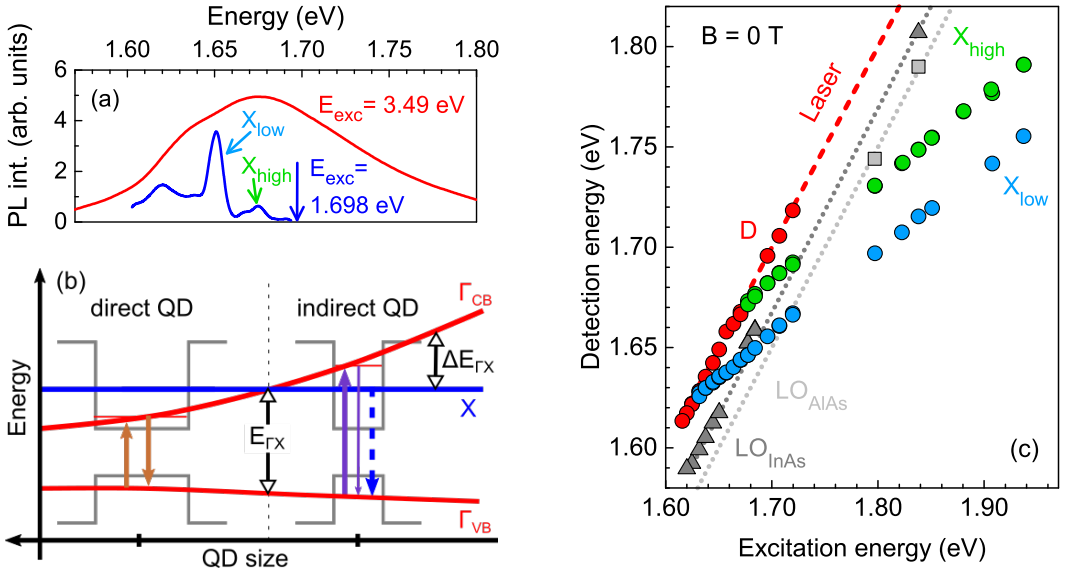

Figure 4.2: **(a)** PL spectrum of the (In,Al)As/AlAs QD ensemble under nonresonant excitation (red line) and PL spectrum emitted by indirect QDs under selective excitation (blue line). Indirect exciton lines are marked as X_{low} (blue) and X_{high} (green). $B = 0$ T, $T = 1.8$ K. **(b)** Band structure schematics in dependence of the QD size and transitions (colored arrows) for two QDs of different sizes with either the Γ (red line) or the X valley (blue line) as the lowest conduction band state. Solid arrows correspond to direct and dashed arrows to indirect transitions in momentum space. The dashed vertical line marks the QD size at which the energies of the Γ and X electron levels are equal. $E_{\Gamma\mathrm{X}}$ is the corresponding excitation energy. $\Delta E_{\Gamma X}$ is the splitting between the Γ and X electron levels in the conduction band of indirect QDs. **(c)** PL peak energies of the QD spectra (sample AG 2890) in dependence of the excitation energy. The laser line is indicated by the red, dashed line. Observed PL features are the D line (red dots), the phonon replicas $\mathrm{LO_{InAs}}$ (triangles) and $\mathrm{LO_{AlAs}}$ (squares) and the indirect exciton lines X_{low} (blue dots) and X_{high} (green dots). Dotted lines are guides for the eye. $T = 1.8$ K. Adapted from Ref. [70].

the Γ to the X valley. For even smaller dots, the X-electron level is lower in energy than the Γ level and the scattering process is accompanied by an energy relaxation. The splitting $\Delta E_{\Gamma X}$ between the Γ and the X valley is denoted as the 'ΓX splitting' in the following.

In the spectral region of the indirect QDs the recombination time is prolonged to the μs range [39], [29]. The long recombination time of the X excitons is one of the most important properties of the (In,Al)As/AlAs QDs, since it extends the spin lifetime. The prolongation can be explained by the indirect band gap in k space, which demands a change of the electron momentum for the recombination, see Sec. 2.2. As the loss of momentum occurs mainly due to the scattering at the heterointerface between the QD and the AlAs barrier, the recombination time is highly sensitive to the sharpness of the QD surface [28].

The selective excitation of a fraction of the (In,Al)As/AlAs QDs with the same size was first demonstrated in Refs. [29] and [88]. An example of the associated PL spectrum for $E_{\mathrm{exc}} = 1.698$ eV is shown in Fig. 4.2 (a) by the blue line. In contrast to the broad PL spectrum under nonresonant excitation (red line), selective excitation causes several narrow PL lines, the so-called fluorescence line narrowing spectrum [89], [90]. This technique allows to determine the ΓX-transition energy $E_{\Gamma X}$ and to monitor the energetic shift $\Delta E_{\Gamma X}$ of the X-exciton line with respect to the Γ-exciton line in the PL spectrum, like it is shown in Fig. 4.2 (c). For this purpose, the laser energy is tuned in the full spectral region of the QD emission. In this way, only the fraction of dots with the appropriate size is excited resonantly. In case of large, direct QDs the PL signal of the Γ exciton overlaps with the laser line (red dashed line). However, a sideband of the direct signal (red dots), shifted by about 3 meV to lower energies, can be observed. In Ref. [29] this line is denoted as an acoustic phonon replica. In section 6.1.1 further evidence is given for that assumption. Since the line is related to the direct recombination, it is denoted as 'D line' (D in figures) in the following.
Further phonon replicas can be observed in a spectral distance of about 30 and 50 meV from the laser line, shown by the grey triangles and squares in Fig. 4.2 (c). In Ref. [70], these lines were identified as the replicas of the LO phonons in InAs and AlAs [82].
The PL line of indirect excitons in smaller QDs moves away from the laser position with increasing excitation energy due to the growing energy splitting $\Delta E_{\Gamma \mathrm{X}}$ between the Γ and the X valley. The PL peak positions of the direct (red dots) and indirect signals (blue and green dots) are plotted in Fig. 4.2 (c) in dependence of the excitation energy. The transition energy $E_{\Gamma \mathrm{X}}$ can be determined as the crossing point of these lines. For sample AG 2890, two indirect PL lines, X_{low} and X_{high}, appear in the spectra. The two transition energies were determined to $E_{\Gamma X}^{\mathrm{low}} = 1.63$ eV and $E_{\Gamma X}^{\mathrm{high}} = 1.67$ eV [70]. The reason for the existence of two indirect PL lines is unclear so far.

In 2012 the g factors of the X electron, the Γ heavy hole and the related indirect exciton were measured by the spin-flip Raman technique [29], [88] for $E = 1.636$ eV, see Tab. 6.2. Later, the g factor of the X-valley electron was confirmed for different energies by means of optically detected magnetic resonance [91].
The first documentation of the optical orientation of the X excitons in (In,Al)As/AlAs QDs was given in the outlook of Ref. [88]. Further studies in small magnetic fields (below 100 mT) showed that the optical orientation degree of the X excitons increases strongly in Faraday geometry ($B \parallel z$) and decreases down to zero in Voigt geometry ($B \perp z$). Surprisingly, it was found that the half width at half maximum (HWHM) of the Hanle curve does not reflect the spin lifetime of several μs, which was expected for that structure [70].
The spin relaxation time τ_{s} was determined under nonresonant excitation in dependence of the longitudinal magnetic field B and the temperature T. For $B > 4$ T these experiments revealed a spin relaxation time in the μs range with a B^{-5} and a $T^{-0.85}$ dependency [88]. Both relations are typical for spin relaxation via phonon scattering [92], [93].

5 Results I: Ultrathin quantum well with indirect band gap

The study of spin dynamics in the GaAs/AlAs QW is particularly interesting due to the extremely long exciton lifetime of 0.34 ms [31] in this structure, which is caused by the type-II alignment and the indirect band gap in momentum space. Moreover, the lack of electron-hole exchange interaction leads to the degeneration of the exciton states, which can be lifted by the Zeeman effect. This new situation makes it possible to investigate the spin dynamics between bright and dark states, which is reflected, for example, in nonmonotonic dependencies of the circular polarization degree from thermodynamic quantities.
The two following sections deal with the spin dynamics of electrons and holes between dark and bright states and the resulting polarization properties of the GaAs/AlAs QW sample, which is introduced in Sec. 4.1. Section 5.1 covers the field of the circular polarization degree. The results are compared with the ones for an InAs/AlAs QW with type-I alignment. In section 5.2 the linear polarization of the GaAs/AlAs QW is investigated. In both sections, the experimental results are compared with the kinetic spin model (see Sec. 2.4) in order to determine important structure parameters.
The samples are studied under nonresonant, pulsed excitation with a photon energy of 3.49 eV. All QW studies in this work are related to phonon-replica lines of the QW spectrum. As the origin of the NP line is not fully understand yet, it is excluded from the analysis and the discussion.

5.1 Circular polarization dynamics

5.1.1 Experimental results and kinetic spin model

The circularly polarized exciton PL was measured for the GaAs/AlAs and the InAs/AlAs QW at different field strengths, field directions and temperatures in steady-state experiments. The sign of the polarization is determined via a control sample with known sign [94]. For the GaAs/AlAs QW, Fig. 5.1 (a) shows the PL spectra of the polarized intensity components I_+ (red line) and I_- (blue line) in a longitudinal magnetic field with $B = 4$ T. The related polarization spectrum is presented in Fig. 5.1 (b) by the red line. At the spectral position of the $\mathrm{LO_{AlAs}}$ phonon replica, the circular polarization degree reaches its maximum of 61%. At the $\mathrm{TA_{AlAs}}$ line the value is about 50%. Surprisingly, the increase of the magnetic field strength from 4 to 10 T (purple line) leads to the decrease of the circular polarization degree. In absence of a magnetic field (blue line), the circular polarization is zero for the whole spectral range. Since the overall shape of the polarization spectrum is preserved for changes in the magnetic field strength, the analysis only refers to the $\mathrm{LO_{AlAs}}$ line.
Figures 5.1 (c) and (d) show the circular polarization degree (colored symbols) in depen-

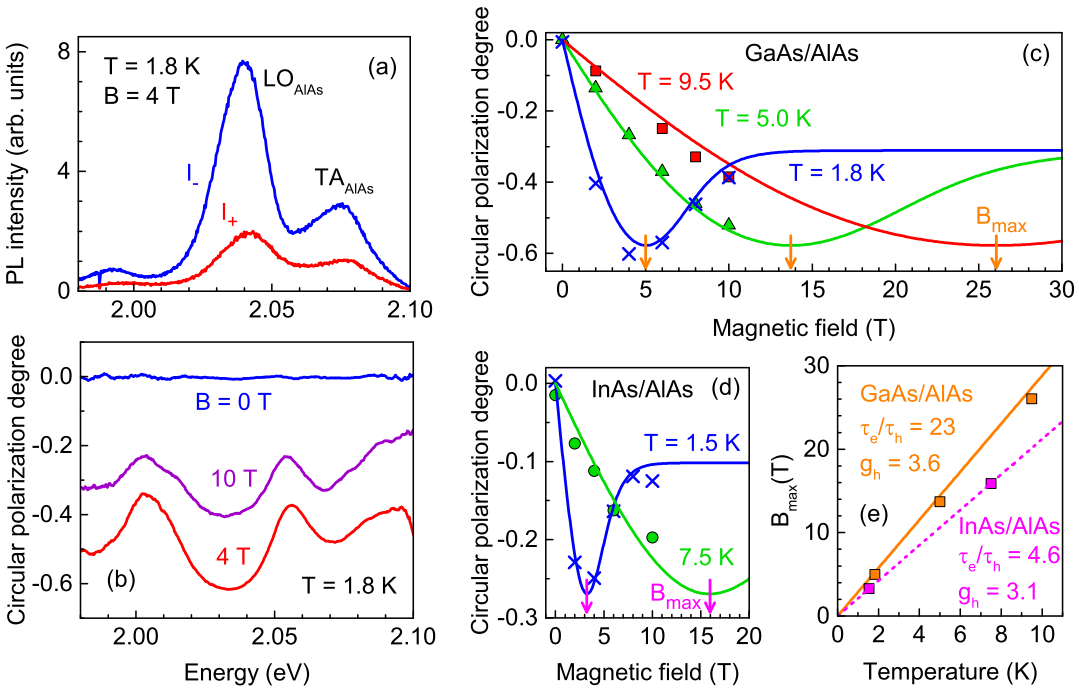

Figure 5.1: **(a)** Spectra of the circular polarized PL components I_+ (red) and I_- (blue), emitted by the GaAs/AlAs QW for $B = 4$ T. **(b)** Circular polarization spectra at different magnetic field strengths ($B \parallel z$) for $T = 1.8$ K. **(c)** and **(d)** Magnetic field induced circular polarization degree of the $\mathrm{LO_{AlAs}}$ phonon replica measured for GaAs/AlAs (a) and InAs/AlAs (b) in Faraday geometry ($B \parallel z$) for different temperatures. The lines show the results of fitting the model function (5.1) to the data sets. The arrows mark the magnetic field values B_{max} at which the fit functions reach their maximum values. **(e)** B_{max} in dependence of the temperature. The values (squares) are taken from (c) and (d). For GaAs/AlAs, the orange line represents Eq. (5.2) with the parameters $\tau_\mathrm{e}/\tau_\mathrm{h}$ and g_h which are obtained from the fit in (c). For InAs/AlAs, the magenta line is a linear fit of the type $B_{\mathrm{max}} = aT$ with the parameter $a = 2.121$ T/K. g_h is obtained from the fit in (d) and $\tau_\mathrm{e}/\tau_\mathrm{h}$ by the comparison of the linear fit with Eq. (5.2).

dence of the longitudinal magnetic field for different sample temperatures. For $B = 0$, the polarization is always zero. The application of a magnetic Faraday field initially leads to the increase of ρ_c. The slope of this increase is determined by the sample temperature. At the lowest temperatures, $T = 1.8$ K for GaAs/AlAs and 1.5 K for InAs/AlAs, the experimental data show a nonmonotonic behavior of the circular polarization degree. For GaAs/AlAs, the highest degree of 60% was measured at 4.8 T. Stronger fields lead to the decrease of ρ_c down to 39% at 10 T. For InAs/AlAs, the maximal circular polarization degree of about 25% is expected between 2 and 4 T. At higher fields, ρ_c decreases and for $B > 8$ T it seems to saturate at around 12%. At higher temperatures, the nonmonotonic behavior can no longer be observed in the studied magnetic field range. The colored lines in Figs. 5.1 (c) and (d) show the results of fitting Eq. (5.1) to the data sets. The fitting and the associated Fig. 5.1 (e) will be discussed later in this section.

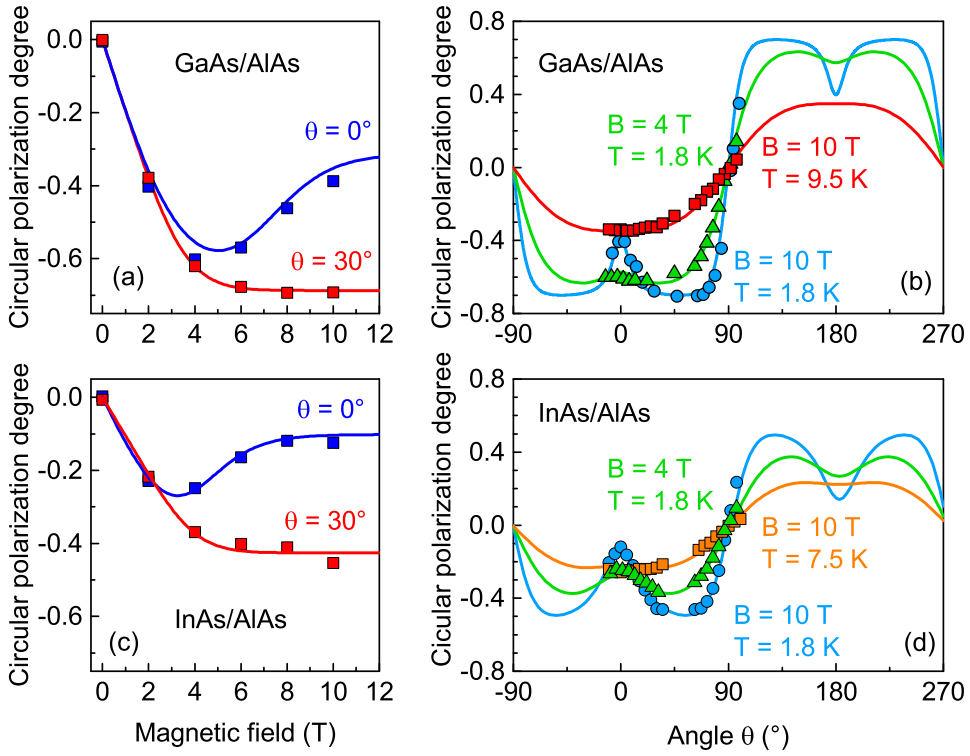

Figure 5.2: **(a)** GaAs/AlAs QW: Magnetic field dependency of the circular polarization degree measured for two different angles θ of the magnetic field direction. **(b)** GaAs/AlAs QW: Angle dependencies of the circular polarization degree measured for different field strengths and temperatures. The colored lines show the results of fitting the model function (5.1) to the data sets. **(c)** and **(d)** Repetition of the measurements presented in (a) and (b) for the InAs/AlAs QW sample.

The impact of a tilted magnetic field on the circular polarization degree is shown in Fig. 5.2 for both samples. In (a), the magnetic field dependence of ρ_c, measured for the GaAs/AlAs QW in Faraday geometry ($\theta = 0°$), is compared with the dependence at an angle of 30° between B and z. Up to 4 T the increase of the circular polarization degree is about the same for both angles. However, for higher, tilted fields (red squares) ρ_c saturates at 69%, whereas in Faraday geometry (blue squares) ρ_c drops back to 39%, like it is described above. In (c), it can be seen that the maximal polarization degree of the InAs/AlAs QW excitons is only about 40% for $\theta = 30°$.
The angle dependence of the circular polarization degree, measured for the GaAs/AlAs QW, is shown in Fig. 5.2 (b) for $B = 10$ T and $T = 1.8$ K (blue), $B = 4$ T and $T = 1.8$ K (green) and for $B = 10$ T and $T = 9.5$ K (red). In the first case of a high magnetic field and a low sample temperature, the circular polarization degree has a local minimum at 0° and the absolute maximum of $\rho_c = 70\%$ is found for $\theta = 45°$. Both, the decrease of the magnetic field strength to $B = 4$ T (green) and the increase of the sample temperature to $T = 9.5$ K (blue) transform the local minimum to the local maximum with $\rho_c < 70\%$. As a result, the angle dependence approaches a cosine function. In all three cases, the circular polarization degree is zero in Voigt geometry ($\theta = 90°$). The

experimental results for the InAs/AlAs QW sample, presented in (d), are quite similar. However, apart from an overall lower circular polarization degree, it can be seen that the lowering around $\theta = 0°$ is broader than for the GaAs/AlAs QW. The colored lines in Fig. 5.2 show the results of fitting Eq. 5.1 to the data sets, which is discussed in the following.

The dependencies of the circular polarization degree, shown in Figs. 5.1 and 5.2 can be described by the kinetic spin model which was introduced in Ref. [31] and expanded in Ref. [42]. A summery of the theory is given in section 2.4.1. In a nutshell, the model describes the PL intensities, emitted from the circularly polarized exciton levels, as the product of the radiative recombination time τ_{rad} and the occupancies of the respective levels. The occupancies are given by the exciton recombination rates and the spin-flip rates of electron and heavy hole τ_{e} and τ_{h}. The spin-flip rates, in turn, depend on the energetic order and splitting of the four different spin states. Due to the lack of electron-hole exchange interaction in indirect band-gap heterostructures, the splitting of the bright and dark states is suppressed [30]. Thus, the fine structure of the GaAs/AlAs QW (and InAs/AlAs QW) exciton is determined only by the Zeeman terms of the Hamlitonian. In a magnetic field, the states are split depending on the strength B and direction θ of the field and the g factors of electron and heavy hole, see Eq. (2.16). The energetic splitting between the exciton spin states causes a magnetic field and temperature dependence of the spin-flip rates, which is taken to account by the Boltzmann factor.
The used fit function for the circular polarization degree is derived from the expression for strict selection rules in an arbitrary field (2.20) and the expression for weakened selection rules in Faraday geometry (2.30). It is

$$\rho_{\mathrm{c}} = \xi \frac{C^2(f_{-+} - f_{+-}) + D^2(f_{++} - f_{--}) + C_{\mathrm{d}}(f_{--} - f_{++})}{C^2(f_{-+} + f_{+-}) + D^2(f_{++} + f_{--}) + C_{\mathrm{d}}(f_{--} + f_{++})}, \tag{5.1}$$

with $C = \cos(\theta/2)$ and $D = \sin(\theta/2)$. The occupancies $f_{\pm\pm}$ are given in section 2.4.1 by Eqs. (2.26). The twelve parameters of Eq. (5.1) can be divided into eight 'internal' parameters, which describe the properties of the QW, and four 'external' parameters, which are given by the adjustments of the experimental setup. Internal parameters are the spin relaxation times τ_{e} and τ_{h}, the radiative and nonradiative exciton recombination times τ_{rad} and τ_{nr}, the g factors of electron and heavy hole, g_{e} and g_{h}, and ξ and C_{d}, which characterize the deviations from the selection rules (see end of section 2.4.1). External parameters of the model are strength B and direction θ of the magnetic field, the sample temperature T and the exciton generation rate G. Note that the actual value of the generation rate is irrelevant for the stationary experiments presented in this work.
The analysis is started with the GaAs/AlAs sample. The radiative and nonradiative exciton recombination times were already determined in Ref. [31] to $\tau_{\mathrm{rad}} = 340$ μs and $\tau_{\mathrm{nr}} = 8500$ μs. It is also adopted from this reference that the g factor of the electron $g_{\mathrm{e}} = 2$ is isotropic and that the z component of the highly anisotropic heavy-hole g factor is $g_{\mathrm{h}} > +2.5$. Time resolved measurements of the circular polarization degree, presented in Ref. [42], which are not part of this work, revealed a heavy-hole spin relaxation time of $\tau_{\mathrm{h}} = 3$ μs for the GaAs/AlAs QW. Thus, the parameters to determine are τ_{e}, g_{h}, ξ, and C_{d}.
In order to receive the highest possible accuracy of the fit parameters, the fit function was optimized for all seven data sets, presented in Fig. 5.1 (a) and Figs. 5.2 (a) and (b),

at once. In addition, the variation of the sample temperature between 1.4 and 2.2 K was permissible for the measurements at $T = 1.8$ K, since the exact determination of T is difficult in this temperature range. Under these conditions, the experimental data for the GaAs/AlAs QW are well described by the following set of parameters: $\tau_e = (69 \pm 27)$ μs, $g_h = 3.6 \pm 0.1$, $\xi = 0.71 \pm 0.03$, and $C_d = 0.0013 \pm 0.0007$. The relativly high uncertainties for τ_e and C_d are rooted in the fact that variations of the factor τ_e/τ_h and C_d cause similar changes of $\rho_c(B, T, \theta)$. This is demonstrated in the last chapter of Ref. [42]. However, these model predictions also show that variations of τ_e/τ_h and C_d have different effects on the polarization dynamics. Therefore, the inclusion of time-resolved measurements in the fitting process might reduce the uncertainties of τ_e and C_d. Of course, a higher amount of data sets should also improve the accuracy of the fit. The model curves with the presented fit parameters are shown in Fig. 5.1 (c) and Figs. 5.2 (a) and (b) by the colored lines.

The situation is more difficult for the InAs/AlAs QW sample, since almost all internal parameters are unknown. It is assumed that the g factor of the electron is $g_e = 2$, the same as for the GaAs/AlAs QW and the In(Al,As)/AlAs QD sample. From Ref. [14] it is known that the recombination rate is $9{\cdot}10^3$ s^{-1}, which includes radiative and nonradiative recombination. Thus, τ_{rad} and τ_{nr} should both be longer than 111 μs. The fitting involves six data sets, which are presented in Fig. 5.1 (d) and Figs. 5.2 (c) and (d). The procedure is the same as for the GaAs/AlAs data sets. It turns out that the experimental data can be reproduced by the model function but, unfortunately, the uncertainties of the spin-flip rates ($\tau_{e/h} \approx 10$ μs), the recombination rates ($\tau_{rad/nr} \approx 300$ μs) and of C_d ($\approx 2 \cdot 10^{-4}$) are extremely high. Thus, it is not possible to make a reliable statement about these values. However, the heavy hole g factor and the depolarization factor can be determined with satisfactory precision to $g_h = 3.1 \pm 0.1$ and $\xi = 0.58 \pm 0.06$. The model curves with the presented fit parameters are shown in Fig. 5.1 (d) and Figs. 5.2 (c) and (d) by the colored lines.

The nonmonotonic behavior of the circular polarization in a magnetic Faraday field is characterized by the field strength B_{max} of the maximal polarization degree, see Fig. 5.1 (c) and (d). B_{max} is determined by the maximum of the model function (with the respective parameters) and plotted in Fig. 5.1 (e) in dependence of the sample temperature. For both QW samples, the values for B_{max} show a linear temperature dependence and are in line with the coordinate origin. In comparison, the values for the GaAs/AlAs sample (orange symbols) show a stronger temperature dependence than for the InAs/AlAs sample (magenta symbols). The reason for the linear temperature dependence of B_{max} and for the nonmonotonic behavior itself is discussed in the following. Moreover, the origin of the two colored lines in Fig. 5.1 (e) will be explained.

5.1.2 Supplement to the kinetic spin model

To understand the physical origin of the nonmonotonic behavior of the circular polarization degree, it is necessary to take a closer look at the spin flip rates. According to Eq. (2.23), the spin-flip rates to higher energy levels are determined by the Boltzmann factors $\alpha = \exp(-g_e \mu_B B / k_B T)$, for electron spin flips, and $\beta = \exp(-g_h \mu_B B_z / k_B T)$ for hole spin flips. Thus, they depend on the strength of the magnetic field, the temperature and the g factors of electron and heavy hole. Within the model function, the Boltzmann factors reflect the order and the splitting of the spin states, which are given by Eq. (2.16).

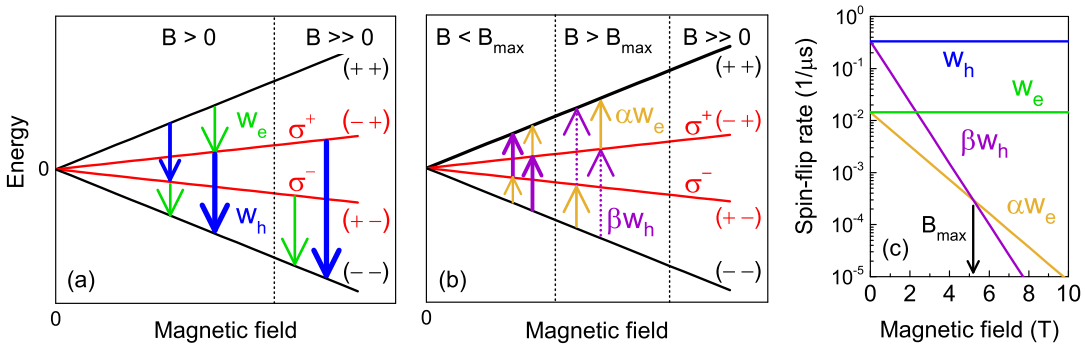

Figure 5.3: **(a)** and **(b)** Schematic representation of the fine-structure splitting of the four indirect exciton states in a magnetic Faraday field into two optically dark (black lines) and two optically bright states (red lines), $g_h > g_e > 0$. (a) Spin-flip transitions of electrons (green arrows) and heavy holes (blue arrows) to lower energy levels for weak and high field strengths. The corresponding rates are w_e and w_h. (b) Transitions of electrons (yellow arrows) and heavy holes (violet arrows) to higher energy levels for fields below and above B_{max} and for even higher fields. The corresponding rates are αw_e and βw_h. **(c)** Calculated spin-flip rates in dependence of the magnetic field strength ($B \parallel z$). B_{max} marks the crossing of αw_e and βw_h.

For the studied case of $g_h > g_e > 0$, the energetic order of the indirect-exciton spin levels in a magnetic Faraday field is shown in Figs. 5.3 (a) and (b). The two dark states, $|{+}{+}\rangle$ and $|{-}{-}\rangle$ (black lines), form the highest and the lowest states of the system. The two bright states in between, $|{-}{+}\rangle$ and $|{+}{-}\rangle$ (red lines), emit σ^+ and σ^- polarized light. Spin flips of electrons and holes are represented by the colored arrows: In (a), transitions to energetically lower states with the rates $w_e = \tau_e^{-1}$ (green) and $w_h = \tau_h^{-1}$ (blue) are shown. In (b), the transitions to higher states with the rates αw_e (yellow) and βw_h (purple) are presented.

The considerations are started for the case of Faraday geometry and a fixed sample temperature T. Figure 5.3 (c) shows the magnetic field dependence of the four different spin-flip rates for this case. w_e and w_h are independent from B and it is $w_e < w_h$. For $B = 0$ it is $\alpha w_e = w_e$ and $\beta w_h = w_h$, since all four spin levels are degenerated. In this case, the spin flips between the states do not change the occupancies in $|{-}{+}\rangle$ and $|{+}{-}\rangle$ and the circular polarization degree remains at its initial value, which is zero under nonresonant excitation, see Figs. 5.2 (a) and (c).

For zero or small fields, it is $\beta w_h > \alpha w_e$, which is shown by the purple and the yellow lines in Fig. 5.3 (c). Thus, βw_h determines the field dependence of the spin dynamics. When the field strength is increased, the rate βw_h, which causes the population of the σ^+ state and the depopulation of the σ^- state (see purple arrows in (b)), decreases. As a result, the occupation develops in favor of the σ^- level and the circular polarization degree starts to increase with a negative sign. This behavior is observed experimentally for both QW samples, see Figs. 5.1 (c) and (d). Since βw_h decreases faster than αw_e with increasing B, the two rates cross at B_{max} and it is $\alpha w_e > \beta w_h$ for $B > B_{max}$, see Fig. 5.3 (c). In this range αw_e determines the field dependence of the spin dynamics. It causes the population of the σ^- state and the depopulation of the σ^+ state, which is shown by yellow arrows in (b). Thus, the decrease of the rate αw_e (yellow line) with

increasing field strength leads to the decline the negative circular polarization degree, which is experimentally observed for $B > B_{\max}$ in Figs. 5.1 (c) and (d).
In a very strong magnetic field it is $\alpha w_e, \beta w_h \to 0$, which means that spin flips to higher energy levels can be neglected. This is illustrated in Fig. 5.3 (b) in the '$B >> 0$' area. As a result, the excitons populate the two bright states and relax to the lower dark state with the rates w_e and w_h, see '$B >> 0$' area in (a). The dark ground state $|--\rangle$ is heavily occupied with excitons where they are trapped due to the strong splitting between the states. Thus, under steady-state conditions, the circular polarization degree becomes independent of the magnetic field and is given only by the ratio of w_e and w_h. For $w_e < w_h$, the σ^- polarized state is populated stronger and the circular polarization degree saturates at a negative value, as it is observed for the two different QW samples in Figs. 5.1 (c) and (d).
In order to make a more quantitative statement, the magnetic field value at which the rates αw_e and βw_h intersect is calculated to

$$B_{\max} = \frac{k_B T \cdot \ln(\omega_h/\omega_e)}{\mu_B (g_h - g_e)}. \tag{5.2}$$

From the fitting of the GaAs/AlAs QW data, presented in this section, it is known that $w_h/w_e = 23$ and $g_h = 3.6$. Further it is $g_e = 2$. With these parameters, the function $B_{\max}(T)$ is plotted in Fig. 5.2 (c), see orange line. As this line is in very good agreement with the maxima of the model curves (orange squares), it can be stated that the position of the polarization maxima and the overall nonmonotonic field dependency is indeed determined by the intersection of αw_e and βw_h. In case of the InAs/AlAs QW sample, the determination of $B_{\max}$ can provide the unknown parameter τ_e/τ_h. The magenta line in Fig. 5.1 (c) is a linear function $B_{\max} = aT$ through the coordinate origin, fitted to the two maxima of the model curves (magenta squares). The slope of the line, $a = 2.121$ T/K, is compared with Eq. (5.2). With $g_h = 3.1$ and $g_e = 2$, the ratio of the spin relaxation times is calculated to $\tau_e/\tau_h = 4.6$. Note that Eq. 5.2 also determines a characteristic temperature $T_{\max}$ in dependence of the magnetic field strength. With the parameters for the GaAs/AlAs QW given above, $T_{\max} = 3.1$ K corresponds to the maximum of the circular polarization degree, which was determined in the temperature series (at $B = 9$ T) in Ref. [42].
The nonmonotonic angle dependency of the circular polarization degree, presented in Fig. 5.2, can be explained by the mixing of the electron spin states due to the transverse part of the magnetic field, see Eq. (2.17). In a tilted field, the exciton state $|++\rangle$ mixes with $|-+\rangle$ and $|--\rangle$ mixes with $|+-\rangle$. As a result, the dark states become optically active and contribute to the circular polarization degree. The high energetic $|++\rangle$ state starts to emit σ^+ polarized light and the low energetic $|--\rangle$ state emits σ^- polarized light. The activation of the dark states becomes important for high magnetic fields and low temperatures. In this case the dark ground state is strongly populated and the dark excited state nearly empty. Thus, already a slight deviation from the Faraday geometry leads to a strong increase of the negative circular polarization degree. The increase of the temperature as well as the decrease of the magnetic field strength reduce the effect, since the occupancies of the two dark states approach each other at high temperatures and / or low fields, compare Fig. 5.2.
In Voigt geometry ($\theta = 90°$), the electron spin states are fully mixed, which means that

all four states emit light with the same oscillator strength. Since the transverse heavy-hole g factor is negligible, the Zeeman splitting consist only of the electron term and the four energy levels are transformed into two degenerated doublets, see Eq. (2.18). In both energy levels, the two degenerated states emit σ^+ and σ^- polarized light. Due to the degeneration, the heavy hole spin-flip rates between these states are equal: $\beta w_\mathrm{h} = w_\mathrm{h}$. Therefore, the σ^+ and σ^- polarized states of the same energy level are equally occupied and the circular polarization degree is zero for all magnetic field strength and temperatures.

5.1.3 Conclusion

In conclusion, the circular polarization degree of indirect GaAs/AlAs and InAs/AlAs QW excitons shows nonmonotonic field and angle dependencies, which can be reproduced by the kinetic spin model presented in Sec. 2.4.1. The assumption of the model that the electron-hole exchange interaction can be neglected is confirmed by the good agreement of theory and experiment also in lower magnetic fields. Moreover, the same qualitative results for the type-I (InAs/AlAs) and the type-II QW (GaAs/AlAs) indicate that the suppression of the electron-hole exchange interaction is caused by the indirect band gap in momentum space. The additional impact of the spatial separation of electron and hole in the type-II structure is unclear.
However, in Ref. [95], the fine structure splitting in a direct type-I QW with a size of 50 Å is calculated theoretically to several hundreds of μeV, while in Ref. [78] experimental values for a indirect type-II GaAs/AlAs QW are about three orders of magnitude smaller for the comparable size. According to that reference, the splitting for the studied QWs with a thickness of 2 monolayers (6 Å) exceeds 20 μeV, which would affect the spin dynamics between 0 and 0.5 T. Since the magnetic field strength was increased with a step size of 2 T, a small fine structure splitting can not be excluded for the studied structures.
Anyway, the fitting of the model function to the experimental data reveals important internal parameters of the QW structures. For the GaAs/AlAs QW excitons the longitudinal heavy-hole g factor is determined to $g_\mathrm{h} = 3.6$ and the spin relaxation time of the electron to $\tau_\mathrm{e} = 69$ μs. For the InAs/AlAs QW excitons $g_\mathrm{h} = 3.1$ and $\tau_\mathrm{e}/\tau_\mathrm{h} = 4.6$ are found. The values for g_h agree with experimental results for GaAs/AlAs superlattices [78], [96]. Further, it is shown that small deviations from the selection rules, represented by the parameters ξ and C_d, are necessary to describe the experimental results.
Finally, a closer look at the magnetic field and temperature dependencies of the spin-flip rates in Faraday geometry reveals the characteristic field strength and temperature, B_max and T_max, at which the circular polarization degree reaches its maximum. This small supplement to the kinetic model provides a deeper insight into the spin dynamics of the QW.

5.2 Linear polarization dynamics

5.2.1 Experimental results and kinetic spin model

The linear polarization of the GaAs/AlAs QW emission is studied under nonresonant, pulsed excitation in steady-state and time-resolved experiments. The magnetic field is

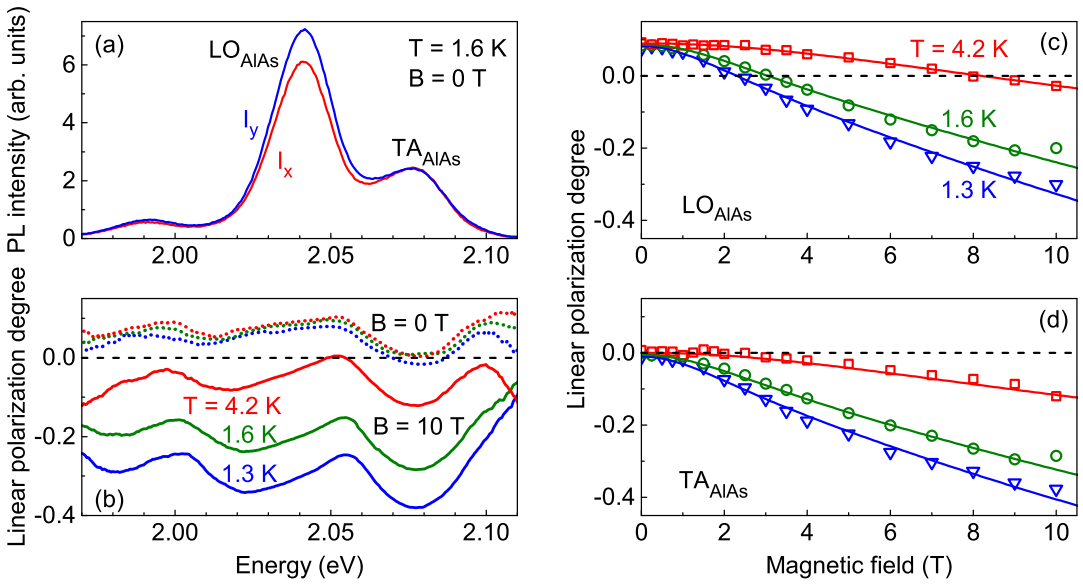

Figure 5.4: **(a)** PL spectra of the GaAs/AlAs QW with the LO_{AlAs} and the TA_{AlAs} phonon replicas. The red line shows the linear polarized I_x component with the polarization axis directed along $x \parallel [1\bar{1}0]$. The blue line represents the I_y component with the polarization axis directed along $y \parallel [110]$. **(b)** Spectral dependence of the linear polarization degree ρ_l measured for $B = 0$ (dotted lines) and $B = 10$ T (solid lines) in Voigt geometry. The colors indicate the sample temperature. The dashed line marks $\rho_l = 0$. **(c)** and **(d)** Linear polarization degrees of the LO_{AlAs} and the TA_{AlAs} emission lines in dependence of the transverse magnetic field strength, measured for different temperatures. The colored lines show the results of fitting Eq. (2.33) to the data sets.

applied in Voigt geometry and the linear polarization degree is determined via Eq. (3.2). Since the directions of the sample axes, $x \parallel [1\bar{1}0]$ and $y \parallel [110]$, are aligned vertically and horizontally, the respective polarized intensity components, I_0 and I_{90}, are denoted as I_x and I_y in the following. The diagonal components, I_{45} and I_{135}, are denoted as $I_{x'}$ and $I_{y'}$.

Figure 5.4 shows the results of the steady-state experiments for different temperatures and magnetic field strengths. In Fig. 5.4 (a), the PL spectra of the linearly polarized intensity components I_x (red) and I_y (blue) are presented for $T = 1.6$ K and $B = 0$. At the spectral position of the LO_{AlAs}-phonon replica the PL intensities differ clearly, while they are the about same for the TA_{AlAs}-phonon line. The difference of the diagonal components $I_{x'}$ and $I_{y'}$ is much weaker (not shown here). Thus, for the LO_{AlAs}-phonon line the intrinsic linear polarization degree ρ_{int} is calculated to 8.5% and to 1.0% for the TA_{AlAs} line. The related polarization spectrum is shown in Fig. 5.4 (b) by the dotted green line. For $B = 0$, the linear polarization degree depends only weakly on the temperature, as it can be seen by the dotted red and the blue lines for $T = 4.2$ K and $T = 1.3$ K. When a magnetic field of 10 T is applied (solid lines), the linear polarization degree changes the sign for the whole spectral range and becomes strongly temperature dependent. However, the overall shape of the polarization spectra is preserved for the changes in temperature and magnetic field strength.

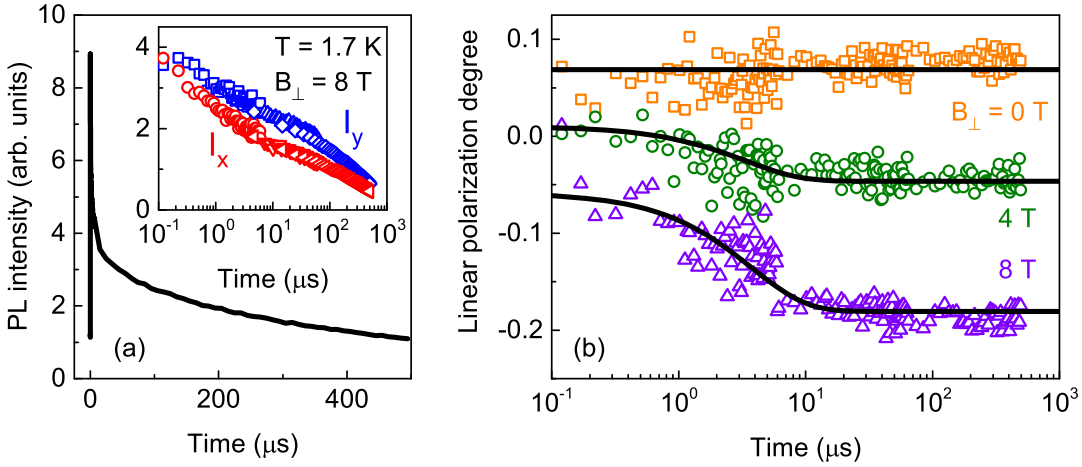

Figure 5.5: **(a)** Dynamics of the PL intensity of the LO_{AlAs} phonon line for $B_\perp = 8$ T. Inset: Dynamics of the linear polarized components I_x (red) and I_y (blue) with the polarization axes directed along $x \parallel [1\bar{1}0]$ and $y \parallel [110]$. **(b)** Linear polarization degree in dependence of the time after the excitation pulse, measured for $B = 0$ (orange), $B_\perp = 4$ T (green) and $B_\perp = 8$ T (purple). The black lines show the results of fitting Eq. (2.36) to the data sets.

The magnetic field dependence of the linear polarization degree, measured at different temperatures, is shown in Figs. 5.4 (c) and (d) for the LO_{AlAs} and TA_{AlAs} lines. For both PL lines, the linear polarization degree (colored symbols) follows a quadratic function of the transverse magnetic field, where the slope depends on the sample temperature. The strongest increase is observed for the lowest temperature, while a higher temperature causes a weaker field dependence. In contrast to the TA_{AlAs} line with a linear polarization degree of zero at $B = 0$, the intrinsic polarization of the LO_{AlAs} line is $\rho_{int} = +10\%$.

The results of the time-resolved experiments are presented in Fig. 5.5. Here, the analysis is limited to the results of the LO_{AlAs} line, since the study of the TA_{AlAs} line does not provide further information. In Fig. 5.5 (a), the dynamics of the PL intensity is observed on a timescale of several hundred microseconds for $T = 1.7$ K and $B = 8$ T. The dynamics of the related linear polarized PL components I_x and I_y are presented in the inset and the derived linear polarization degree is plotted in Fig. 5.5 (b) by purple symbols. For $B = 8$ T, the linear polarization increases from -6% to -18% within about 10 μs and remains constant at this value until the end of the measurement at $t = 500$ μs. For $B = 4$ T (green symbols), the initial polarization is about 0% and the increase is comparably low. After $t = 10$ μs the linear polarization degree reaches its final value of -4.5%. For $B = 0$ (orange symbols), the linear polarization degree increases slightly within the same time from 5% to 8%.

The fact that the PL emission is linearly polarized in absence of a magnetic field gives important information about the symmetry of the QW structure. In principle, two kinds of point symmetry groups are possible for QWs that are grown from a zinc-blende lattice material along the [001] axis. The D_{2d} group describes QWs with a symmetric poten-

tial while the C_{2v} group is suitable for asymmetric potentials e.g. due to nonequivalent interfaces or elastic strain [22], [52]. As the rotoreflection axis $S_4 \parallel z$ of the D_{2d} group prohibits the occurrence of intrinsic linear polarization, the studied QW can be assigned to the C_{2v} group. Here, the intrinsic linear polarization is the result of heavy and light hole mixing, caused by strain and nonequivalent interfaces (see Sec. 2.4.2).
The magnetic field induced linear polarization of the QW PL is due to the mixing of electron and hole states in the transverse field. The mixing of the holes states requires a finite in plane g factor, which is given by the heavy-hole and light-hole mixing in the C_{2v} QW. By calculating the exciton-spin system as the tensor product of the two carrier-spin systems, it can be shown that the dark exciton states become vertically polarized and the bright states become horizontally polarized in the transverse magnetic field and that the oscillator strength is the same for all four states. Due to the finite in-plane g factor of the hole, the oppositely polarized states are split be the Zeeman term of the hole. The resulting linear polarization degree and its transverse magnetic field dependency can be described by Eq. (2.33), which is part of the kinetic spin model for the indirect GaAs/AlAs QW, see section 2.4. Further symmetry considerations and experiments in Ref. [43], which are not part of this work, reveal that the in-plane components of the hole g-factor tensor are given by the relations $|g_{xx}| = |g_{yy}|$ and $g_{xx} = -g_{yy}$. In the following section, the g factor of the hole is referred to as g_{yy} since the magnetic field is applied in y direction.

The linear polarization degree can be modeled by Eq. (2.33) with two external and seven internal parameters. External parameters are the strength of the transverse magnetic field B and the sample temperature T. Internal parameters are the spin-flip rates, τ_e and τ_h, and the in-plane g factors, $g_\mathrm{e} = g_{yy}^{(\mathrm{e})}$ and $g_{yy}^{(\mathrm{h})}$, of electron and hole, the radiative and nonradiative recombination rates of the exciton, τ_rad and τ_nr, and the intrinsic linear polarization degree ρ_int. From the studies of the circular polarization degree in Sec. 5.1, most of the internal parameters are already known. They are $\tau_\mathrm{e} = 69$ μs, $\tau_\mathrm{h} = 3$ μs, $g_\mathrm{e} = 2$, $\tau_\mathrm{rad} = 340$ μs and $\tau_\mathrm{nr} = 8500$ μs. Thus, only the in-plane component of the hole g factor $g_{yy}^{(\mathrm{h})}$ and the intrinsic linear polarization degree ρ_int are used as internal fitting parameters. Since the exact determination of the sample temperature is difficult, T is used as an additional fitting parameter with relatively narrow limits.
The model function is fitted to the steady-state data sets of the linear polarization degree, presented in Fig. 5.4 (c) and (d), which were measured for the $\mathrm{LO_{AlAs}}$ and the $\mathrm{TA_{AlAs}}$ lines at three different temperatures each. Since it is assumed that $g_{yy}^{(\mathrm{h})}$ is constant for the studied temperature range ($\sim 1-5$ K) and has no spectral dependence, this parameter is optimized for all six data sets at once. It is given by $g_{yy}^{(\mathrm{h})} = -0.18 \pm 0.02$. In contrast, the intrinsic linear polarization ρ_int is fitted individually for each data set. It varies between 8.4% and 9.2% for the $\mathrm{LO_{AlAs}}$ line and between -0.9% and 0.2% for the $\mathrm{TA_{AlAs}}$ line. With increasing temperature, ρ_int is shifted to higher positive values. The fitted model curves are shown in Fig. 5.4 (c) and (d) by the colored lines for the respective temperatures.
For the analysis of the linear polarization dynamics, presented in Fig. 5.5 (b), the simplified spin model, which is summarized in section 2.4.2, is applied. In this model, the linear polarization degree is given by the product of the mean spins of electrons and holes. Equation (2.36) describes the polarization dynamics as a exponential decay from the initial to the thermal spin polarization. External parameters of the model function

are the time t after the laser pulse, the strength of the transverse magnetic field B and the temperature T. Internal parameters are the spin-flip rates, τ_e and τ_h, the in-plane g factors, g_e and $g_{yy}^{(\mathrm{h})}$, and the initial polarizations, ρ_e^0 and ρ_h^0 of electrons and holes, and finally the intrinsic linear polarization ρ_int. As mentioned above, τ_e, τ_h and g_e are already known and $g_{yy}^{(\mathrm{h})}$ is determined to -0.18 ± 0.02 in this section. However, in order to verify this result, $g_{yy}^{(\mathrm{h})}$ is used again as a fitting parameter. Further fitting parameters are ρ_e^0 and ρ_h^0, which can range between -1 and 1, and ρ_int (and T within narrow limits).
The model function, Eq. (2.36), is fitted to the time-resolved linear polarization degree, which was measured for the $\mathrm{LO_{AlAs}}$ line at three different field strengths, see Fig. 5.5 (b). Since it is assumed that the fit parameters are independent from B, they are optimized for all three data sets at once. It turns out that the best result is achieved when ρ_e^0 is set to 1. In this case, the other fit parameters are optimized to $g_{yy}^{(\mathrm{h})} = -0.16 \pm 0.03$, $\rho_\mathrm{h}^0 = 0.51 \pm 0.03$ and $\rho_\mathrm{int} = (6.9 \pm 0.2)\%$ and the experimental data are reproduced well by the model function, see black lines in Fig. 5.5 (b).

5.2.2 Conclusion

In conclusion, the intrinsic and the magnetic field induced linear polarization of the exciton PL can be explained by the C_{2v} point symmetry of the studied GaAs/AlAs QW. Strain and nonequivalent interfaces cause the mixing of heavy and light holes, which lead to intrinsic linear polarization and to a finite in-plane g factor of the hole. In a transverse magnetic field, the latter causes the mixing of the hole states. The mixing of electron and hole states in Voigt geometry leads to the formation of linearly polarized states. The magnetic field and temperature dependence of the linear polarization degree can be modeled by the kinetic spin model, presented in 2.4.2. A simplified spin model is used to describe the dynamics. With the spin relaxation and exciton recombination times obtained in the section above, both models nicely reproduce the experimental data and deliver consistent results for the in-plane g factor of the hole with an average value of $g_{yy}^{(\mathrm{h})} = -0.17 \pm 0.02$. The intrinsic linear polarization ρ_int, a steady-state parameter, depends on the sample temperature and the phonon replica and ranges between -1% and 10%. The initial polarization of electrons and holes, $\rho_\mathrm{e}^0 = 1$ and $\rho_\mathrm{h}^0 = 0.51 \pm 0.03$, obtained in the energy relaxation process, are crucial parameters of the dynamics.

6 Results II: (In,Al)As/AlAs quantum dot ensemble

(In,Al)As/AlAs QDs with an indirect band gap in momentum space were originally examined due to their prolonged exciton recombination time [39], [29], which makes these structures interesting for spintronic applications. However, the fascinating physics of the indirect excitons lead to the investigation of the exciton fine structure, thermal redistribution processes and the hyperfine interaction. These studies are presented in this chapter, which is organized as follows:
Section 6.1 provides an overview about the PL spectrum of the QD ensemble. For this purpose, PL signals of direct and indirect excitons are studied in dependence of excitation energy, temperature and indium concentration. A deeper insight to the energetic structure and the thermal redistribution between different states is given in Sec. 6.2, in which the PL dynamics are investigated. The lack of electron-hole exchange interaction for indirect excitons is demonstrated in Sec. 6.3 by the observation of optical orientation. Moreover the impact of the ΓX splitting on the spin dynamics is discussed. The suppression of the electron-hole exchange interaction for indirect excitons is also demonstrated in Sec. 6.4 by the measurement of the anisotropic exchange splitting in the spectral range of the ΓX mixing. The hyperfine interaction of the indirect exciton and other depolarization mechanisms, leading to the decrease of the optical orientation, are studied in Sec. 6.5. Finally, a first attempt to study the spin dynamics of indirect excitons under selective excitation is presented in Sec. 6.6.

6.1 Direct and indirect exciton states

Due to the ensemble structure of the studied (In,Al)As/AlAs QD samples, excitons can be created in QDs with a specific size by selective excitation. As the transition between direct and indirect QDs occurs at a certain QD size (see Sec. 4.2.2), the energy structure serves as a map that is indispensable for the investigation of all further sample properties. In this regard, the energies of the valence and conduction bands were studied theoretically in dependence of the QD size and the indium fraction in Ref. [26], see Sec. 4.2.2. In Ref. [29] and [70], the ΓX-transition energies were determined experimentally for sample AG 2890, see Fig. 4.2 (c).
In this section, a full overview of all detected PL features is given for the samples AG 2890 and RC 1517 as well as the ΓX-transition energies for sample RC 1517. The D line, close to the direct transition in the PL spectra, and further PL features are investigated. Moreover, the thermal redistribution between direct and indirect states is studied. In order to describe the impact of the indium concentration x on the X exciton energy, a simple particle in a box model is applied and discussed.
All experiments presented in this section are steady-state measurements under selective cw excitation in absence of a magnetic field.

6.1.1 Photoluminescence spectra under selective excitation

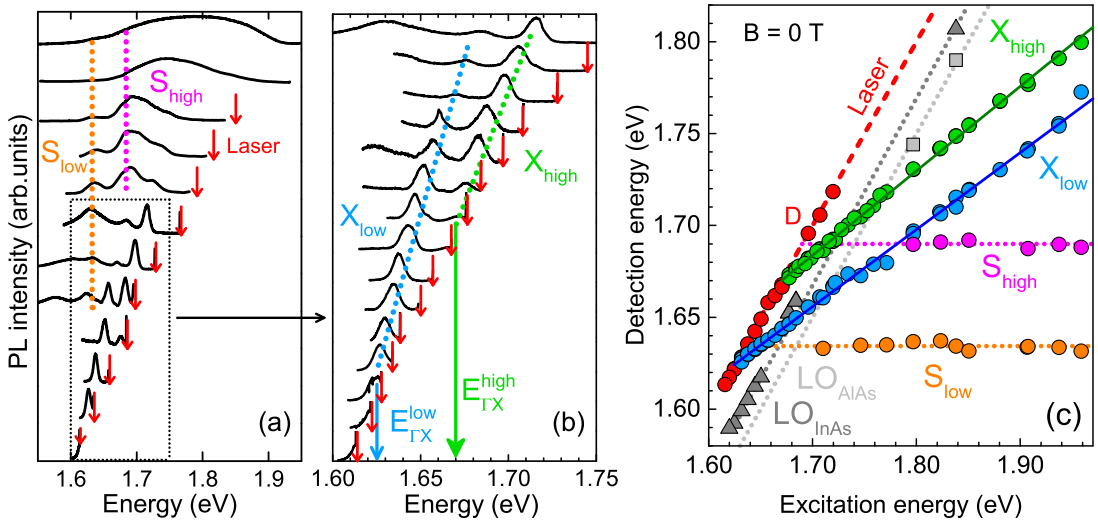

Figure 6.1: **(a)** PL spectra of the (In,Al)As/AlAs QD ensemble (sample AG 2890) for different excitation energies, indicated by the red arrows. $T = 2$ K. Colored, dotted lines mark the static PL features S_{low} and S_{high}. **(b)** Detailed evolution of the PL spectra in the spectral region between 1.60 and 1.75 eV. Dotted lines trace the shifts of the X_{low} (blue) and X_{high} (green) exciton lines emitted by indirect QDs. ΓX-transition energies are found at $E_{\Gamma X}^{low} = 1.624$ eV and $E_{\Gamma X}^{high} = 1.670$ eV, marked by the blue and green arrows. **(c)** PL-peak energies of all known features of the QD spectra in dependence of the excitation energy. The red, dashed line shows the laser line, red dots the signal of the D line. LO_{InAs} and LO_{AlAs} phonon replicas are shown by the grey triangle and square symbols. Dotted lines are guides for the eye. The blue and green solid lines show linear fits to the X_{low} and X_{high} data points, see Eqs. (6.4) and (6.5). Some data points are adapted from Ref. [70], compare Fig. 4.2 (c).

For a systematic study of the energy structure, PL spectra are detected while the laser energy is scanned through the spectral region of the QD emission. This range is limited by the band gap of the GaAs substrate, emitting at 1.52 eV, and by the AlAs barrier at 2.30 eV. For higher energies, the excitation process becomes nonresonant and the shape of the spectrum does not change further with increasing laser energy. For sample AG 2890, the results of the scan are presented in Fig. 6.1. The development of the PL spectrum with increasing laser energy, indicated by the red arrows, is shown in (a) and (b). Several PL lines are observed. In (c), the peak energies of the PL features are plotted in dependence of the excitation energy. This figure is an extension of Fig. 4.2 (c), which is adapted from Ref. [70]. The extension contains the static PL features S_{low} (orange) and S_{high} (magenta) and several additional data points of the indirect exciton lines X_{low} (blue) and X_{high} (green). In addition, Fig. 6.2 shows two wide PL spectra, covering the spectral range between the substrate emission at 1.52 eV and the laser line. In these spectra nearly all PL features can be observed at once. For simplification, the PL features are categorized in three different groups: Direct, indirect and further PL features.

The direct PL features (D line, LO phonon replicas) stem from the recombination of direct excitons, i.e. from the recombination of electrons and heavy holes in the Γ valleys of the conduction and the valence band respectivly. As the emission energy of the direct recombination is equal to the excitation energy, the direct PL line is covered by the laser line. However, the QD spectrum exhibits a spectral broadening on both sides of the laser line, see Figs. 6.2, 6.3 and 6.4. In Sec. 6.1.2, this broadening will be identified as the acoustic phonon sideband of the direct zero-phonon line. In the following, the acoustic phonon sideband is referred as 'D line' ('D' in figures), as it represents the emission of direct QDs in the spectra. The spectral position of the D line (red dots) is plotted in Fig. 6.1 (c) in dependence of the excitation energy. The laser emission is indicated by the dashed red line. Further direct PL features are the optical phonon replicas, $\mathrm{LO_{InAs}}$ (grey triangles) and $\mathrm{LO_{AlAs}}$ (grey squares), which were identified in Ref. [70].
The indirect PL features, denoted as X_{low} (blue) and X_{high} (green), appear when the excitation energy E_{exc} exceeds the ΓX-transition energies $E_{\Gamma X}^{\mathrm{low}}$ and $E_{\Gamma X}^{\mathrm{high}}$, see Fig. 6.1 (b). At $E_{\Gamma X}^{\mathrm{low}} = 1.624$ eV the X_{low} line (blue) splits off from the laser line and for $E_{\mathrm{exc}} > 1.67$ eV the second indirect line X_{high} (green) appears. Both emission lines are the result of exciton recombination in indirect QDs, i.e. the recombination of electrons in the X valley with heavy holes in the Γ valley. The spectral distance between the indirect PL lines and the laser line, $\Delta E_{\Gamma X}$, increases with increasing excitation energy, as it can be seen by the blue and green data points in Fig. 6.1 (c). The blue and green lines represent linear fits of the data points, which are given by Eqs. (6.4) and (6.5). The ΓX-transition energies are calculated from these fits. In Sec. 6.1.4, the relation between the slope of these lines and the indium concentration of the QDs is discussed.
Further PL features are the two lines $\mathrm{S_{low}}$ (orange) and $\mathrm{S_{high}}$ (magenta), which are static in their spectral positions close to the ΓX-transition energies. The PL maximum of $\mathrm{S_{low}}$ is at $E = 1.634$ eV and it becomes visible for excitation energies above 1.7 eV. $\mathrm{S_{high}}$ appears for excitation energies above 1.8 eV at $E = 1.690$ eV, see Fig. 6.1 (a). Finally, a broad PL band is observed in the low energy part of the spectra, presented in Fig. 6.2. As the PL feature is more than 100 meV below the laser energy the excitation process is assumed to be nonresonant and the feature is referred as NR band.

In Fig. 6.2, nearly all known PL features of the (In,Al)As QD ensemble are visible at once. The excitation energy is $E_{\mathrm{exc}} = 1.70$ eV in (a) and $E_{\mathrm{exc}} = 1.73$ eV in (b). The spectra are detected for different sample temperatures between 12 and 70 K. The color gradient clearly shows that the X_{low} and $\mathrm{S_{low}}$ lines have the same temperature dependence which is also the strongest decrease in the whole spectrum. This behavior can be observed for both excitation energies. In contrast, the intensity of the D line increases with increasing temperature. This effect is studied in Sec. 6.1.3. The NR band is temperature stable up to 70 K. Moreover, it is possible to see the spreading of the NR band with increasing excitation energy. The peak of this PL feature shifts to higher energies and the integral intensity increases. In the high energy range, for excitation energies above 1.8 eV, $\mathrm{S_{low}}$, $\mathrm{S_{high}}$ and NR start to dominate the PL spectrum, see Fig. 6.1 (a).
The origin of $\mathrm{S_{low}}$, $\mathrm{S_{high}}$ and NR is not understand yet but the emission energies of $\mathrm{S_{low}}$ and $\mathrm{S_{high}}$ indicates that these PL features are connected with the ΓX-transition energies. A possible explanation for these two features could be a cascading reabsorption process between different QDs. When a X-valley exciton recombines, the created photon can ei-

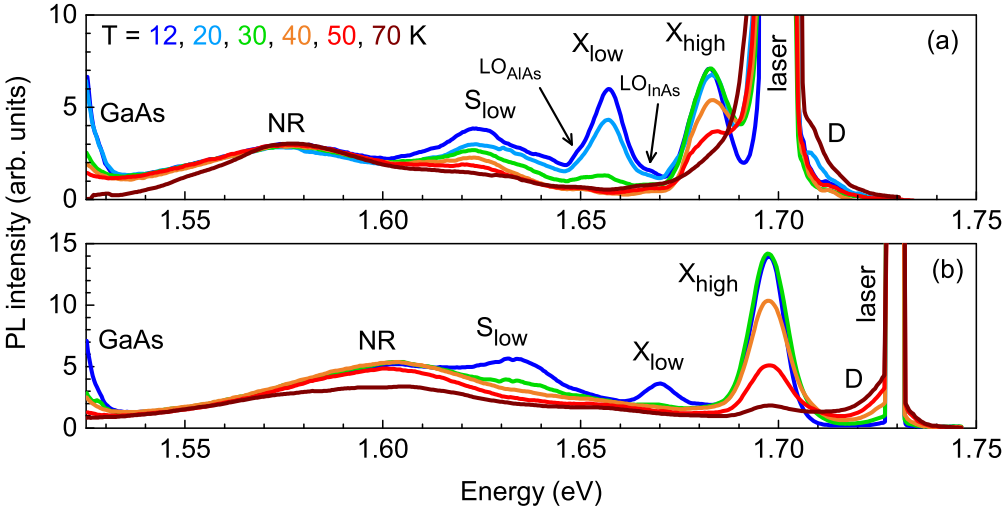

Figure 6.2: Full PL spectra of indirect (In,Al)As/AlAs QDs under selective excitation for different temperatures between 12 and 70 K. The laser energy is **(a)** $E_{\mathrm{exc}} = 1.70$ eV and **(b)** $E_{\mathrm{exc}} = 1.73$ eV. The spectra contain the emissions from the GaAs substrate, the NR band, the static line $\mathrm{S_{low}}$, the optical phonon replicas $\mathrm{LO_{InAs}}$ and $\mathrm{LO_{AlAs}}$ (only in (a)), the two indirect PL lines X_{low} and X_{high} and the D line.

ther be emitted by the sample and detected as PL or it can be reabsorbed in the sample creating a direct exciton in a larger QD. In case of a second indirect QD the electron will relax to the X valley and the process continues until the size of the dot corresponds to $E_{\Gamma X}$. However, the PL features are detected for the multi-layer sample AG 2890 as well as for the single-layer sample RC 1517, see Fig. 6.5 (a). In the latter one the effect of reabsorption should be much smaller than in the multi-layer sample, which is not reflected in the experimental results. Therefore, the origin of these features remains unknown.

6.1.2 Direct recombination: The D line

Under selective excitation, the PL emission of the Γ exciton is covered by the laser emission. Only side bands of the Γ line are detectable next to the laser line. In Ref. [29], the side band on the low energy side is denoted as the acoustic phonon replica of the Γ-exciton recombination. However, since the identification of this line is crucial for the following sections, it will now be examined in detail.
The D line is investigated in dependence of the excitation energy and the temperature. In Fig. 6.3 (a), the laser energy is varied from 1.590 to 1.626 eV. With increasing excitation energy, the spectral distance ΔE between the laser and the D line increases, see (b). At the same time, the peak intensity of the D line roughly doubles. A small anti-Stokes contribution is observed on the high energy side of the laser that increases in intensity in the same way. For $E_{\mathrm{exc}} = 1.626$ eV, which is above the ΓX-transition energy $E_{\Gamma\mathrm{X}}^{\mathrm{low}}$, the shape changes from a Lorentz to an asymmetric shape, probably due to the contribution of the X_{low} line, and the anti-Stokes contribution decreases strongly. For $E_{\mathrm{exc}} = 1.620$ eV, an increase of the temperature from 10 to 35 K leads to a more symmetric emission regarding the laser line and the width increases from 5 to 7 meV,

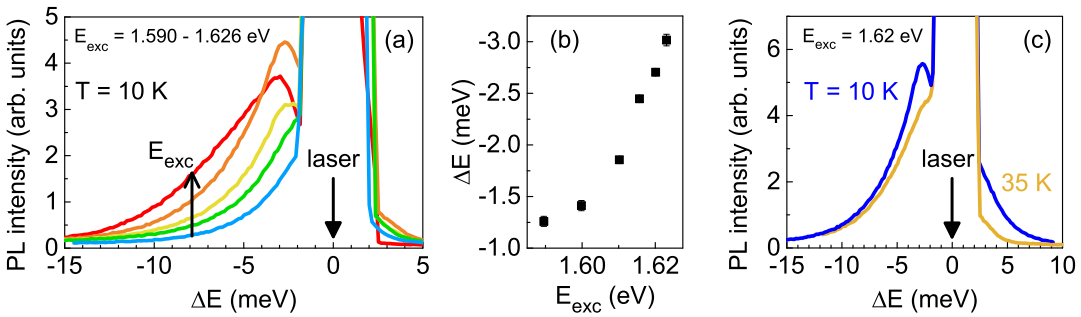

Figure 6.3: D line of the (In,Al)As/AlAs QD spectrum under selective excitation. In **(a)** (and (c)) the PL intensity is plotted in dependence of ΔE, which is the shift from the laser energy. Blue line: $E_{\mathrm{exc}} = 1.590$ eV, green: 1.610 eV, yellow: 1.616 eV, orange: 1.620 eV, red: 1.626 eV **(b)** Spectral shift of the D line with respect to the laser energy. $T = 10$ K. **(c)** D line at two different temperatures. $E_{\mathrm{exc}} = 1.620$ eV.

see Fig. 6.3 (c).
Due to its dependencies on excitation energy and temperature, the D line can be identified as the acoustic phonon sideband of the direct recombination, caused by inelastic exciton-phonon coupling in the QDs. These relations are explained in the following. An exciton, or electron-hole pair, creates a local net charge which results in the deformation of the lattice. Therefore, the recombination of electron an hole is accompanied by the emission of an acoustic phonon and the relaxation of the lattice [97]. This effect leads to a low energy sideband in the PL spectrum below the zero-phonon line of the exciton. At higher temperatures, the probability of phonon absorption increases and approaches the phonon emission rate, leading to symmetric sidebands, as it is observed in Fig. 6.3 (c). In larger QDs, the spatial extension of the exciton wave function shifts the spectral density of the phonon-coupling towards the zero-phonon line [97]. As a result, the phonon sideband is shifted to higher energies with increasing QD size (here: decreasing excitation energy). Moreover, the shapes of the measured PL spectra in Figs. 6.3 (a) and (c) are quite similar to the calculated spectra for single GaN/AlN quantum dots by Ostapenko et al. [97]. They also show the same spectral dependencies concerning the dot size (here: excitation energy) and temperature.

6.1.3 Thermal redistribution

When comparing the results so far, it is noticeable that the temperature dependence of the D-line intensity depends on the type (direct / indirect) of the studied QD, compare Figs. 6.2 and 6.3 (c). This behavior is examined in more detail in this section.
First, the temperature dependence of the D line emitted by large direct QDs is compared with the situation of smaller indirect QDs. In Fig. 6.4 (a), the PL intensity of the D line, emitted by direct QDs, is presented for different temperatures. The laser energy is $E_{\mathrm{exc}} = 1.619$ eV. Between 10 and 70 K the D line drops monotonically to 20% of the initial value. The situation is different for indirect QDs, excited with a laser energy of $E_{\mathrm{exc}} = 1.651$ eV, as shown in Fig. 6.4 (b). The ΓX splitting between the laser and the X_{low} line is $\Delta E_{\Gamma X}^{\mathrm{low}} = 17$ meV. At low temperature ($T = 10$ K), the intensity of the X_{low} line is much higher than the intensity of the D line. When the temperature is increased,

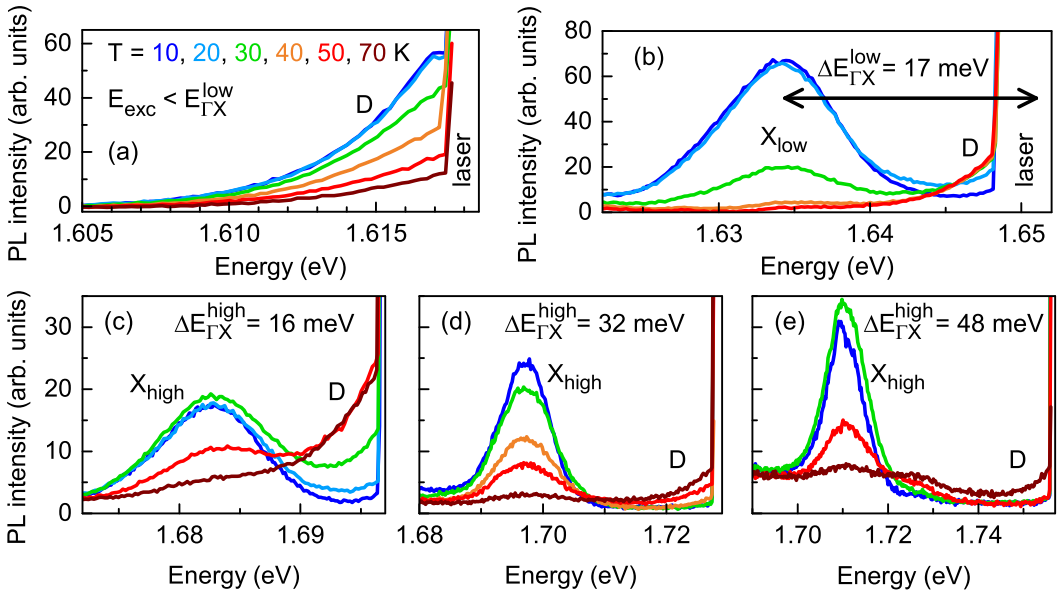

Figure 6.4: Temperature development of the QD PL spectra under selective excitation: **(a)** D line emitted by direct QDs for $E_{\mathrm{exc}} = 1.619$ eV, **(b)** D line and X_{low} line emitted by indirect QDs for $E_{\mathrm{exc}} = 1.651$ eV, $\Delta E_{\Gamma X}^{\mathrm{low}}$ is the spectral distance between the laser and the X_{low} line, **(c)** - **(e)** D line and X_{high} line emitted by indirect QDs for (c) $E_{\mathrm{exc}} = 1.698$ eV, (d) $E_{\mathrm{exc}} = 1.729$ eV and (e) $E_{\mathrm{exc}} = 1.759$ eV. $\Delta E_{\Gamma X}^{\mathrm{high}}$ is the spectral distance between the laser and the X_{high} line.

the intensity of the indirect X_{low} line decreases, while the intensity of D line increases. Between 20 and 30 K, X_{low} decreases strongly and becomes smaller than the D line for $T \geq 30$ K. The comparison with (a) shows that X_{low} is more sensitive to temperature changes than the D line in direct QDs.

In a second step, the temperature behavior of the D line is studied in dependence off the ΓX splitting. Figures 6.4 (c)-(e) show the PL spectra for three different excitation energies. In order to vary the ΓX splitting $\Delta E_{\Gamma X}$ over a larger range, the X_{high} line is selected for this experiment. In (c), the laser energy is $E_{\mathrm{exc}} = 1.698$ eV and the ΓX splitting, measured between the laser and the X_{high} line, is $\Delta E_{\Gamma X}^{\mathrm{high}} = 16$ meV. The increase of the temperature causes the decrease of the X_{high} line and a strong increase of the PL intensity at the spectral position of the D line. Although the relative increase in (c) is higher than for the situation in (b), with a comparable ΓX splitting, at $T = 50$ K the absolute intensities of the D line are the same in both cases. In (d) the laser energy is $E_{\mathrm{exc}} = 1.729$ eV and the ΓX splitting is $\Delta E_{\Gamma X}^{\mathrm{high}} = 32$ meV. When the temperature is increased to $T \geq 50$ K, the intensity of the D line starts to increases, but only sightly in comparison with (a). For an even larger ΓX splitting, $\Delta E_{\Gamma X}^{\mathrm{high}} = 48$ meV for $E_{\mathrm{exc}} = 1.759$ eV in (e), the PL intensity of the D line does not increase for $T \leq 50$ K. Only for $T = 70$ K it is slightly increased, comparable to the situation in (d).

Another finding that can be drawn from the results in Fig. 6.4 is that the decrease of the X_{high} line is much slower than the decrease of the X_{low} line with increasing temperature, compare (b) and (c). Starting from the PL intensity at 10 K, the X_{low} line is reduced to about one third for $T = 30$ K (green), while the PL intensity of the X_{high} line is even

increased for this temperature. Only between 50 and 70 K (red and wine) the X_{high} line is reduced to one third of its 10 K value.

In direct QDs, like shown in Fig. 6.4 (a), the decrease of the D line can be explained by the shift of the acoustic phonon sideband to higher energies (see Sec. 6.1.2) and also by nonradiative decay channels which gain in importance at higher temperatures [98], [99]. In indirect QDs, the electrons can relax from the Γ to the lower lying X valley, which leads to the reduction of the D-line intensity, compare Figs. 6.4 (a) and (b) for $T = 10$ K (blue lines). When the temperature is raised, the intensity of the X_{low} line in (b) decreases faster than the D line in direct QDs, see (a). This indicates either a more effective, nonradiative energy transfer or an additional decay channel. At the same time, the existence of the energetically lower X level leads to the increase of the D line when the temperature is raised, see (b). Moreover, the increase of the D line is reduced for larger ΓX splitting, see (d) and (e). All these effects can be explained by the assumption that X electrons are thermally excited to the direct energy level. Further evidence for this explanation can be found in the third part of Sec. 6.2.2, where the impact of the temperature increase on the recombination dynamics is discussed.
The reason for the different temperature dependencies of the two indirect exciton lines, X_{low} and X_{high}, is not understand so far. The comparison of Figs. 6.4 (b) and (c) indicates that the thermal electron redistribution from the X_{high} to the Γ level might be more efficient than from the X_{low} level, since the PL decrease of the X_{high} line is much weaker. Thus, further studies of the temperature dependence might help to understand the reason for the existence of two indirect PL lines.

6.1.4 Influence of the indium concentration - Particle in a box model

In the previous sections it is already demonstarted that the spectral distance between the laser (Γ line) and the indirect exciton lines, X_{low} and X_{high}, increases with increasing excitation energy E_{exc}, see Fig. 6.1 for sample 2890. Figure 6.5 (a) shows this behavior for sample RC 1517 by the blue and green symbols and gives an overview about the spectral energies of the PL features at different excitaion energies. The ΓX-transition energies for sample RC 1517 can be determined to $E_{\Gamma X}^{\mathrm{low}} = 1.611$ eV and $E_{\Gamma X}^{\mathrm{high}} = 1.657$ eV. In order to describe the different energy levels, calculations of the conduction- and valence-band levels by the simple band effective mass approach under consideration of strain, deformation and the nonparabolic electron dispersion were presented in Ref. [26]. However, the aim of this section is to find a simple model to describe the relation $E_{\mathrm{X}}(E_{\mathrm{exc}})$ for the indirect PL lines.

In the particle in a box model, the energy of the electron (hole) in a confining potential is given by the effective mass m^* of the carrier and the size L of the confinement [15], see Eq. (2.2). For the indirect exciton X the energy is given by:

$$E_{\mathrm{X}} = \frac{1}{2m_{\mathrm{X}}^*}\left(\frac{\hbar\pi}{L}\right)^2 + E_{\mathrm{gap,X}}, \tag{6.1}$$

where $E_{\mathrm{gap},X}$ is the energy gap between the X valley of the conduction band and the Γ valley of the valence band. The excitation energy E_{exc} for the indirect exciton is equal

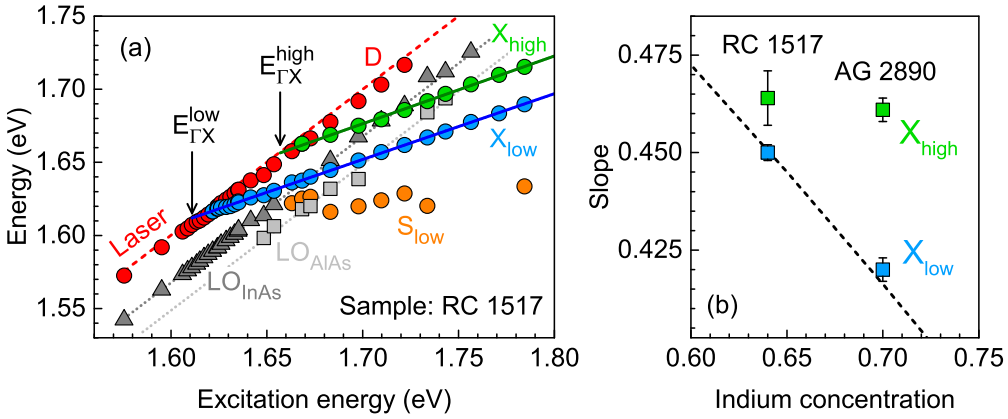

Figure 6.5: **(a)** PL peak energies of the QD spectrum of sample RC 1517 in dependence of the excitation energy. Description of the PL features is analogue to sample AG 2890 in Sec. 6.1.1. The ΓX-transition energies are at $E_{\Gamma X}^{\text{low}} = 1.611$ eV and $E_{\Gamma X}^{\text{high}} = 1.657$ eV. The green and blue lines show the fit functions (6.6) and (6.7). **(b)** Relation between the slope of the indirect PL line and the indium concentration x of the QDs. The colored symbols show the experimentally determined slopes of the X_{low} (cyan) and the X_{high} lines (green) with the respective, nominal indium concentrations of the two studied samples. The dashed line shows the slope a_X as a function of the indium concentration, which results from Eq. (6.9) of the particle in a box model. No fitting parameters are used.

to the energy E_Γ of the direct exciton state in this QD. E_Γ can also be described by the particle in a box model via:

$$E_{\text{exc}} = E_\Gamma = \frac{1}{2m_\Gamma^*}\left(\frac{\hbar\pi}{L}\right)^2 + E_{\text{gap},\Gamma}, \tag{6.2}$$

where $E_{\text{gap},\Gamma}$ is the energy gap between the Γ valley of the conduction band and the Γ valley of the valence band. The combination of both equations results in:

$$E_{\text{X}}(E_{\text{exc}}) = \underbrace{\frac{m_\Gamma^*}{m_{\text{X}}^*}}_{\text{slope } a_X} E_{\text{exc}} + \underbrace{E_{\text{gap,X}} - \frac{m_\Gamma^*}{m_{\text{X}}^*} E_{\text{gap},\Gamma}}_{\text{intercept}}. \tag{6.3}$$

Here, the indirect exciton energy E_{X} is a linear function of the excitation energy E_{exc}. The slope, denoted with a_X in the following, is given by the ratio of the effective masses of the Γ and the X exciton. The expression for the intercept includes also the gap energies.

The linear function (6.3) is fitted to the experimental data for sample AG 2890 in Fig. 6.1 (b) and sample RC 1517 in Fig. 6.5 (a). For AG 2890, the fit functions are given by

$$E_{\text{X}}^{\text{low}} = 0.420 \cdot E_{\text{exc}} + 0.942 \quad \Rightarrow \quad a_X^{\text{low}} = 0.420 \pm 0.003, \tag{6.4}$$

$$E_{\text{X}}^{\text{high}} = 0.461 \cdot E_{\text{exc}} + 0.901 \quad \Rightarrow \quad a_X^{\text{high}} = 0.461 \pm 0.003, \tag{6.5}$$

	m^* in InAs		m^* in AlAs	
	Γ valley	X valley	Γ valley	X valley
electron	0.026 [46]	0.16 [46]	0.15 [46]	0.22 [46]
heavy hole	0.40 [100]		0.76 [100]	
exciton	0.0244	0.114	0.125	0.171

Table 6.1: Literature values for the effective masses m^* of electrons and heavy holes in the Γ and the X valley of InAs and AlAs bulk in units of the free electron mass. Effective exciton masses are calculated from the literature values as the reduced masses of the respective electron-hole pairs.

and for RC 1517 by

$$E_{\mathrm{X}}^{\mathrm{low}} = 0.450 \cdot E_{\mathrm{exc}} + 0.886 \quad \Rightarrow \quad a_X^{\mathrm{low}} = 0.450 \pm 0.002, \tag{6.6}$$

$$E_{\mathrm{X}}^{\mathrm{high}} = 0.464 \cdot E_{\mathrm{exc}} + 0.888 \quad \Rightarrow \quad a_X^{\mathrm{high}} = 0.464 \pm 0.007. \tag{6.7}$$

Now it will be demonstrated that the slope a_X of the indirect exciton lines, given by the ratio of the effective masses m_Γ^* and m_X^*, can be connected with the indium fraction x of the samples. The effective masses of electrons, holes and excitons depend on the material in which they are located. The respective masses in the Γ and X valleys of InAs and AlAs (bulk) are given in Tab. 6.1. The values for the exciton masses are the reduced masses of electrons and holes. Moreover, in the compound semiconductor (In,Al)As, the effective exciton mass depends on the indium concentration x of the QDs:

$$m^*_{(\mathrm{In,Al})\mathrm{As}} = x \cdot m^*_{\mathrm{InAs}} + (1-x) \cdot m^*_{\mathrm{AlAs}}. \tag{6.8}$$

With Eq. (6.8) and the effective masses of the excitons from Tab. 6.1, the ratio of the effective Γ- and X-exciton masses in an (In,Al)As QD can be expressed by:

$$\frac{m_\Gamma^*}{m_{\mathrm{X}}^*} = \frac{x \cdot 0.0244 + (1-x) \cdot 0.125}{x \cdot 0.114 + (1-x) \cdot 0.171} = a_X. \tag{6.9}$$

With this expression it is possible to deduce the indium concentration x from the slope of the indirect PL line and reverse. As the indium concentrations are known from the growth conditions of the samples (see Sec. 4.2.1), it is possible to test the accuracy of the model. For this purpose, Eq. (6.9) is plotted in Fig. 6.5 (b) as dashed line together with the actual values for the two samples (colored symbols). It turns out that the model function reproduces the slopes of the X_{low} lines (blue) for both samples. However, the slopes of the X_{high} lines (green) can not be described by Eq. (6.9).

The reason for the mismatch between the calculated and the actual slope of the X_{high} line is routed in the linearity of the model and the existence of two indirect PL lines with different slopes. It is possible that a more advanced model, taking into account strain, deformation potentials, and the nonparabolicity of the electron dispersion, would deliver two different slopes for the same indium concentration. However, from the good agreement between the measured and the calculated slope for the X_{low} line it can be

assumed that the indium concentration is the parameter that mainly determines the slope of the PL lines. Therefore, it is justified to think the model a little bit further. As described in Sec 4.2.1, the indium concentration is not uniform in the QD volume. The maximum concentration is assumed to be centered at bottom of the dot. Therefore, the spatial expansion of the wave function defines the average indium concentration the exciton feels. Thus, another interpretation of the results in Fig. 6.5 (b) could be that the X_{high} excitons experience a lower indium concentration than the nominal value, of about $x = 0.62$, due to a different expansion of the wave function.

6.1.5 Conclusion

In this section, the PL features of the (In,Al)As/AlAs QD ensemble, which occur under selective excitation, are investigated in dependence of excitation energy and temperature. The two samples, AG 2890 and RC 1517, show similar PL spectra. The D line of the spectrum is identified as acoustic phonon replica of the direct Γ-exciton recombination. Since the zero-phonon line of direct recombination is covered by the laser line, all further measurements regarding the direct transition (Sec. 6.3, Sec. 6.4.1) are carried out on this line. For sample RC 1517, the ΓX-transition energies are determined to $E_{\Gamma X}^{\text{low}} = 1.611$ eV and $E_{\Gamma X}^{\text{high}} = 1.657$ eV. In temperature series with AG 2890, the thermal redistribution of electrons from the Γ to the X valleys is observed. Moreover, it was found that the two indirect PL lines X_{low} and X_{high} show different temperature dependencies. For excitation energies above 1.8 eV the unidentified PL features S_{low}, S_{high} and NR start to dominate the spectrum. The static S_{low} line shows the same temperature dependence as the X_{low} line.
Finally, the slope of the indirect exciton energy $E_X(E_{\text{exc}})$ is modeled by a particle in a box theory, which takes the indium concentration of the dots into account. For the lower energetic exciton X_{low}, the model is in good agreement with the sample properties, while this is not the case for the X_{high} excitons. The mismatch might be explained by the uneven distribution of the indium concentration in the QDs or by the simplicity of the model.

6.2 Thermal redistribution dynamics

In this section, the PL dynamics of the nonresonantly excited (In,Al)As/AlAs QD ensemble (sample AG 2890) are studied at different sample temperatures between 2.6 and 85 K. The combination of information on PL intensity and recombination time of direct and indirect QDs and their temperature dependence, gives interesting insights into the energy (fine) structure and the dynamics that take place in between. For example, in the previous section (6.1.3) the temperature dependence of the D-line intensity is explained by the thermal redistribution of the electrons from the X to the Γ valley. Since the two corresponding exciton states are characterized by strongly different recombination times [39], [29] - fast recombination in large, direct dots and slow recombination in small, indirect dots - the redistribution should also influence the PL dynamics.
A tool for the investigation of the PL dynamics is the distribution of recombination times. It is shown in Ref. [28] that the recombination of indirect excitons is mediated by electron scattering at the QD interface, which leads to nonexponential decay curves. In contrast to the exponential decay, which is described by a single recombination time, these curves

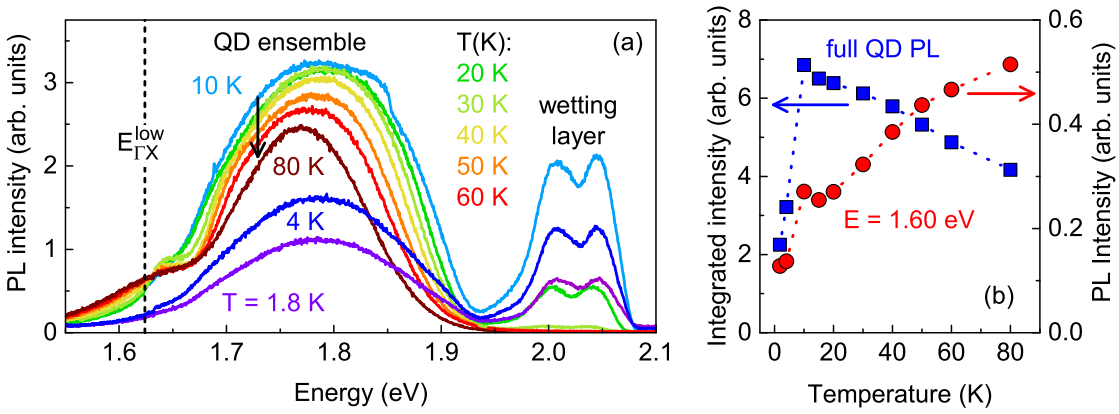

Figure 6.6: **(a)** PL spectra of the (In,Al)As/AlAs QD ensemble (sample AG 2890) under nonresonant excitation for different temperatures. The dashed line marks the ΓX-transition energy $E_{\Gamma X}^{\text{low}} = 1.624$ eV. **(b)** Integrated PL intensity of the full QD emission (dark blue squares) and PL intensity at $E = 1.60$ eV (red dots) in dependence of the sample temperature. Dotted lines are guides for the eye.

are determined by a broad distribution of recombination times. A description of these 'distribution' functions is given in Sec. 2.3.
For the analysis of the experimental findings, two complementary phenomenological models of the level structure and the associated thermal redistribution are introduced. Description and analysis of the experimental results are strictly divided into two subsections for two reasons. On the one hand, the interplay of several experimental results must be taken into account to check the consistency of the models. On the other hand, due to the complexity of the PL dynamics and the lack of a mathematical model, the interpretation of the results should be understood as a proposal under discussion.

6.2.1 Experimental findings

Before the results of the time-resolved PL spectroscopy are viewed, a temperature series of the QD PL under cw excitation ($E_{\text{exc}} = 3.06$ eV) is presented. Figure 6.6 (a) shows the emission in the energy range of the QD ensemble and the wetting layer. When the temperature is increased from 1.8 to 10 K the integrated PL intensity of the QD ensemble ($1.55 - 1.93$ eV) increases by a factor of 3, see also blue symbols in Fig. 6.6 (b). The further increase of the sample temperature form 10 to 85 K, leads to the linear decrease of the integrated intensity. This decrease is caused by the reduction of the PL intensity in the spectral range between 1.65 and 1.93 eV, which is nearly the whole QD emission range. However, for lower energies, especially for emission energies below $E_{\Gamma X}^{\text{low}} = 1.624$ eV, the situation is completely different. At $E = 1.60$ eV, the increase of the temperature from 10 to 85 K causes the increase of the PL intensity by a factor of about 2, see red symbols in (b). For $T > 85$ K, the PL intensity seems to saturate. At $E = 1.63$ eV, close to $E_{\Gamma X}^{\text{low}}$, the PL intensity remains constant for temperature changes between 10 and 85 K, see (a).
The ratio of the wetting-layer PL and the QD PL remains the same for the temperature increase between 1.8 and 10 K. For higher temperatures, the wetting-layer PL decreases

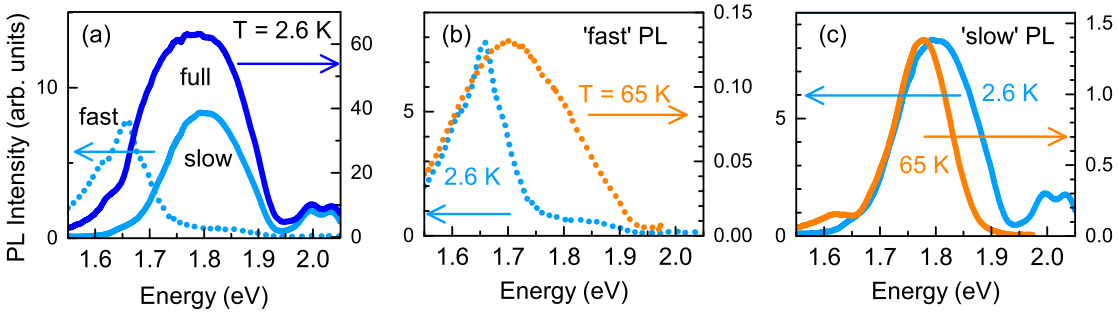

Figure 6.7: Time-resolved PL spectra of the (In,Al)As/AlAs QD ensemble. **(a)** 'Fast' PL (blue, dotted line), measured with $t_{\mathrm{delay}} = 20$ ns and $t_{\mathrm{gate}} = 10$ ns, 'slow' PL (blue, solid line), measured with $t_{\mathrm{delay}} = 500$ ns and $t_{\mathrm{gate}} = 34500$ ns, and the fully time-integrated PL spectrum (dark blue line) measured with $t_{\mathrm{delay}} = 0$ ns and $t_{\mathrm{gate}} = 35000$ ns. $T = 2.6$ K. **(b)** and **(c)** Comparison of the (b) fast and the (c) slow low-temperature spectra (blue) from (a) with the respective PL spectra detected at $T = 65$ K (orange).

much faster and become negligible for $T \geq 30$ K.

Now, the results of the time-resolved PL spectroscopy are presented. The excitation energy is $E_{\mathrm{exc}} = 3.49$ eV and the pulse frequency is 2 kHz. The experimental method is described in Sec. 3.3. As a first step, the PL is collected in two different time windows. The first one starts shortly after the laser pulse and has gate width of 10 ns, the second one starts 500 ns after the laser pulse and has a width of 35000 ns. Figure 6.7 (a) shows the results for $T = 2.6$ K. The blue, dashed PL spectrum was detected within $t_{\mathrm{gate}} = 10$ ns after a delay of $t_{\mathrm{delay}} = 25$ ns with respect to the laser pulse. Here the PL maximum is at 1.649 eV and the FWHM is about 109 meV. Between $t = 50$ ns and 60 ns the PL maximum shifts strongly to higher energies (not shown here). In the final stage the intensity maximum is located at 1.801 eV as shown by the blue, solid spectrum which was detected within $t_{\mathrm{gate}} = 34500$ ns after $t_{\mathrm{delay}} = 500$ ns. Here the FWHM is 130 meV and the shape of the curve is similar to the fully time-integrated PL spectrum (dark blue line). For simplification, the PL spectra in Fig. 6.7 are labeled with 'fast' and 'slow' PL. In the following, these terms are used to distinguish between PL emitted before and after $t = 55$ ns.

Next, the spectra presented in (a) are compared with the results for higher temperatures. Figure 6.7 (b) shows the 'fast' PL for $T = 2.6$ K (blue) and $T = 65$ K (orange). Although both PL spectra were measured in the same time window ($t_{\mathrm{delay}} = 20$ ns and $t_{\mathrm{gate}} = 10$ ns) the shapes are clearly different. With the increase of temperature the PL maximum shifts from 1.649 to 1.706 eV and the FWHM almost doubles from 108 to 209 meV. Compared to $T = 2.6$ K, the spectral range of the 'fast' emission is significantly increased for $T = 65$ K as the high energy shoulder is shifted from 1.75 to 1.90 eV. Thus, 'fast' PL can be measured between 1.55 and 1.9 eV. Moreover, the spectral integrated PL intensity decreases by a factor of about 33 for $T = 65$ K.

The development of the 'slow' PL spectrum is shown in Fig. 6.7 (c) for $T = 2.6$ K and 65 K. The spectra were recorded with $t_{\mathrm{delay}} = 500$ ns and $t_{\mathrm{gate}} = 34500$ ns each. Apart from the decrease of the integral intensity, the shapes of the spectra differ clearly from each other. Between 1.8 eV and 1.95 eV there is a decrease of the PL intensity when the

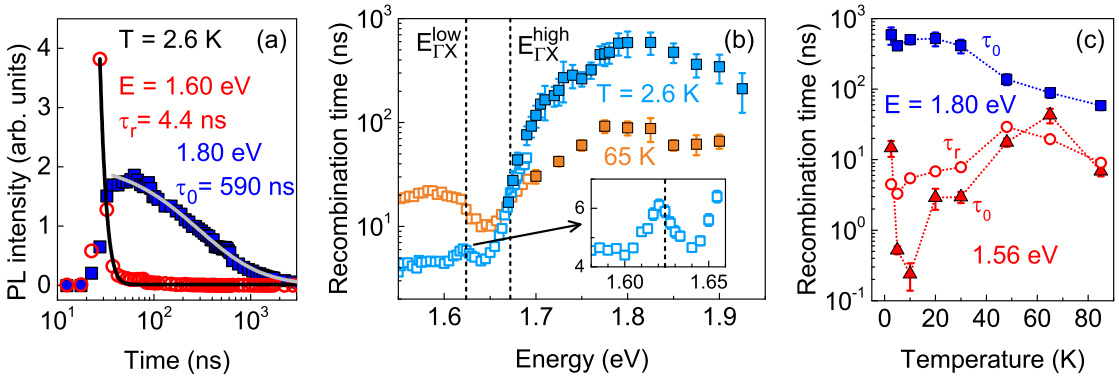

Figure 6.8: **(a)** PL decay curves of direct QD excitons, with $E = 1.60$ eV (red circles), and indirect QD excitons with $E = 1.80$ eV (dark blue squares). The lines show the results of fitting the exponential (black) and the distribution function (grey) to the data sets. **(b)** Fit parameters τ_r (open symbols), of the exponential function, and τ_0 (filled symbols) of the distribution function for $T = 2.6$ K (blue) and 65 K (orange). The dashed lines show the ΓX-transition energies. The inset shows the recombination times around $E_{\Gamma X}^{\text{low}}$. **(c)** Recombination time τ_r (open symbols) and τ_0 (filled symbols) in dependence of the temperature for direct and indirect excitons with emission energies of $E = 1.60$ eV (red) and 1.80 eV (dark blue).

temperature is changed from 2.6 K to 65 K. Between 1.55 eV and 1.65 eV the opposite effect, although much lower, is observed. Here, a slight increase of the PL intensity is found at the higher temperature.

In order to determine the recombination times for different QD sizes (emission energies) and temperatures, time-integrated measurements were performed for different delay times between 0 and 80000 ns. In order to obtain a reasonable temporal resolution, the gate widths t_{gate} are chosen so that Δt is usually smaller than $0.25t$ (see Sec. 3.3). Two examples of the resulting decay curves with very different time dependencies are presented in Fig. 6.8 (a) for $T = 2.6$ K. The emission energies are 1.60 eV (red circles) and 1.80 eV (dark blue squares). To determine the characteristic decay time, the decay curves were fitted with either an exponential function

$$I(t) = A \cdot \exp(-t/\tau_r),$$

or the distribution function Eq. (2.12) with the fit parameters τ_0 and γ, which is introduced in Sec. 2.3. τ_r and τ_0 characterize the recombination time of the decay. The best results were achieved by fitting the exponential function to decay curves emitted at low energies (1.55 - 1.67 eV) and the distribution function to decay curves emitted at high energies (1.67 - 1.925 eV). The quality of the fit was determined by the errors of the fit parameters. As the recombination times vary between three orders of magnitude, parameter sets with an average error below 30% are considered as a reasonable fits.
The fit functions for PL decay at $E = 1.60$ and 1.80 eV are shown in Fig. 6.8 (a) by the colored lines. The exponential fit function (black) is optimized for $\tau_r = (4.4 \pm 0.1)$ ns and the distribution function (grey) for $\tau_0 = (590 \pm 160)$ ns and $\gamma = 2.9 \pm 0.4$. In Fig. 6.8

(b), the full spectral dependence of the fit parameters τ_r (open symbols) and τ_0 (filled symbols) is shown for $T = 2.6$ K and $T = 65$ K. For $T = 2.6$ K (blue), the recombination time is constant at about 4.5 ns between 1.55 and 1.605 eV. Between 1.605 and 1.640 eV it increases up to 6 ns at 1.621 eV (see closeup) and decreases down to 4.5 ns again. The spectral energy of this local maximum agrees well with the ΓX-transition energy $E_{\Gamma X}^{\text{low}}$ at 1.624 eV. For energies above 1.64 eV, the recombination time increases up to the total maximum of 591 ns at 1.825 eV and then decreases down to 212 ns at 1.925 eV. The transition from exponentially shaped decay curves (open symbols) to decay curves fitted by the distribution function (filled symbols) is between 1.66 and 1.67 eV. This energy coincides with the ΓX-transition energy $E_{\Gamma X}^{\text{high}}$ at 1.67 eV. The comparison with the results for $T = 65$ K (orange symbols) shows that the recombination time rises with increasing temperature for energies below $E_{\Gamma X}^{\text{high}}$ and decreases for energies above this value. In addition, the local maximum at $E_{\Gamma X}^{\text{low}}$ is transformed to an inflection point with a higher recombination time on the low energy side.
The temperature dependence of the recombination time, measured at the spectral points $E = 1.56$ eV (red) and 1.80 eV (dark blue), is presented in Fig. 6.8 (d). Although the exponential parameter τ_r (open red circles) describes the recombination time at $E = 1.56$ eV with a much higher accuracy, the fit parameters τ_0 of the distribution function (filled red triangles) are added to the plot for completeness. At $E = 1.56$ eV, the results for τ_r and τ_0 differ strongly, especially for for temperatures around 10 K but the general trend is the same. However, the following description refers to the τ_r (open red circles) for $E = 1.56$ eV and τ_0 (filled dark blue squares) for $E = 1.80$ eV only. For temperatures between 2.6 and 48 K, the recombination times for $E = 1.56$ eV and 1.80 eV show opposite temperature dependencies. At $E = 1.56$ eV, τ_r increases from 4.4 to 29 ns and at $E = 1.80$ eV, while τ_0 decreases from 590 to 140 ns. Only exception is the temperature range around 5 K. Here both curves have a local minimum. Above 48 K both curves seem to follow the same negative slope. However, the slope of the high energy curve (dark blue squares) is nearly 5 times bigger than for the low energy curve (red circles) in that temperature range. Thus, the difference between the exciton recombination times, measured at $E = 1.56$ eV and 1.80 eV, becomes smaller with increasing temperature.

The fit parameter γ of the distribution function is presented in Fig. 6.9 (a) and (b) in dependence of the emission energy and the temperature. A strong spectral dependence of γ is observed in (a) for $T = 2.6$ K (blue squares) and $T = 65$ K (orange squares), where it decreases from 5.0 or 3.7 to 2.2. The higher values are found for exciton recombination in direct QDs with $E < E_{\Gamma X}^{\text{low}}$, while the lower value is reached exactly at the transition energy between direct and indirect QDs. The dark blue and the red lines show Boltzmann functions fitted to the data points in this energy range with the central points at (1.606 ± 0.002) eV for $T = 2.6$ K and at (1.592 ± 0.005) eV for $T = 65$ K.
For $T = 5$ K (green squares), γ remains constant at about 1.9 in this energy range. For higher energies, γ is more or less independent from the temperature and increases slightly up to about 2.7 at $E = 1.80$ eV. This independence is reflected in the constant slope of the blue squares in (b), which show γ at the emission energy of 1.70 eV as a function of the temperature. In contrast, γ shows a strong temperature dependence for the emission energy $E = 1.56$ eV (red squares) with the highest values at $T = 2.6$ K and a local maximum at $T = 65$ K.

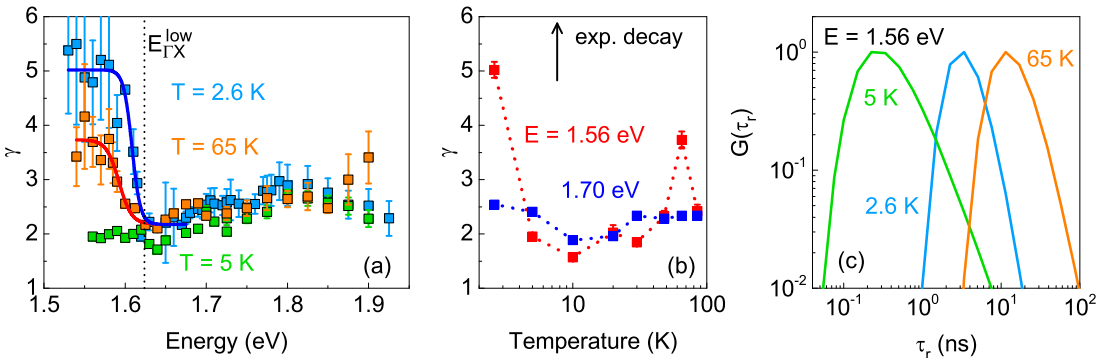

Figure 6.9: **(a)** Fit parameter γ of the distribution function Eq. (2.12) in dependence of the emission energy, measured at different temperatures. The dashed line shows the ΓX-transition energy $E_{\Gamma X}^{\text{low}} = 1.624$ eV. **(b)** Fit parameter γ for direct (red) and indirect QDs (dark blue) in dependence of the temperature. Dotted lines are guides for the eye. **(c)** Distribution $G(\tau_\text{r})$ of the recombination times, according to Eq. (2.13), in direct QDs ($E = 1.56$ eV) at different temperatures.

According to Eq. (2.13), it is now possible to calculate the distribution of recombination times $G(\tau_\text{r})$ for certain cases from the two fit parameters τ_0 (from Fig. 6.8 (c)) and γ. Figure 6.9 (c) shows $G(\tau_\text{r})$ for the direct QDs with an emission energy of 1.56 eV. Surprisingly, the broadest distribution and the lowest average recombination time are found for $T = 5$ K (green line), while the narrowest distribution is given for the lowest temperature $T = 2.6$ K (blue line). The highest average recombination time, under these three selected temperatures, is measured for $T = 65$ K (orange line).

To complete this section, the main experimental results, which were gained under non-resonant excitation of the (In,Al)As/AlAs QD ensemble, are summarized. The following effects occur due to the increase of the temperature

from 2 K to 5 K /10 K:

1) The integrated intensity increases by a factor of 3. (For indirect QDs, the increase starts at lower temperatures than for direct QDs.)
2) The recombination is accelerated.
3) The distribution of recombination times in direct QDs becomes broader.

and above 10 K:

4) The PL intensity emitted by direct QDs increases by a factor of 2, while the PL intensity from indirect QDs decreases.
5) The recombination time of direct QDs increases (for $T < 60$ K), while the recombination time of indirect QDs decreases. For $T > 60$ K, the recombination time decreases for both kinds of dots.
6) For $T = 65$ K, the distribution of recombination times in direct QDs is narrowed.

6.2.2 Discussion and redistribution models

The analysis of the experimental results presented in the previous section will be divided into three parts: First, the strong spectral dependence of the recombination time and its distribution for $T \approx 2$ K are discussed. Then, the temperature dependence of these quantities is examined, where a distinction is made between the low temperature effects, which occur between 2 and 10 K, and the high-temperature effects, which occur above 10 K. Two different models are considered as explanations for the experimental findings: It is assumed that in the lower temperature range, the PL dynamics is governed by the thermal redistribution of excitons from the dark to the bright Γ-exciton state, while at higher temperatures, the redistribution of electrons between the Γ and the X valley determines the dynamics. These models are checked on the basis of the experimental results.
The discussion of the wetting layer is largely dispensed here, as its interaction with the QDs is weak [27].

Dynamics of direct and indirect excitons

The strong increase of the recombination time at the ΓX-transition energy for $T = 2.6$ K, presented by the blue symbols in Fig. 6.8 (b), is already described in Ref. [39] and [29]. These results are briefly recalled here. For indirect excitons, with the electron in the X valley of the conduction band and the heavy hole in the Γ valley of the valence band, the direct optical recombination is forbidden due to the mismatch in momentum space. The required change of momentum is caused by the scattering of the electron at the QD interface [28]. This condition prolongs the recombination time. In the studied (In,Al)As/AlAs QD ensemble, larger dots with smaller emission energy are direct QDs, while smaller dots with higher emission energy are indirect, see Sec. 4.2.2. For a specific size, which is related to the ΓX-transition energy $E_{\Gamma X}$, the band gap of the dots is changed from direct to indirect. Thus, the recombination time increases for $E > E_{\Gamma X}$.
A new feature is the maximum of τ_r at the ΓX-transition energy $E_{\Gamma X}^{\mathrm{low}}$, which is presented in the inset of Fig. 6.8 (b). The maximum can be explained by the mixing of the short-living Γ state with the long-living X state. However, more remarkable than the increase of τ_r is the decrease of the recombination time between $E_{\Gamma X}^{\mathrm{low}}$ and $E_{\Gamma X}^{\mathrm{high}}$. This behavior can be explained by the sustained, dominant recombination of Γ excitons caused by electrons that do not relax to the X level. The reason for the low energy relaxation rate is routed in the small energy gap $\Delta E_{\Gamma X}$ between the Γ and the X valley in this energy range. It is assumed that the relaxation, which is mediated by phonon scattering, is accelerated when $\Delta E_{\Gamma X}$ is larger than the phonon energy of at least one phonon type in the QDs. The energy of the $\mathrm{TA_{AlAs}}$ phonons is 12 meV [82]. According to Eq. (6.4), it is $\Delta E_{\Gamma X} = 12$ meV when the energy of the Γ level is $E_\Gamma = 1.645$ eV. For higher energies (smaller dots), the relaxation to the X valley is assisted by the $\mathrm{TA_{AlAs}}$ phonons. In the inset of Fig. 6.8 (b) it can be seen that the recombination time starts to increase again exactly at this energy. Further consequences of the slow relaxation from the Γ to the X valley in this energy range are also discussed in Sec. 6.3 in connection with the optical alignment and the optical orientation of direct excitons and in Sec. 6.5.4 in connection with the hyperfine interaction.
The parameter γ, which reflects the width of the recombination time distribution, changes

strongly at the ΓX-transition energy, see blue symbols in Fig. 6.9 (a). According to Eqs. (2.12) and (2.13), a high value of γ is connected with an exponential-like decay, while a low γ describes a nonexponential decay function with a broad distribution of recombination times. Thus, the observed decrease of γ is connected with the broadening of the distribution $G(\tau_\mathrm{r})$. In Ref. [28], where γ is determined to 2.30 - 3.45 for indirect QD excitons in similar samples, the nonexponential decay of indirect excitons is explained by the electron scattering at the QD interface, which provides the change of momentum and leads to the recombination. In contrast, the recombination of direct excitons of the (In,Al)As/AlAs QD ensemble is well described by exponential functions, see Sec. 6.4.2. It can thus be stated that the width of the recombination time distribution is an additional tool to distinguish between direct and indirect excitons, at least at low temperatures ($T \leq 2.6$ K).

$T < 10$ K: Redistribution between dark and bright states

The discussion of the temperature dependence is started with the recall of the fine structure of direct excitons, which is introduced in Sec. 2.1.2. The electron-hole exchange interaction splits the dark and bright exciton levels by an energy of δ_0, which is in the range of several hundreds of μeV [18]. In case of indirect excitons, the electron-hole exchange interaction is suppressed [30]. Therefore, δ_0 becomes zero or is at least strongly reduced. Anyway, for excitons in the dark ground states, the radiative recombination is forbidden. A scheme of the dark and bright Γ and X levels of the QD ensemble is presented in Fig. 6.10. The splitting between the dark and bright X exciton levels, X_d and X_b, is only for better visibility. When the QD sample is excited nonresonantly, excitons are created in the AlAs barrier (B). The QDs act as potential traps, where the carriers get captured. The associated energy relaxation (dashed green arrows) is accompanied by the loss of spin polarization. Thus, the bright and dark Γ-exciton states, Γ_b (red) and Γ_d (grey), are equally populated.
First, the redistribution in direct QDs with $E_\Gamma < E_X$ and $\delta_0 > 0$ is considered, see left side of Fig. 6.10. For the direct QDs, it is demonstrated in Sec. 6.3 that the spin relaxation time is comparable to the recombination time. Therefore, excitons in the bright Γ level can either recombine (red arrow) or, with the about the same probability, relax to the dark Γ level (green arrow). At very low temperatures ($k_\mathrm{B}T \ll \delta_0$), the excitons are frozen in the dark state, where they can recombine only nonradiativly (not shown). Thus, the PL intensity, emitted by the bright state, is low, compare Fig. 6.6 for $E = 1.60$ eV and $T = 1.8$ K.
The increase of the temperature to $k_\mathrm{B}T > \delta_0$ leads to the increase of the spin-flip rate from the dark to the bright level (orange arrow) and to the increase of the PL intensity emitted by the direct QDs. In the experiment, presented in Fig. 6.6 (b), an increase of the PL intensity is found between 5 and 10 K (see red symbols). Thus, if the model is correct, the splitting between the upper dark and the lower bright Γ exciton level can be estimated to 645 μeV and the exchange splitting δ_0, with $\delta_2 > \delta_1$ [18] and $\delta_1 \approx 300$ μeV (Sec. 6.4), to $\delta_0 > 945$ μeV. In Ref. [31] it was found for the indirect type-II GaAs/AlAs QW, that the nonradiative recombination is much slower than the radiative recombination and in Sec. 5.1 it is demonstrated that this is also true for the indirect type-I InAs/AlAs QW. Here, it is assumed that this relation can also be applied for the direct type-I (In,Al)As/AlAs QDs. In this case, the redistribution from the dark to the

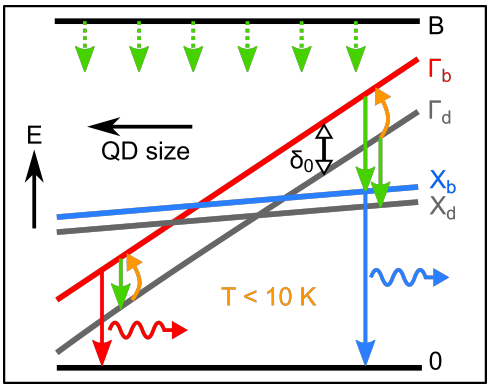

Figure 6.10: Schematic representation of the low-temperature model describing the thermal redistribution (orange arrows) between the dark and bright Γ-exciton states in the (In,Al)As/AlAs QD ensemble under nonresonant excitation. Dark and bright Γ states, Γ_d (grey) and Γ_b (red), are split by the exchange energy δ_0. Here, the splitting between dark and bright X states, X_d (grey) and X_b (red), is only for better visibility. The dashed green arrows indicate the relaxation from the AlAs barrier (B), solid green arrows show the relaxation between QD levels. Recombination and PL emission of direct and indirect excitons is indicated by the red and blue arrows.

bright exciton level causes the acceleration of the recombination, since a higher amount of excitons can now recombine radiatively. The decrease of the recombination time is documented in Fig. 6.8 (c) by the red symbols. At the same time, the broadening of the recombination time distribution is observed for direct excitons, see red symbols in Fig. 6.9 (b). This behavior might be explained by excitons that alternate between the bright and dark states several times before the recombination.
In case of indirect QDs, with $E_\Gamma > E_X$ (right side of Fig. 6.10), the excitons relax from the Γ to the X state. As mentioned above, the relaxation is accelerated for a sufficiently high ΓX splitting ($\Delta E > E_{\mathrm{Phonon}}$). When this process becomes faster than the direct recombination, and thus faster than the spin relaxation (see Sec. 6.6.2), the excitons from the bright Γ level relax to the bright X level and excitons from the dark Γ level relax to the dark X level (green arrows). Due to the long spin-flip or spin-relaxation time of X exciton in comparison to its recombination time, excitons in the dark X level are trapped and do not contribute to the radiative emission. The same effect should prevent the relaxation of the bright X excitons to the dark states. The increase of the temperature leads to the thermal activation of excitons from the dark to the bright Γ state (orange arrow), which causes a strong increase of the indirect exciton emission (blue arrow). This effect is observed experimentally as shown by the increase of the integrated intensity (blue symbols) in Fig. 6.6 (b). As described above for the direct QDs, the increased number of bright excitons leads to the acceleration of the recombination, which can be seen in Fig. 6.8 (c) by the dark blue symbols for $T > 10$ K.
It is assumed that the simultaneous increase of the wetting-layer PL with the QD PL at low temperatures, demonstrated in Fig. 6.6 (a), is caused by the thermal redistribution of excitons from dark to bright wetting-layer states, while its fast decrease at higher temperatures is explained by the exciton transfer to nonradiative centers [27].

$T > 10$ K: Redistribution between direct and indirect states

Now the effects at higher temperatures are discussed. Figure 6.11 illustrates the possible redistribution processes between the Γ and X exciton levels as well as the thermal excitation to the AlAs barrier (B).
In case of direct QDs, the Γ level is the exciton ground state, see left side of (b). For $T = 2.6$ K, the respective exciton recombination time is determined to 4.5 ns, see blue symbols in Fig. 6.8 (b). The recombination is indicated by the red arrows. With increasing temperature, the transition rate of the electron to the X valley rises (orange arrow). The transition rate to the higher energy level is proportional to the Boltzmann factor which depends on the size of the energy gap and the temperature. In the X state the recombination time is several hundred nanoseconds, see blue symbols in Fig. 6.8 (b), while the energy relaxation time is significantly shorter. Otherwise, it would be possible to find X lines above the laser line in the PL spectra of direct QDs, which is not the case. Thus, all excitons in the X state relax back to the Γ state (green arrow). However, if the relaxation time is in the order of a few nanoseconds, it can be assumed that the detour to the X state prolongs the overall exciton recombination time in direct QDs. Indeed, in Fig. 6.7 (c) it is shown that the 'slow' PL intensity is slightly increased for $T = 65$ K in the energy range around 1.60 eV. Moreover, Figs. 6.8 (c) and (d) show that the recombination time in direct QDs, with $E < E_{\Gamma\mathrm{X}}^{\mathrm{low}} = 1.624$ eV, increases with increasing temperature.
Another argument for the thermal excitation of excitons from the Γ to the X state in direct QDs is the energy shift of the transition from high to low γ values when the temperature is increased from 2.6 K to 65 K, see Fig. 6.9 (a). As it is pointed out on page 67, high γ values indicate a direct and low γ values an indirect recombination. The transition energies are determined to $E = 1.606$ eV for 2.6 K and $E = 1.592$ eV for 65 K. The difference of the ΓX splittings $\Delta E_{\Gamma X}$ at these two energies can be calculated via Eq. (6.4) to 8.12 meV, which is in good agreement with the difference of the thermal energies $\frac{3}{2}k_{\mathrm{B}}(65 - 2.6\ \mathrm{K}) = 8.05$ meV. These results imply that by increasing the temperature, the additional thermal energy lifts the excitons of larger and larger QDs to the higher X state.

In case of indirect QDs (right side of Fig. 6.11), the Γ excitons can either relax to the X states (green arrow) or recombine (red arrow). The dominating process is determined by the size of the ΓX splitting $\Delta E_{\Gamma X}$, as explained above (p. 66). However, in the X state the recombination time is in the order of several hundred nanoseconds for $T = 2.6$ K. In contrast to direct QDs (left side of (b)), the long recombination time in indirect QDs increases the probability that the exciton will be thermally exited to the higher level, here Γ state, during its lifetime. This process, indicated by the orange arrow, leads to the increase of the PL emission from the direct level (red arrow) and to the decrease of emission from the indirect state (blue arrow). This effect is observed and discussed in context of selective excitation of indirect QDs, see Figs. 6.4 (b) - (e) in Sec. 6.1.3. Moreover, this effect should reduce the recombination time in the spectral region of the indirect QDs, which is confirmed in the experiment by the decrease of τ_{r} (dark blue symbols) in Fig. 6.8 (c).

For the smallest QDs in the ensemble, the energy of the Γ level approaches the AlAs

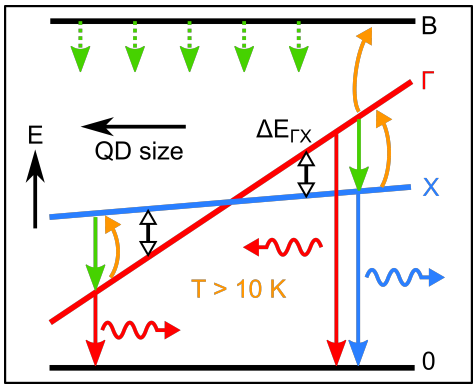

Figure 6.11: Schematic representation of the high-temperature model for $T > 10$ K describing the thermal redistribution (orange arrows) between direct and indirect exciton states in the (In,Al)As/AlAs QD ensemble under nonresonant excitation. The dashed green arrows indicate the relaxation from the AlAs barrier (B). In direct QDs with $E_\Gamma < E_X$, thermal activation occurs from the Γ (red line) to the X state (blue line), while in indirect QDs with $E_\Gamma > E_X$, excitons are activated from the X to the Γ state and from the Γ state to the barrier. Relaxation between QD states is indicated by solid green arrows, direct and indirect recombination by red and blue arrows. $\Delta E_{\Gamma X}$ is the energy splitting between the Γ and the X state.

barrier. Thus, the band-gap energy of the barrier, which is given by 2.30 eV, determines the maximum energies of the two indirect exciton levels, as these levels can be excited only by energy relaxation from the Γ valley. For sample AG 2890, they can be calculated via the equations (6.4) and (6.5) to $E_{\text{max}}^{\text{low}} = 1.91$ eV and $E_{\text{max}}^{\text{high}} = 1.96$ eV. $E_{\text{max}}^{\text{high}}$ is in good agreement with the intensity minimum between the QD PL and wetting layer, shown in Fig. 6.6 (a). It is easy to see that the rise of the temperature enhances the escape of excitons from the QDs into barrier (upper orange arrow in Fig. 6.11). The excitons quickly relax back to unpopulated QDs (dashed green arrows). As the recombination time in direct QDs is lower than in indirect QDs for all temperatures up to 85 K, see Fig. 6.8 (c), the additional excitons from the barrier most likely populate direct QDs. This exciton redistribution from the smallest indirect dots to the direct QDs is reflected in the temperature dependence of the PL spectrum, see Fig. 6.6 (a). Here, the intensity of the direct QDs increases (see also red symbols in (b)), while the integrated intensity decreases. Note that this increase of direct PL emission is not in conflict with the decrease of the emission of direct QDs, which is demonstrated in Fig. 6.4 (a), since there is no thermal excitation to the barrier under selective excitation. In addition, it can be seen in Fig. 6.6 (a) that with increasing temperature the higher energy flank of the QD PL decreases the fastest, due to excitons escaping to the barrier. The effect is also visible in Fig. 6.7 (c), where at 65 K the relative intensity of the 'slow' PL is strongly reduced for energies above 1.8 eV in comparison to 2.6 K.

Further effects

Finally, some effects that can not be explained by the two models should be mentioned and discussed. The decrease of the integrated PL intensity with increasing temperature,

demonstrated in Fig. 6.6 (b) by the dark blue symbols, is attributed to nonradiative losses. Moreover, the decrease of the direct (and indirect) recombination time above 65 K in Fig. 6.8 (c) can be explained by this process. At low temperatures around 5 K, the decrease of the recombination time, which is explained by the thermal redistribution from the dark to the bright Γ level, is followed by the increase of the recombination time with increasing temperature. In case of direct QDs this increase can be explained in terms of the thermal redistribution between direct and indirect states, which is discussed above. However, in case of indirect QDs (dark blue symbols in Fig. 6.8 (c)), this effect is unexpected. It might be due to the acceleration of the relaxation time from the Γ to the X level with rising temperature, which leads to the increase of indirect recombination processes. This assumption is based on the consideration that the relaxation from Γ to the X level is mediated by phonon scattering, which should increase with increasing temperature. The reason for the narrowing of the distribution $G(\tau_\mathrm{r})$ (increase of γ) for direct QDs at 65 K in Fig. 6.9 (b) is not understood so far.

6.2.3 Conclusion

The temperature depended study of the PL dynamics under nonresonant excitation of the whole (In,Al)As/AlAs QD ensemble turns out to be highly complex. As the experimental findings indicate two different temperature ranges with different effects, they are compared with two thermal redistribution models. For $T < 10$ K, a strong increase of the PL intensity and an acceleration of the PL dynamics are found. Moreover the distribution of recombination times broadens. These results are explained by the thermal activation of Γ excitons from the dark to the bright states. The exchange splitting is estimated to $\delta_0 > 945$ μeV. For $T > 10$ K, the PL intensity of the direct QDs increases, while the integral intensity of the QD emission decreases. This effect is attributed to the escape of excitons from the smallest QDs to the AlAs barrier and the related redistribution to direct QDs. Furthermore, the recombination times, measured for the excitons in direct and indirect QDs, show opposite temperature dependencies above 10 K. It is assumed that in case of direct QDs, the exciton lifetime is prolonged by thermal transitions the X state. In case of indirect QDs, the recombination time is decreased, since the excitons are thermally excited from the X to the Γ state from where they quickly recombine.
It should be emphasized that although the comparison of experimental findings and the thermal redistribution models are qualitatively in good agreement, mathematical models are required to prove their quantitative accuracy.

6.3 Optical orientation and alignment

In this section, the fine structures of direct and indirect excitons in the (In,Al)As/AlAs QD ensemble are investigated. The fine structure is a fundamental property of the exciton, as it defines the spin states of the energy levels and their splitting. It is known for direct QD excitons that the pure spin states are mixed and split by the anisotropic exchange interaction into two linearly polarized states $|X\rangle$ and $|Y\rangle$, see Sec. 2.1.2. If, in this case, the spin relaxation time τ_s is not significantly shorter than the exciton recombination time τ_r, the effect of optical alignment is observed. For indirect excitons, it is theoretically predicted that the electron-hole exchange interaction is suppressed [30]. Thus, the exciton spin states are expected to be degenerated and exist in their

pure, unmixed forms, $|+1\rangle$ and $|-1\rangle$, as it is shown in Fig. 2.1 for $E_{\mathrm{exch}} = 0$. In this case, optical orientation should be measurable for the indirect QDs.
The optical addressing of direct and indirect QDs with a specific exciton energy (QD size) by selective excitation is discussed in Sec. 4.2.2 and 6.1. The techniques to measure optical alignment and optical orientation are explained in Sec. 3.2.2. Here, optical alignment and optical orientation are measured for direct and indirect QDs in sample AG 2890 by tuning the laser energy through the energy range of the QD ensemble. The polarization of the laser light is either circularly or linearly polarized. Since there is no external magnetic field, except for the earth magnetic field, which can be neglected, the optical orientation degree ρ_{oo} is equal to the circular polarization degree ρ_{c}^{+}. ρ_{c}^{+} is determined by the circularly polarized intensity components of the PL I_{+}^{+} and I_{-}^{+}. The degree of optical alignment is determined analogously via the linearly polarized components I_{0}^{0} and I_{90}^{0}.

6.3.1 Fine structure of direct and indirect excitons

As a first attempt, two different excitation energies, $E_{\mathrm{exc}} = 1.61$ eV and $E_{\mathrm{exc}} = 1.70$ eV, are chosen to compare the polarization properties in direct and indirect QDs. The results in Fig. 6.12 show that direct and indirect excitons behave contrariwise with regard to optical alignment and optical orientation. In case of the direct QDs (red lines), the D line in (a) shows an optical alignment degree of 53%, while the optical orientation degree of 1% in (b) can be neglected. In case of indirect QDs (green lines), an optical alignment degree of 4% and an optical orientation degree of 37% are found for the X_{high} line, see Figs. 6.12 (c) and (d). The D line, which is of low intensity for indirect QDs, shows an optical orientation degree of 73%, while the linear polarization degree could not be determined in this case.

The results for the direct QDs confirm the considerations about the exciton fine structure. In Sec. 2.1.2 it is explained that for direct excitons the spin states are split by the isotropic exchange interaction into bright $|\pm1\rangle$ and the dark $|\pm2\rangle$ states. The twofold degeneration of the bright states is lifted by the anisotropic exchange interaction, which is nonzero for real, unsymmetrical QDs. The loss of the axial symmetry also leads to the mixing of the two bright states. The resulting states are given by the linear polarized, dipole active [101] states $|\mathrm{X}\rangle = \frac{1}{\sqrt{2}}(|+1\rangle + |-1\rangle)$ and $|\mathrm{Y}\rangle = \frac{1}{i\sqrt{2}}(|+1\rangle - |-1\rangle)$ with an energy splitting of δ_1, the anisotropic exchange splitting [18], [102].
When the direct QDs are excited with linearly polarized light under steady-state conditions, as presented in Fig. 6.12 (a), the linear polarization degree of the emitted light depends on the ratio between the spin relaxation time τ_{s} and the exciton recombination time τ_{r}, see Eq. (2.7). If the τ_{s} is not much smaller than τ_{r}, the optically induced spin polarization remains for some excitons during their lifetime and the polarization of the emitted light is nonzero. In case of linearly polarized excitation, the occurrence of $\rho_{\mathrm{l}} > 0$ is called optical alignment. As the linear polarization degree of the D line is 53%, it can be concluded that the spin relaxation time of the Γ exciton is comparable to its recombination time, which is several nanoseconds (see Fig. 6.8 (c)).
The circularly polarized excitation of a direct QD, as presented in Fig. 6.12 (b), leads to the creation of an exciton in the superposition state of $|\mathrm{X}\rangle$ and $|\mathrm{Y}\rangle$. The coherence of these two states gets lost within the decoherence time τ_{d} [103], which is given by the

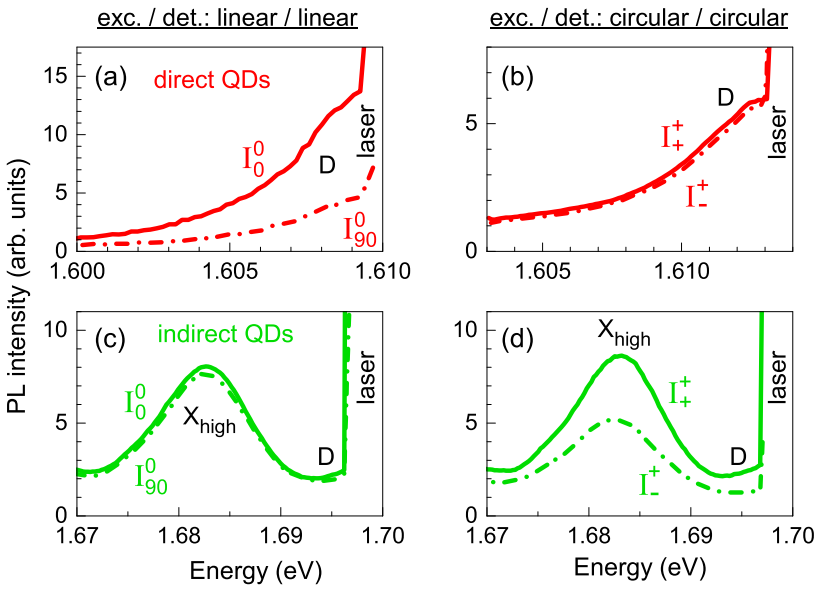

Figure 6.12: Polarized PL spectra under selective, polarized excitation of direct (red) and indirect QDs (green) of the (In,Al)As/AlAs QD ensemble. $T = 10$ K and $B = 0$ T. I_+^+ and I_-^+ are circularly polarized PL components, I_0^0 and I_{90}^0 are linearly polarized PL components. **(a)** Linearly and **(b)** circularly polarized PL components of the D line with $E_{\mathrm{exc}} = 1.61$ eV. **(c)** Linearly and **(d)** circularly polarized PL components of the X_{high} and the D line with $E_{\mathrm{exc}} = 1.70$ eV.

energy difference between the states [6]. As the two states are split by the anisotropic exchange interaction, it is $\tau_{\mathrm{d}} = h/\delta_1$, where h is the Planck constant. In Sec. 6.4, the splitting δ_1 is determined to about 350 μeV for direct QD excitons. Thus, the decoherence time is estimated to $\tau_{\mathrm{d}} \approx 10$ ps. In case of $\tau_{\mathrm{d}} \ll \tau_{\mathrm{r}}$, the coherence is lost before the recombination of the exciton and the emitted light is unpolarized. With τ_{r} in the range of several ns (see Fig. 6.8 (c)), this condition is fulfilled in direct QDs and the absence of optical orientation is demonstrated in Fig. 6.12 (b).

The situation is different for indirect QDs. The occurrence of optical orientation in (d) means that the bright exciton states are given by $|+1\rangle$ and $|-1\rangle$. This finding can be explained by the indirect band gap in momentum space. As the wave functions of electron and hole hardly overlap in k-space, the electron-hole exchange interaction is weakened for indirect excitons [30]. Therefore, the mixing and splitting of the spin states is suppressed. When the indirect QDs are excited with circular polarized light, only the corresponding spin state gets populated. The relatively high optical orientation degree of 37% indicates that the spin relaxation time τ_{s} is not significantly shorter than the exciton recombination time τ_{r}. In Sec. 6.5 it is found that for $B = 0$ mT the optical orientation degree is strongly suppressed by the hyperfine interaction and that τ_{s} can become much longer than τ_{r} in an external longitudinal magnetic field. This is also confirmed by time-resolved measurements in Sec. 6.6.
Linearly polarized light excites the superposition of the indirect exciton states $|+1\rangle$ and $|-1\rangle$. The decoherence time τ_{d} of this superposition is given by $h/\Delta E$, where ΔE is the

splitting between the spin states. Due to the suppression of the electron-hole exchange interaction, the spin states are degenerated and it is $\Delta E \to 0$. Thus, the decoherence time should be extremely long and optical alignment should be observable. However, it is assumed that the optical alignment of the X_{high} exciton is suppressed by the weak optical alignment of the Γ-exciton state in the same dot, see D line in Fig. 6.12 (c), which is not understood so far. This relation is discussed in the following section.
The high optical orientation degree of 73%, measured for the direct excitons in indirect QDs (D line in Fig. 6.12 (d)), can be explained by the fast energy relaxation τ_{relax} of the electron from the Γ to the X valley, which is the ground state here. Due to this fast relaxation, only a small fraction of excitons with $\tau_{\mathrm{r}} < \tau_{\mathrm{relax}}$ recombines from the Γ state. Therefore, the PL intensity of the D line is small compared to the indirect X_{high} line. The high optical orientation of the D line implies that the coherence of $|\mathrm{X}\rangle$ and $|\mathrm{Y}\rangle$ in the direct superposition state, which is excited by the circularly polarized light, is preserved for these short-lived Γ excitons with $\tau_{\mathrm{r}} < \tau_{\mathrm{d}}$.

It should be noted that the occurrence of linear polarization can, in principle, also result from the mixing of heavy and light hole states in the C_{2v}-symmetric QDs, as it is the case for the GaAs/AlAs QW in zero magnetic field (Sec. 5.2). However, as the transverse g factor of the heavy-hole is very small (see Tab. 6.2), also in comparison with the in-plane g factor of the studied GaAs/AlAs QW, the mixing can be neglected [29].

6.3.2 Spin decoherence and ΓX relaxation

In order to study the spectral dependence of the polarization properties, the measurements described above were repeated for several excitation energies between $E_{\mathrm{exc}} = 1.57$ eV and 1.77 eV. Particular attention is paid to the transition region between direct and indirect QDs. The optical alignment (filled circles) and orientation degrees (open circles) of the direct D line (red) and the two indirect exciton lines X_{low} and X_{high} (blue and green) are presented in Fig. 6.13. In (a), the values are plotted in dependence of the excitation energy to compare polarization properties for QDs with the same size, while in (b) the dependence on the emission energy of the respective PL line is shown. In the latter case, the values for the optical alignment of the X_{low} and X_{high} excitons merge.
The degree of optical alignment, indicated by the filled circles in Fig. 6.13 (a) and (b), demonstrates a step-like function of the (excitation) energy. The high plateau, with about 50% polarization degree (filled, red), is found in the spectral region of the direct QDs ($E_{(\mathrm{exc})} < E_{\Gamma\mathrm{X}}^{\mathrm{low}}$) and the low plateau, with about 3% polarization degree (filled, green), is measured for indirect PL lines with $E_{(\mathrm{exc})} > E_{\Gamma\mathrm{X}}^{\mathrm{high}}$. In between the polarization degree of the X_{low} line (filled, blue) decreases linearly.
The optical orientation degree is indicated by the open circles. For direct excitons (open, red), it is about 1% in direct QDs and starts to increase in indirect QDs with $E_{(\mathrm{exc})} < E_{\Gamma\mathrm{X}}^{\mathrm{low}}$. For higher energies the values seem to approach 100% asymptotically. The optical orientation degree of the indirect X_{low} line (open, blue) starts to increase from 2% at $E_{\Gamma\mathrm{X}}^{\mathrm{low}}$ up to almost 22% for $E_{\mathrm{exc}} = 1.71$ eV and $E = 1.66$ eV and decreases for higher (excitation) energies. The X_{high} line (open, green) appears with an optical orientation degree of 42% at $E_{\Gamma\mathrm{X}}^{\mathrm{high}}$. For higher (excitation) energies its optical orientation degree decreases.

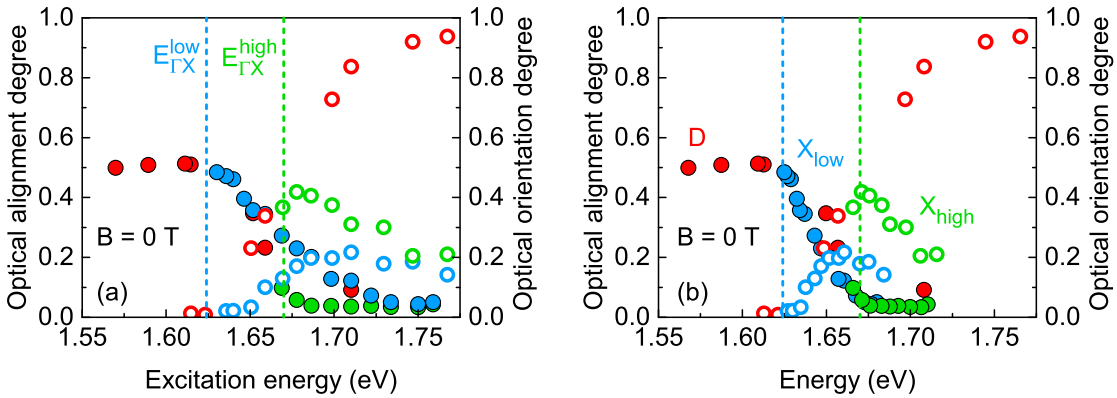

Figure 6.13: Optical alignment (filled circles) and optical orientation degree (open circles) measured for direct (red: D) and indirect exciton lines (blue: X_{low}, green: X_{high}) and plotted in dependence of **(a)** the excitation energy and **(b)** the spectral energy of the respective PL feature. The dashed lines show the ΓX-transition energies $E_{\Gamma X}^{\mathrm{low}}$ and $E_{\Gamma X}^{\mathrm{high}}$. $T = 10$ K.

Apart from the (bright) fine structures of direct and indirect excitons, which are discussed in the context of Fig. 6.12, the spectral dependencies of the optical orientation and alignment in Figs. 6.13 (a) and (b) provide further details and information. It was expected that the appearance of optical orientation and the disappearance of optical alignment would coincide with a spectrally sharp change in polarization when moving from direct to indirect QDs at $E_{\Gamma X}^{\mathrm{low}}$. However, the transition is extended to the spectral region between $E_{\Gamma X}^{\mathrm{low}}$ and $E_{\Gamma X}^{\mathrm{high}}$. In the following this effect is discussed for the two types of polarizations.

1.) Optical orientation: The gradual increase of the optical orientation degree, from zero up to 94%, measured for direct excitons in indirect QDs (open, red) can be explained by the increase of the average Γ-exciton recombination rate, which reduces the effect of decoherence. The increase of the recombination rate is due to the acceleration of the energy relaxation from the Γ to the X level. The relaxation process is nonradiative and mediated by phonon scattering. Therefore, it is most effective when the energy difference $\Delta E_{\Gamma X}$ between the Γ and the X state overcomes the phonon energies in the QDs. In InAs, the LO-phonon energy is 30 meV and in AlAs it is 49 meV [82]. From the experimental data in (a) and (b) it can be seen that the strongest slope of the optical orientation degree is measured for $E_{(\mathrm{exc})} = E_{\Gamma} = 1.672$ eV. The X-exciton energy for these QDs can be calculated by Eq. (6.4) to $E_{\mathrm{X}}^{\mathrm{low}} = 1.644$ eV. Thus, the energy difference $\Delta E_{\Gamma X}$ is given by 28 meV, which is in good agreement with the LO-phonon energy of InAs.
For the largest indirect dots, with $E_{\Gamma X}^{\mathrm{low}} < E_{\Gamma} < 1.644$ eV, $\Delta E_{\Gamma X}$ is smaller than the LO-phonon energy and the energy relaxation time from the Γ to the X state can become longer than the decoherence time of the direct excitons: $\tau_{\mathrm{relax}} > \tau_{\mathrm{d}} \approx 10$ ps (Sec. 6.3.1). Since only short-lived Γ excitons with $\tau_{\mathrm{r}} < \tau_{\mathrm{relax}}$ recombine directly, a certain amount recombines at $\tau_{\mathrm{d}} < \tau_{\mathrm{r}} < \tau_{\mathrm{relax}}$ under the emission of unpolarized light. This leads to the reduction of the optical orientation degree of the Γ exciton in this spectral region, as it

can be seen by the open red circles between $E_{\Gamma X}^{\text{low}}$ and $E_{\Gamma X}^{\text{high}}$.
In smaller indirect QDs, with $E_\Gamma > 1.644$ eV, $\Delta E_{\Gamma X}$ is larger than the LO-phonon energy and the energy relaxation time of the Γ excitons becomes faster, approaching the decoherence time. Thus, the percentage of Γ excitons recombining at $\tau_r < \tau_d$, under emission of circular polarized light, increases. For sufficiently small QDs, τ_{relax} falls below τ_d and it is $\tau_r < \tau_{\text{relax}} < \tau_d$. In this case, all excitons that recombine from the Γ state are circular polarized, resulting in a optical orientation degree of 100%. In Fig. 6.13, the maximal optical orientation degree of the D line is 93% (open red circles). The difference might be due to depolarization caused by acoustic phonons, since the D line is the acoustic phonon replica of the Γ exciton transition, see Sec. 6.1.2.

For the indirect exciton X_{low}, the increase of the optical orientation degree (open blue circles) with increasing (excitation) energy can be explained by the considerations made above. In case of large indirect QDs, with a small energy gap $\Delta E_{\Gamma X}$ between Γ and X valley, the energy relaxation time τ_{relax} is longer than the decoherence time τ_d. Therefore, the optical orientation is already lost when the exciton relaxes to the X state. The optical orientation degree of the direct exciton emission is the upper limit for the polarization of the indirect exciton emission, see open circles in Fig. 6.13 (a). Thus, the increase of the Γ-exciton polarization results in the increase of the X-exciton polarization.
In case of small indirect QDs, where $\Delta E_{\Gamma X}$ is higher than the LO-phonon energy, the energy relaxation time becomes shorter than the decoherence time of the Γ state. Therefore, the circular polarization of the laser light should be preserved up to 100% when the exciton relaxes to the X state. The strong difference between the optical orientation of Γ and X excitons in Fig. 6.13 (a) is explained in Sec. 6.5 by the depolarization of the X exciton in the nuclear field. For the highest (excitation) energies used, the optical orientation degree of the X_{low} and the X_{high} excitons decreases. This can be explained by the widening of the energy gap $\Delta E_{\Gamma X}$ to energies above the LO-phonon energies. In this case the energy relaxation requires the scattering of the Γ exciton with several optical phonons, which enhances the depolarization.

2.) Optical alignment: The energy dependence of the optical alignment degree in the spectral ΓX-transition region is not fully understood up to now. Following the considerations above, it is expected that the optical alignment degree should increase strongly with the appearance of the lower X level. The opposite effect is observed, see red filled circles in Fig. 6.13.
However, for the Γ (filled, red) and the X_{low} excitons (filled, blue), the measuerd degrees of optical alignment are about the same for the same dot, see (a). This requires an extremely long decoherence time τ_d of the circularly polarized X exciton states, comparable to the recombination time, which is several hundreds nanoseconds (see Fig. 6.8 (c)). Since τ_d is given by $h/\Delta E$ [6], where ΔE is the splitting between the circularly polarized $|+1\rangle$ and $|-1\rangle$ states here, this long decoherence time might be due to the degeneration of spin states ($\Delta E \to 0$) for indirect excitons. Since the hyperfine interaction is an important source of decoherence, an upper limit of the spin decoherence time in a single quantum dot can be calculated by the number of nuclei N in the dot and the hyperfine coupling constant A [104]. The latter is determined in Sec. 6.5.2 to $A_{\text{As}}^{\parallel} = 10.4$ μeV. For the studied structure with $N = 5 \cdot 10^4$ per dot, the upper limit of τ_d is given by

$\hbar N/A \approx 3$ μs, which is much higher than the recombination time of the X excitons. Other decoherence channels can lead to a further reduction of τ_d.

6.3.3 Conclusion

The study of the polarization properties in absence of external magnetic fields reveals important information about the bright fine structure of the excitons in the (In,Al)As/AlAs QD ensemble. For Γ excitons in direct QDs, the anisotropic electron-hole exchange interaction mixes and splits the pure spin states $|+1\rangle$ and $|-1\rangle$ to the linearly polarized $|X\rangle$ and $|Y\rangle$ states. This is confirmed by the detection of optical alignment. For X excitons in indirect QDs, the suppression of the electron-hole exchange interaction, which was theoretically predicted in Ref. [30], is demonstrated by the occurrence of optical orientation. It turns out that degree of optical orientation is limited by the loss of coherence in the Γ state, due to the relatively long relaxation time from the Γ to the X state. Since the energy relaxation is accompanied by the emission of phonons, it is accelerated if the ΓX splitting $\Delta E_{\Gamma X}$ is higher the LO-phonon energy. For the largest indirect QDs with a smaller ΓX splitting, the energy relaxation time exceeds the decoherence time of the Γ exciton, which leads to the reduction of the optical orientation degree in these dots.
Moreover, the suppression of the electron-hole exchange interaction for indirect excitons and the related degeneration of the spin states might also lead to a very long decoherence time of the superposition state, resulting in the optical alignment of the X excitons. However, since the relatively low optical alignment of the higher energetic Γ excitons in indirect QDs is not understand, further studies are necessary to verify this assumption.

6.4 Anisotropic exchange splitting affected by ΓX mixing

In the previous section, it is found that the bright Γ-exciton states of the (In,Al)As/AlAs QD ensemble are split and mixed by the anisotropic exchange interaction, while the electron-hole exchange interaction is suppressed for indirect excitons. In this section the anisotropic exchange splitting δ_1 between the linearly polarized Γ-exciton states $|X\rangle$ and $|Y\rangle$ is measured. The spectral dependence and the splitting at the ΓX-transition energies $E_{\Gamma X}^{\mathrm{low}}$ and $E_{\Gamma X}^{\mathrm{high}}$ (see Sec. 6.1.4) are of particular interest here. Two different techniques, a macroscopic and a microscopic one, are presented and compared. In both cases, the studied sample is RC 1517.

6.4.1 Macroscopic measurements on the QD ensemble

An ensemble of QDs offers several advantages over single QDs like the higher PL intensity and the possibility to perform size-dependent measurements by selective excitation. However, due to homogeneous broadening, the width of these selectivly exited PL lines is in the range of 6 meV (see Fig. 6.14), which is much broader than the expected anisotropic exchange splitting of a few hundred μeV [18]. Therefore, it is not possible to measure the spectral splitting between the oppositely polarized PL lines, which are emitted from the $|X\rangle$ and $|Y\rangle$ states.
The macroscopic technique used here is based on the fact that the anisotropic exchange splitting of direct excitons can be exceeded by the Zeeman splitting in a longitudinal magnetic field [81]. In zero magnetic field, the pure spin states $|+1\rangle$ and $|-1\rangle$ are split

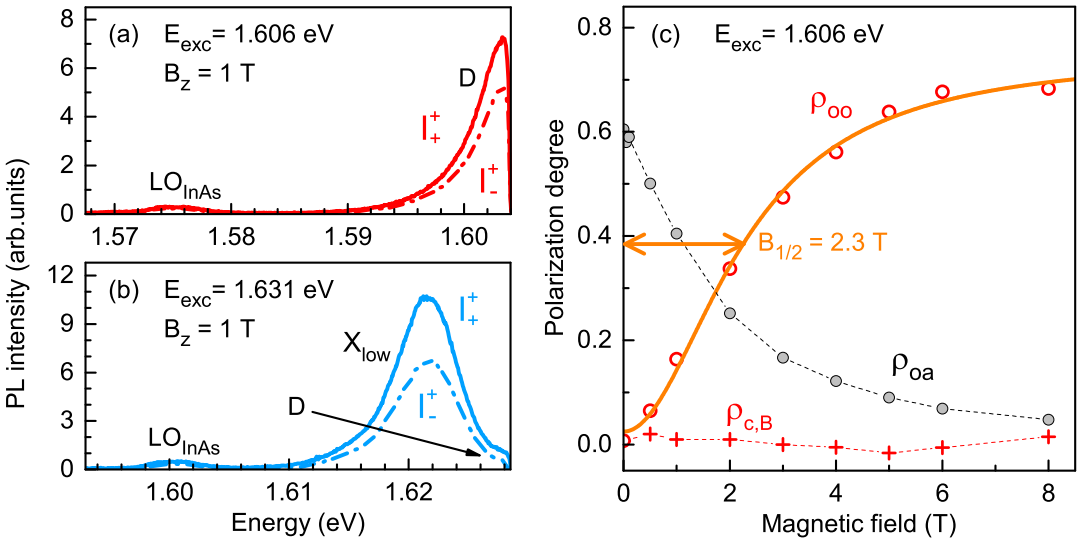

Figure 6.14: **(a)** and **(b)** Circularly polarized intensity components I_+^+ and I_-^+ of the PL spectra emitted by (a) direct and (b) indirect QDs under σ^+ polarized excitation. The longitudinal magnetic-field strength is 1 T. **(c)** Degree of the optical orientation (red circles), the magnetic field induced polarization (red crosses) and the optical alignment (grey dots) of the D line emitted by direct QDs ($E_{\mathrm{exc}} = 1.606$ eV) in dependence of the longitudinal magnetic-field strength. The orange line shows a Lorentzian function, which is fitted to ρ_{oo} with a HWHM of $B_{1/2} = 2.3$ T. $T = 1.8$ K. Dashed lines are guides for the eye.

and mixed by the electron-hole exchange interaction (see Fig. 2.1). Thus, the degree of optical alignment is high, while optical orientation is negligible (see Sec. 6.3). When a magnetic field B_z is applied parallel to the growth axis of the sample (Faraday geometry), the Zeeman splitting between $|+1\rangle$ and $|-1\rangle$ increases and the mixing is lifted. This leads to the arise of the optical orientation and the decrease of the optical alignment. The anisotropic exchange splitting δ_1 between the bright Γ-exciton states can be determined by the magnetic field dependence of the optical orientation degree ρ_{oo}. The so-called polarization recovery curve is given by:

$$\rho_{\mathrm{oo}}(B_z) = \rho_{\mathrm{oo}}^0 \frac{\left(\mu_{\mathrm{B}} g_z^{(\mathrm{Ex})} B_z\right)^2}{\delta_1^2 + \left(\mu_{\mathrm{B}} g_z^{(\mathrm{Ex})} B_z\right)^2} \text{[81]}, \tag{6.10}$$

with the high-field limit ρ_{oo}^0 of the optical orientation degree, the Bohr magneton μ_{B} and the longitudinal g factor $g_z^{(\mathrm{Ex})}$ of the Γ exciton.

For the studied sample, the optical orientation degree of the Γ exciton, ρ_{oo}, is calculated from the intensities of the circularly polarized PL, which is emitted by the D line under circularly polarized excitation. In addition, the magnetic field induced polarization $\rho_{\mathrm{c},B}$ is determined. The techniques are described in Sec. 3.2.2. Figure 6.14 (a) shows the PL spectra of the intensity components I_+^+ and I_-^+, emitted from selectively excited

direct QDs ($E_{\mathrm{exc}} = 1.606$ eV) for $B_z = 1$ T. The magnetic-field dependencies of ρ_{oo} and $\rho_{\mathrm{c},B}$ are presented in (c) by the open red circles and the red crosses. Dashed lines are guides for the eye. A Lorentzian function (orange line) with a half width at half maximum (HWHM) of $B_{1/2} = 2.3$ T is fitted to the data points of ρ_{oo}. With Eq. (6.10), the anisotropic exchange splitting can be determined via $\delta_1 = B_{1/2}\mu_{\mathrm{B}} g_z^{(\mathrm{Ex})}$. The g factor of the Γ exciton is calculated by the heavy-hole g factor $g_z^{(\mathrm{hh})} = 2.43$ [29] and the electron g factor $g_z^{(\mathrm{e})} = -0.2$ [47]. With the resulting direct exciton g factor of $g_z^{(\mathrm{Ex})} = 2.63$, the anisotropic exchange splitting is $\delta_1 = (346 \pm 35)$ μeV for $E_{\mathrm{exc}} = 1.606$ eV.
It turns out that magnetic field induced polarization degree $\rho_{\mathrm{c},B}$ is negligible. This indicates a short exciton recombination time in comparison with the spin-relaxation time [103] for the Γ excitons. For completeness, the degree of optical alignment ρ_{oa} is given by the grey dots. It is calculated from the linear polarized intensity components under linear polarized excitation (see Sec. 3.2.2). The decrease of the optical alignment with increasing magnetic-field strength is in line with the considerations made at the beginning of this section.

In principle, the presented technique for determining δ_1 can be applied to direct and indirect QDs of all sizes (energies) in the ensemble. However, in practice, it can be difficult to measure the PL intensities I_+^+ and I_+^- of the D line. This is shown in Fig. 6.14 (b) for the case of indirect QDs ($E_{\mathrm{exc}} = 1.631$ eV). Especially for excitation energies slightly above the ΓX-transition energy, the overlap of direct and indirect exciton emission and the small PL intensity of the D line hinder an accurate measurement. For this reason, the anisotropic exchange splitting is only determined for three different excitation energies using the macroscopic technique. These results are presented in Fig. 6.16 (c) by the red triangles together with the results of the microscopic technique (black dots), which is described in the following section.

6.4.2 Microscopic measurements on single QDs

For the direct measurement of δ_1, the splitting is determined by the distance between two oppositely linearly polarized PL lines, which are emitted from the Γ-exciton states $|\mathrm{X}\rangle$ and $|\mathrm{Y}\rangle$ of a single QD. Although the idea is simple, the measurement is technically challenging. First, a mesa structure is etched into the sample to reduce the number of QDs, which are excited by the laser beam. For the excitation of a single mesa and the detection of its PL a microscope objective is used. Further details about the sample preparation and the experimental setup are given in Sec. 3.4.
Figures 6.15 (a) and (b) show two exemplary PL spectra from different mesas under nonresonant excitation. It can be seen, that the broad emission spectrum of the QD ensemble (compare Fig. 6.6 (a)) is lost here. Instead, single PL lines and small groups of lines are randomly distributed along the spectra. They appear in the direct QD range ($E < E_{\Gamma\mathrm{X}}^{\mathrm{low}} = 1.611$ eV) as well as in the indirect range ($E > 1.611$ eV). In the latter case, the PL lines can stem from the recombination of direct or indirect excitons.
The source of the emitted light (direct / indirect QDs) is determined by measuring the recombination times for several PL lines of the spectrum. Figure 6.15 (c) shows the decay curve of a PL line at 1.642 eV. It can be fitted by the sum of two exponential functions (violet line) with the time constants / recombination times $\tau_{\mathrm{fast}} = 0.9$ ns and

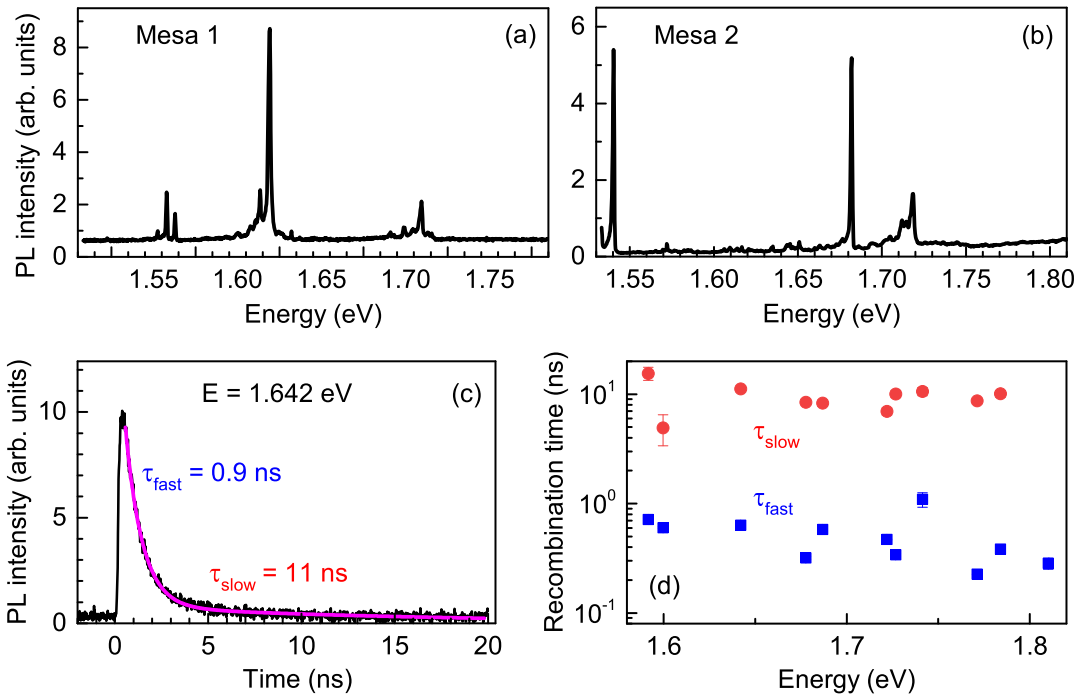

Figure 6.15: **(a)** and **(b)** Unpolarized micro-PL spectra measured under nonresonant excitation of two different mesas on the (In,Al)As/AlAs QD sample. **(c)** Time-resolved PL intensity of a single PL line at $E = 1.642$ eV, measured under pulsed, nonresonant excitation. The violet line shows the result of fitting the sum of two exponential functions to the data points. The corresponding time constants τ_{fast} and τ_{slow} are given in the figure. **(d)** Spectral dependence of the time constants τ_{fast} (blue squares) and τ_{slow} (red dots). $T = 8$ K.

$\tau_{\text{slow}} = 11$ ns. The spectral dependencies of the fit parameters τ_{fast} (blue squares) and τ_{slow} (red dots) are presented in Fig. 6.15 (d). It can be seen, that the recombination times are constant in the whole spectral range. Even in the energetic region of indirect QDs the values are in good agreement with the recombination times which were found for direct excitons under selective excitation in Sec. 6.2.1. Thus, it can be stated that the detected PL lines result from the recombination of Γ excitons only.

Finally, it is necessary to clearly identify the pairs of lines that are split by the anisotropic exchange interaction. The direct exciton states $|\text{X}\rangle$ and $|\text{Y}\rangle$, are linearly polarized. When a QD is excited nonresonantly by a continuous-wave laser, both states are populated with the same probability and the two PL lines show about the same intensity. With a well-set two-channel detection, for orthogonally linear-polarized light, only the respective PL line is detected.

Figure 6.16 (a) and (b) show examples of split PL lines at two different detection energies. The color of the lines represents the angle of the $\lambda/2$ plate, which is used to select the linear polarized PL, aligned either to the x or to the y axis of the sample (see Sec. 3.2.1). For the two presented cases, with $\delta_1(1.5615\text{ eV}) = 602$ μeV and $\delta_1(1.6537\text{ eV}) = 53$ μeV, the splittings of the lines differ by a factor of more than 100. The full spectral dependence of the anisotropic exchange splitting is plotted in Fig. 6.16 (c) together with the results

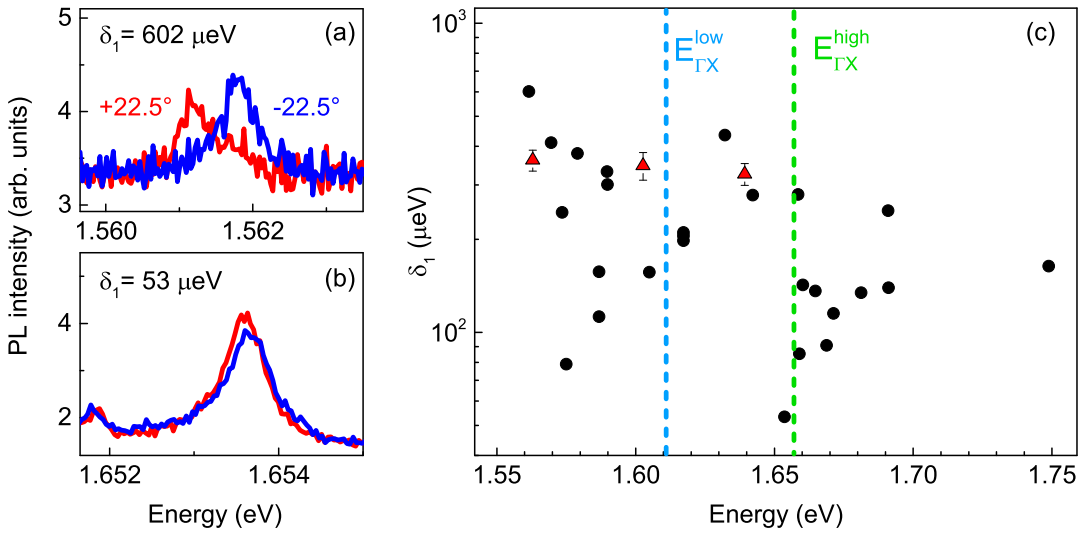

Figure 6.16: **(a)** and **(b)** Linearly polarized PL lines at two different detection energies. The two angles of the $\lambda/2$ plate, +22.5°(red) and -22.5°(blue), are equivalent to the x and y axes of the sample. $B = 0$ T. **(c)** Anisotropic exchange splitting in dependence of the detection energy, measured with the macroscopic (red triangles) and the microscopic technique (black dots). The ΓX-transition energies are marked by the dashed lines. $T = 8$ K.

of the macroscopic technique (red triangles). Split lines are found from $E = 1.5615$ eV up to $E = 1.749$ eV. Between these energies, δ_1 decreases from 602 μeV down to 164 μeV. At about 1.60 eV and 1.66 eV two minima are visible. Here, the splitting drops down to 80 μeV or 53 μeV respectively.

In general, the anisotropic exchange splitting of the Γ-exciton states can vary widely for different QD sizes, shapes and compositions. Typical values for InAs/GaAs QDs are 100 - 1000 μeV [105]. In this regard, the results in Fig. 6.16 (c) meet the expectations. The two minima of δ_1 are found close to the ΓX-transition energies $E_{\Gamma X}^{\text{low}} = 1.611$ eV and $E_{\Gamma X}^{\text{high}} = 1.657$ eV, which are determined in Sec. 6.1.4. For X excitons, the electron-hole exchange interaction is weakened, as the wave functions of X electron and Γ hole hardly overlap in momentum space [30]. Therefore, it can be stated that the strong decrease of the anisotropic exchange splitting is caused by the ΓX mixing of the electron wave function.

6.4.3 Conclusion

Two different techniques are used to determine the anisotropic exchange splitting δ_1 of direct excitons in an ensemble of direct and indirect (In,Al)As/AlAs QDs. It turns out that both techniques lead to comparable results. However, only the microscopic technique can deliver results for the spectral range of the ΓX transition, where δ_1 decreases strongly. The strong decrease is attributed to the suppression of the electron-hole exchange interaction for indirect excitons.

6.5 X excitons in nuclear and external magnetic fields

Usually, the presence of nuclear fields is the main reason for the depolarization of exciton spins in QDs [106], [107]. Nuclear spins act as local magnetic fields with randomly fluctuating directions. Via hyperfine interaction, they can basically have the same effects on excitons like an external magnetic field.
The impact of a magnetic field B on the observed spin polarization depends on the angle θ between B and z and on the g factors of the excitons or carriers. A longitudinal magnetic field ($B \parallel z$) causes the energetic splitting (ΔE_Z) of the pure exciton spin states $|+1\rangle$ and $|-1\rangle$, the Zeeman effect. In case of $\tau_\mathrm{s} < \tau_\mathrm{r}$ and $\mathrm{k_B}T < \Delta E_\mathrm{Z}$, the splitting can lead to the increase of the circular polarization degree. This is the magnetic field induced polarization, which is observed for the indirect GaAs/AlAs QW in Sec. 5.1. In contrast, the Larmor precession of the exciton spins around a transverse magnetic field ($B \perp z$) leads to their depolarization. This is the Hanle effect, which is commonly used to determine the spin lifetime T_s of the carriers [67]. In case of randomly aligned nuclear fields, the depolarization can be counteracted by an external, longitudinal magnetic field [22]. The related field dependence is called polarization recovery curve (PRC) [108].
A common tool to investigate the polarization effects of electrons in external or nuclear fields is the optical orientation. In Sec. 6.3, the optical orientation of indirect QD excitons is demonstrated for $B = 0$. Here, it is studied in longitudinal and transverse magnetic fields. It should be noted that all measurements presented in this section refer to the circular polarization degree ρ_c^+, as it is defined in Sec. 3.2.2. However, since these measurements were performed under cw excitation and it is $\tau_\mathrm{s} > \tau_\mathrm{r}$ for sample AG 2890 (see Sec. 6.5.1 and Sec. 6.6.2), the circular polarization degree under polarized excitation is to be equated with optical orientation degree.
The subsequent sections are organized as follows: In Sec. 6.5.1, the impact of the nuclear fields on the Hanle curve is studied in dependence of the sample temperature. The microscopic model, which describes the hyperfine interaction with the X electron (see Sec. 2.5), is compared with the experimental results in Sec. 6.5.2. In Sec. 6.5.3, the g-factor anisotropy of the indirect QD excitons is determined by the application of tilted magnetic fields in order to identify the dominating spin state. Finally, in Sec. 6.5.4, the depolarization mechanisms during the Γ state of the exciton and their influence on the X-exciton spin polarization are investigated and discussed.

6.5.1 The Hanle curve: Nuclear fields vs. spin lifetime

In an external transverse magnetic field, the Larmor precession around the field direction can cause the depolarization of the carrier spins, which is known as the Hanle effect. The necessary field strength is directly realted to the spin lifetime of the carriers. However, it was already found in Ref. [70] that this relation does not hold for the indirect excitons of the (In,Al)As/AlAs QD ensemble. In this section, the mismatch will be explained by the presence of nuclear magnetic fields. The investigation of the circular polarization degree in transverse and longitudinal magnetic fields is carried out at the X_high exciton, since its optical orientation degree in zero magnetic field is comparatively high, see Fig. 6.13 (a).

Figure 6.17 (a) shows the X-exciton polarization in dependence of the magnetic field

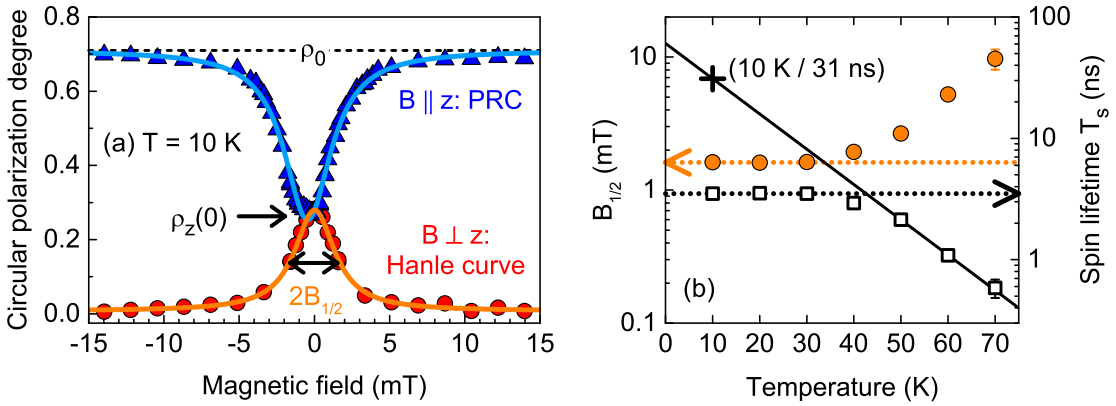

Figure 6.17: Results for X_{high} excitons in indirect QDs with $E_{exc} = 1.698$ eV and $E = 1.683$ eV: **(a)** Circular polarization degree as a function of the magnetic field strength. The polarization recovery curve (PRC, blue triangles) is measured in Faraday geometry, the Hanle curve (red dots) in Voigt geometry. The colored lines show Lorentz functions fitted to the data points with half widths of $B_{1/2} = 1.89$ mT (PRC) and $B_{1/2} = 1.62$ mT (Hanle). **(b)** Half width $B_{1/2}$ of the Hanle curve (orange circles) and the calculated spin lifetime T_s (black squares) by Eq. (2.8) in dependence of the sample temperature. Dotted lines are guides for the eye. The black cross marks the spin lifetime at $T = 10$ K for the exponential extrapolation (solid line).

strength in Faraday (blue triangles) and Voigt geometry (red circles). The excitation energy is $E_{exc} = 1.698$ eV and the detection energy $E = 1.683$ eV is the spectral energy of the X_{high} exciton. At 10 K, the circular polarization degree can be increased from $\rho_z(0) = 27.5\%$ up to $\rho_0 = 71\%$ by a longitudinal magnetic field. In a transverse field, the Hanle curve is observed, which reduces the circular polarization degree down to 1%. The two curves are well described by Lorentz functions with half widths at half maximum (HWHM) of $B_{1/2} = 1.89$ mT for $B \parallel z$ and $B_{1/2} = 1.62$ mT for $B \perp z$. The Lorentz fit of the PRC (blue) is slightly shifted by -0.45 mT from zero.
The half width of the Hanle curve is plotted in Fig. 6.17 (b) in dependence of the temperature, shown by the orange dots. It can be seen that $B_{1/2}$ is constant at about 2 mT for $T \leq 30$ K. For higher temperatures, it increases up to 10 mT at 70 K. According to (Eq. 2.8), one can calculate the spin lifetime from the half width of the Hanle curve via $T_s = \hbar/(g_e \mu_B B_{1/2})$, where g_e is the transverse g factor of the electron. Although this relation refers to a free electron, it can be applied to the indirect exciton since the transverse g factor of the heavy hole is negligible and for the X electron it is equal to the free electron g factor, see Tab 6.2. The results for T_s are shown by the black squares in (b). For low temperatures, the calculated spin lifetime is constant at 3.5 ns. When the temperature is increased above 30 K, the calculated spin lifetime starts to decrease. At 70 K it is 0.6 ns.

At first glance, the results in Figs. 6.17 (a) and (b) are contradictory. The application of a longitudinal magnetic field leads to the restoration of the circular polarization degree up to 71%, as it can be seen by the blue curve in (a). Due to this high optical orientation of the X exciton, it follows from Eq. (2.7) that the spin relaxation time τ_s

is much longer than the exciton recombination time τ_r. Thus, accoring to Eq. (2.6), the spin lifetime T_s is mainly determined by τ_r, which is several hundreds ns for the studied sample (Sec. 6.2.1). For the studied case ($E = 1.683$ eV, $T = 10$ K), the exciton recombination time is about 40 ns. This value was obtained by the measurements presented in Sec. 6.2.1. It is more than 10 times longer than the calculated result for the spin lifetime in Fig. 6.17 (b), see black squares. Moreover, considering that the increase of the temperature usually leads to the decrease of the spin lifetime [109], the temperature independence of T_s for $T \leq 30$ K is remarkable.
However, the results can be explained by the presence of nuclear spins with sufficiently strong nuclear fields. The spins of the nuclei are randomly fluctuating. Assuming that these fluctuations are slow compared to the electron spin dynamics, they can be considered as frozen nuclear fields B_N [22]. The electron spins precess around the respective direction of B_N with the Larmor frequency $\Omega = \mu_B g_e B_N/\hbar$. B_N depends on the strength of the hyperfine interaction between the nuclei and the electrons. In case of isotropic hyperfine interaction, 2/3 of the initial electron spin polarization is lost by the Hanle effect caused by B_N. The remaining 1/3 of the polarization, unaffected by nuclear spin projections along z, can be destroyed by the Hanle effect of an external, transverse magnetic field ($B \perp z$), as it can be seen in Fig. 6.17 (a) by the red curve. With increasing magnetic field, the composite vector $\vec{B} + \vec{B_N}$ starts to turn to the direction of B. For $B \gg B_N$ the polarization is lost completely.
The initial polarization of the electron, ρ_0, without the depolarization by nuclear fields, can be restored by applying a longitudinal magnetic field ($B \parallel z$). When the external field overcomes the nuclear fields that are aligned perpendicular to z, the depolarization of the electron spins is suppressed. Therefore, the half widths of the PRC and the Hanle curve are both determined by B_N. This effect can be seen by comparing the blue curve, which can now be identified as PRC, and the red Hanle curve in Fig. 6.17 (a). In the longitudinal field, the polarization is restored from $\rho_z(0) = 27.5\%$ to $\rho_0 = 71.0\%$. The ratio $\rho_0/\rho_z(0) = 2.58$ is comparable to the ratio of 3 in case of isotropic hyperfine interaction.

The considerations above lead to the conclusion that for $B_N > \hbar/g_e\mu_B T_s$, the half width of the Hanle curve is not determined by the spin lifetime of the electron but by the strength of the nuclear field. For simplification, it is assumed that B_N is equal to the half width of the Hanle curve. Then the inequation above becomes invalid for $T_s < 3.5$ ns. For the studied QDs this means that only spin lifetimes of less than 3.5 ns can be determined by measuring the Hanle curve. This condition is fulfilled for temperatures above 30 K, see Fig. 6.17 (b). In order to remove the effect of the nuclear spins from the analysis, the calculated spin lifetimes for $T > 40$ K are fitted with an exponential function (black diagonal line). Typical functions to describe the influence of the temperature on the spin lifetime have a linear or quadratic dependence [109]. However, with the exponential fit function the spin lifetime for $T = 10$ K is estimated to 31 ns (black cross), which is comparable to the experimental result of 40 ns, gained by time-resolved measurements (Sec. 6.2.1).
The restored circular polarization degree of the indirect exciton, $\rho_0 = 71\%$, is only slightly smaller than 73%, the circular polarization degree of the direct exciton for the same excitation energy $E_{exc} = 1.698$ eV (see Fig. 6.13 (a)). Two statements can be derived from this fact. Via Eq. (2.7), a lower limit for the ratio of the spin relaxation time and the

exciton recombination time can be calculated. With an initial polarization of $\rho_\mathrm{i} \leq 0.73$ and $\rho = 0.71$ it is $\tau_\mathrm{s}/\tau_\mathrm{r} \geq 36$ for the X_high exciton, which is in good agreement with the result in Sec. 6.6.2. Moreover, it can be stated that the depolarization due to the energy relaxation from the Γ to the X level is small for this exciton energy. This confirms the considerations made in Sec. 6.3.2: Since the energy difference between the Γ to the X level (here: $\Delta E_{\Gamma X} = 15$ meV) is small compared to the phonon energies in the QDs ($\mathrm{TA_{AlAs}}$: 12 meV, $\mathrm{LO_{InAs}}$: 30 meV, $\mathrm{LO_{AlAs}}$: 49 meV [82]), the energy relaxation can be mediated by a single scattering process. This reduces the depolarization.

6.5.2 Application and limits of the microscopic model

In the section above it is demonstrated that at low temperatures and magnetic fields the spin polarization is determined by the hyperfine interaction with the nuclear spins. The study of the hyperfine interaction in indirect QDs is interesting since the wave functions of the X electrons are not of pure s type but contain also p-type contributions [56]. In direct QDs, the s symmetry of Γ electrons is causing a strong Fermi contact coupling, which is usually the main part of the hyperfine interaction [110]. A different symmetry of the Bloch amplitudes leads to the reduction of the hyperfine coupling constant [111]. Therefore, it is assumed that the hyperfine interaction is weakened for indirect band gap electrons, like it is the fact for holes [106], with an approximate p-type wave function. A weak hyperfine interaction can lead to very long spin-decoherence times, exceeding the μs range [104]. This property, together with a long exciton lifetime, is highly interesting for spintronic applications.
In this section, PRCs for different exciton energies and temperatures are compared with the microscopic model, which is introduced in Sec. 2.5. As a first step, an important condition for the applicability is determined. After that, the model is applied to a suitable data set, which allows the quantification of the hyperfine interaction.

Figure 6.18 (a) shows the theoretical ratio of the zero field polarization $\rho_z(0)$ and the restored polarization ρ_0 of a X electron as a function of the hyperfine anisotropy factor ε. The values are calculated by Eq. (2.49) with $\Delta_x = 1$ and $\Delta_y = \Delta_z = \varepsilon$ for the x-valley electron (blue) and $\Delta_z = 1$ and $\Delta_x = \Delta_y = \varepsilon$ for the z-valley electron (red). The results for the y valley, with $\Delta_y = 1$ and $\Delta_x = \Delta_z = \varepsilon$, are the same as for the x valley. Note that these dependencies are independent from the strength of the nuclear field B_N. It is $\rho_0/\rho_z(0) = 3$ for isotropic hyperfine interaction with $\varepsilon = 1$ in all three valleys. In case of the z valley, it is $\rho_0/\rho_z(0) = 1$ for $\varepsilon = 0$. In between 0 and 1 the slope is roughly linear. In case of the x/y valley, $\rho_0/\rho_z(0)$ approaches ∞ for $\varepsilon \to 0$.
Experimental values for $\rho_0/\rho_z(0)$, measured for different QD sizes, are given in Fig. 6.18 (b). The first data point ($E = 1.683$ eV) is taken from Fig. 6.17 (a) in the section above. The ratio is increasing with increasing exciton energy while the slope is decreasing. Assuming a monotonic increase, it is $\rho_0/\rho_z(0) = 3$ for $E = 1.69$ eV. The temperature dependence of $\rho_0/\rho_z(0)$, measured for $E = 1.683$ eV, is given in Fig. 6.18 (c). Up to 30 K the ratio is constant at about 2.5. For higher temperatures it decreases down to 1.04 at $T = 70$ K.

By combining Fig. 6.18 (a) with (b) and (c) one could conclude that for $E < 1.69$ eV the polarized electron is located in the z valley, while for $E > 1.69$ eV it is in the x/y

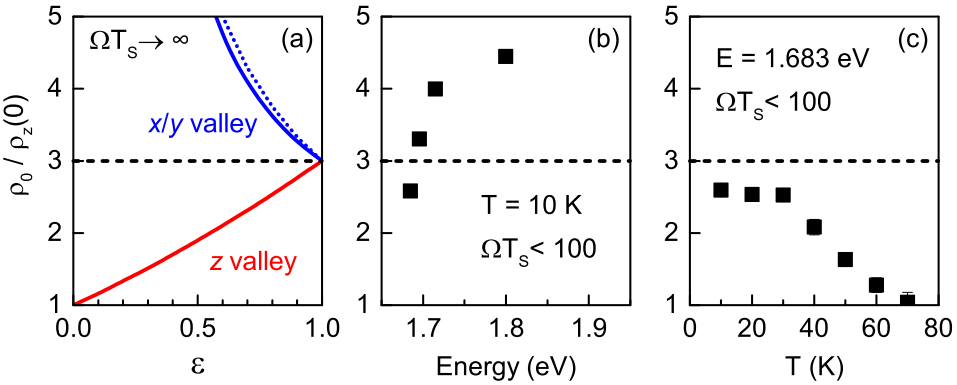

Figure 6.18: Ratio of zero field polarization $\rho_z(0)$ and restored polarization ρ_0 of the X electron / exciton in a longitudinal magnetic field ($B \parallel z$). The black, dashed lines mark the ratio $\rho_0/\rho_z(0) = 3$ in case of isotropic hyperfine interaction ($\varepsilon = 1$) and $\Omega T_\mathrm{S} \to \infty$. **(a)** Theoretical values in case of $\Omega T_\mathrm{s} \to \infty$, calculated by Eq. (2.49), for electrons in the x/y (blue) and the z valley (red) in dependence of the hyperfine-anisotropy factor ε. The dashed, blue line shows the approximation $\rho_0/\rho_z(0) = 3/\varepsilon$ taken from Eq. (6.11). **(b)** Experimental data for different emission energies, measured at $T = 10$ K. **(c)** Experimental data in dependence of the temperature, measured for $E = 1.683$ eV.

valley of the conduction band. This would be a surprise, since it is assumed that the X_z valley is significantly higher in energy than the X_x and X_y valley for all QD sizes [26]. Moreover, the results imply that the hyperfine-anisotropy factor ε, and thus the coupling constants, are not the same for different QD sizes and temperatures.
However, the results can be explained by the spin lifetime T_s of the electrons. In the microscopic model (Sec. 2.5), it is assumed that the spin lifetime is much higher than the precession period Ω^{-1} of the electron spin the in nuclear field B_N, where Ω is given by $\mu_\mathrm{B} g_\mathrm{e} B_\mathrm{N}/\hbar$. For simplicity, it can be assumed that in case of isotropic hyperfine interaction ($\varepsilon = 1$), 1/3 of the nuclear spins point to the x direction, 1/3 to the y direction and 1/3 to the z direction. If $\Omega T_\mathrm{s} \to \infty$ is fulfilled, the nuclear fields pointing to the x and y directions fully depolarize 2/3 of the electron spins, while 1/3 is stabilized by the nuclear spins pointing to the z direction. If the condition is not fulfilled, the nuclear fields, pointing to x and y directions, can not fully depolarize the electron spins during the exciton lifetime and the resulting zero-field polarization $\rho_z(0)$ is higher than 1/3. This means, that a low spin lifetime can lead to the decrease of the ratio $\rho_0/\rho_z(0)$.
Experimentally, the reduction of $\rho_0/\rho_z(0)$ is observed in (b) with decreasing exciton energy and in (c) with increasing temperature. Indeed, the exciton recombination time τ_r, which determines the spin lifetime for the indirect band gap electrons, is decreasing with decreasing exciton energy in that range (see Fig. 6.8 (b)) and the spin lifetime is decreasing with increasing temperature, see Fig. 6.17 (b). Therefore, it can be stated that a z-valley character of the polarization curves is caused by the non-fulfillment of the condition $\Omega T_\mathrm{s} \to \infty$. As a result, the highest agreement between the experimental data and the microscopic model is expected for the longest living X electrons ($E = 1.80 - 1.85$ eV) studied at temperatures below 30 K.

In order to quantify theses considerations, an approximation of $\rho_z(0)/\rho_0$, based on the

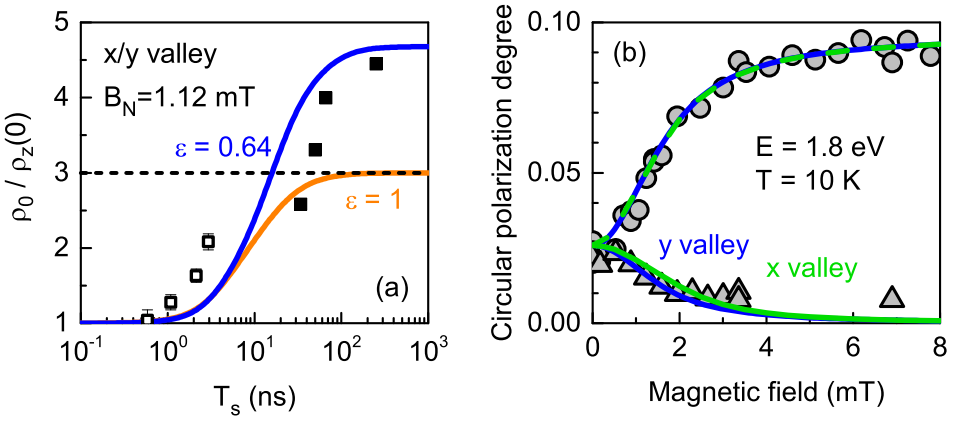

Figure 6.19: **(a)** Theoretical model for $\rho_0/\rho_z(0)$, given by the reciprocal of Eq. (6.11) with $\varepsilon = 0.64$ (blue line) and $\varepsilon = 1$ (orange line), and compared with the experimental data (squares) in dependence of the spin lifetime T_s. The open squares show the data from the temperature set in Figs. 6.17 (b) and 6.18 (c). The filled squares show the data from the energy series in Fig. 6.18 (b). The respective lifetimes are gained from the measurements presented in chapter 6.2. **(b)** Experimental data for the PRC (circles) and the Hanle curve (triangles) measured at $E = 1.80$ eV. Lines: PRC and Hanle curve, calculated by Eq. (2.49) of the microscopic model, with $\varepsilon = 0.64$ and $B_\mathrm{N} = 1.12$ mT, for X_x (green) and X_y valley electrons (blue).

Hanle curve, Eq. (2.8), is made for $x(y)$-valley electrons in dependence of the spin lifetime T_s:

$$\frac{\rho_z(0)}{\rho_0} = \underbrace{\frac{1}{3}\cdot\frac{1}{1+(\Omega T_\mathrm{s})^2}}_{x(y)\text{ axis}} + \underbrace{\frac{1}{3}\cdot\frac{1}{1+(\varepsilon\cdot\Omega T_\mathrm{s})^2}}_{y(x)\text{ axis}} + \underbrace{\frac{1}{3}\left(\frac{1-\varepsilon}{1+((1+\varepsilon)/2\cdot\Omega T_\mathrm{s})^2}+\varepsilon\right)}_{\text{z axis}} \qquad (6.11)$$

The first two terms describe the Hanle effect caused by the nuclear fields pointing to the x and the y directions. The last term represents the fraction of QDs with $B_\mathrm{N} \parallel z$. For $\Omega T_\mathrm{s} \to \infty$, only the third term contributes to the spin polarization and Eq. (6.11) becomes $\rho_z(0)/\rho_0 = \varepsilon/3$, which is a good approximation of the microscopic model, see the dashed, blue line in Fig. 6.18 (a). In case of zero hyperfine interaction, $\Omega T_\mathrm{s} = 0$, it is $\rho_z(0) = \rho_0$ and all three terms contribute equally.

Figure 6.19 (a) shows Eq. (6.11) as a function of T_s for $\varepsilon = 1$ (green) and $\varepsilon = 0.64$ (blue). B_N is 1.12 mT in both cases. The parameters $\varepsilon = 0.64$ and $B_\mathrm{N} = 1.12$ mT are taken from the analysis of the polarization curves measured at $E = 1.80$ eV, which are shown in Fig. 6.19 (b). The curves in (a) are compared with the experimental data from the temperature series (open squares), presented in Figs. 6.17 (b) and 6.18 (c), and with the data from the energy series (filled squares) presented in Fig. 6.18 (b). In the latter case, the spin lifetime T_s is assumed to be equal to the exciton recombination time gained in Sec. 6.2.

It can be seen that the theoretical curve with $\varepsilon = 0.64$ (blue) roughly describes the experimental data. The saturation of $\rho_0/\rho_z(0)$, which is equal to the case $\Omega T_\mathrm{s} \to \infty$, sets in for $T_\mathrm{s} > 100$ ns. Therefore, it can be concluded, that the microscopic model can be

applied only to the data set measured at $E = 1.80$ eV (for $T = 10$ K). This is shown in Fig. 6.19 (b).

Figure 6.19 (b) shows the experimental PRC (circles) and Hanle curves (triangles) for the exciton energy $E = 1.80$ eV and the temperature $T = 10$ K. Both curves can be described by Lorentz functions (not shown here) with half widths of $B_{1/2}^{\mathrm{PRC}} = 1.67$ mT (PRC) and $B_{1/2}^{\mathrm{Hanle}} = 1.43$ mT (Hanle curve). The circular polarization degree of the X_{high} exciton increases in the longitudinal magnetic field from 2.14% to 9.52%. Thus, the ratio $\rho_0/\rho_z(0)$ is 4.45, which corresponds, according to Fig. 6.18 (a), to $\varepsilon = 0.64$. The model curves (blue and green lines) are calculated via Eq. (2.49) and the fit parameters of the Lorentz functions: $\rho_0 = 0.952$, $\varepsilon = 0.64$ and $B_{\mathrm{N}} = B_{1/2}^{\mathrm{Hanle}}/(2\varepsilon) = 1.12$ mT, see Eq. (2.50). Experimental data and model calculations show good agreement, especially for the y valley.
With Eq. (2.46) it is now possible to calculate the coupling constant $A_{\mathrm{As}}^{\parallel}$ from the nuclear magnetic field strength B_{N}. The QD volume V can be approximated by a spherical cap with $V = \pi h(3a^2 + h)/6$, where h is the QD height and a the radius of the base. It is assumed that the shape of the dots is defined by $d = 2a = 3h$, where d is the dot diameter. For $E = 1.80$ eV, the dot diameter is estimated to be $d = 11.3$ nm [57]. With $B_{\mathrm{N}} = 1.12$ mT, $g_{\mathrm{e}} = 2$, $I = 3/2$, $V_0 = 45.1 \cdot 10^{-24}$ cm^3 and $V = 222$ nm^3 the hyperfine coupling constant is given by $A_{\mathrm{As}}^{\parallel}(\mathrm{exp.}) = 10.4$ μeV. This value is nearly three times smaller than the theoretical one, $A_{\mathrm{As}}^{\parallel}(\mathrm{theo.}) = 27.3$ μeV, given in Sec. 2.5 but still in the same order of magnitude.

In conclusion of this section, it is demonstrated for low temperatures, that frozen nuclear magnetic fields determine the spin polarization of the X_{high} electron in indirect QDs. For spin lifetimes longer than 100 ns, it is possible to apply the microscopic model from Sec. 2.5, which allows to determine the strength of the nuclear field $B_{\mathrm{N}} = 1.12$ mT, the alignment of the X valley, which is either X_x or X_y, and the hyperfine coupling constant of $A_{\mathrm{As}}^{\parallel} = 10.4$ μeV. Due to the relatively high hyperfine anisotropy factor $\varepsilon = 0.64$, the nuclear field reduces the electron spin polarization by a factor of 4.45. Thus, it can be stated, that the hyperfine interaction is an important depolarization channel for indirect QD excitons, although the coupling constants of the X electron are about 4 times smaller than for Γ electron, see Sec. 2.5. In this regard, it might be interesting to create indirect QDs with a X_z-electron ground state, since their coupling to the nuclear fields is weaker.

6.5.3 g factor anisotropy: Γ and X valley characteristics

In the two sections above, it is assumed that due to the weak electron-hole exchange interaction of indirect excitons [30], the spin polarization is determined by the electron spins only. The holes are neglected from the considerations. One aim of this section is to show that this assumption is justified for the X_{high} exciton. It is commonly known, that the g factor of the free electron is isotropic, while the g factors of the heavy hole and the exciton can be strongly anisotropic. Therefore, it is possible to distinguish between the different spin characteristics by applying tilted magnetic fields, like it was demonstrated for trions in Ref. [112]. In fact, the situation for trions is comparable to indirect excitons, since the electron-hole exchange interaction is also suppressed for trions in the ground

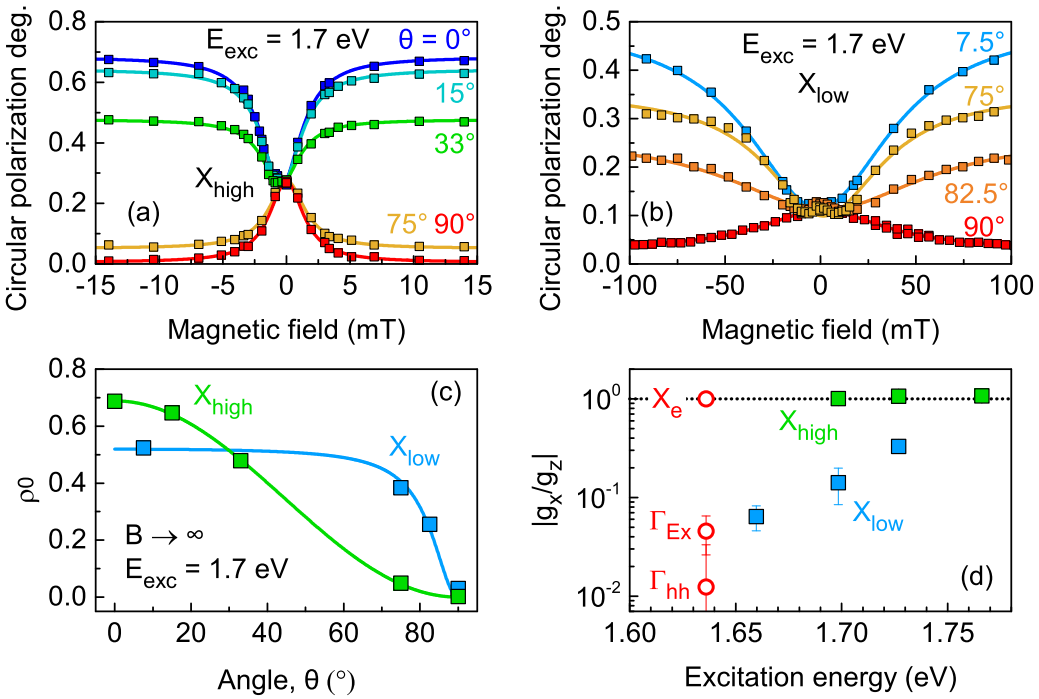

Figure 6.20: **(a)** and **(b)** Circular polarization degree of (a) X_{high} and (b) X_{low} excitons in dependence of the magnetic field strength B for different angles θ between B and z. Colored lines show Lorentz functions fitted to the data sets. **(c)** High field limit ρ_0 of the circular polarization degree in dependence of the angle θ for X_{high} (green) and X_{low} excitons (blue). Values are taken from the Lorentz functions in (a) and (b). The colored lines show Eq. (6.12) fitted to the data points with the parameters $g_x/g_z = 1.01$ (X_{high}) and $g_x/g_z = 0.14$ (X_{low}). **(d)** g-factor anisotropy g_x/g_z in dependence of the excitation energy. Results for the X_{high} (green) and the X_{low} excitons (blue) are compared with literature values from Tab. 6.2 (red circles) for the X electron (X_{e}), the direct exciton (Γ_{Ex}), and the heavy hole (Γ_{hh}). The dotted, horizontal line marks the isotropic g factor with $g_x/g_z = 1$.

state [18].

For the experimental determination, the circular polarization degree of the indirect exciton PL is measured in dependence of strength and angle of the external magnetic field. The measurements are repeated for different excitation and detection energies, which address the X_{high} and the X_{low} excitons.

Figure 6.20 (a) shows the results for the X_{high} excitons, excited with $E_{\mathrm{exc}} = 1.7$ eV. The angle θ between the z axis and the magnetic field B is indicated by the color. In case of $\theta = 0°$(blue) and $\theta = 90°$(red), the polarization curves are equal the PRC and the Hanle curve in Fig. 6.17 (a). For tilted fields in between, the high-field limit ρ_0 of the polarization degree is decreasing from 69% to zero with increasing angle θ. From the results for $\theta = 15°$(cyan) and $\theta = 75°$(yellow) it can be suspected, that the circular polarization degree is independent from the magnetic field for $\theta = 45°$. The field dependencies of the data points (squares) for the different angles are well described by Lorentz functions (colored lines) with an average HWHM of $B_{1/2} = (1.76 \pm 0.04)$ mT.

	Γ_{hh} [29]	Γ_{e} [47]	Γ_{Ex}	X_{e} [29]	X_{Ex} [29]
g_x	0.03 ± 0.05	0.15 ± 0.01	-0.12 ± 0.05	2.00 ± 0.01	-1.95 ± 0.08
g_z	2.42 ± 0.05	-0.05 ± 0.01	2.47 ± 0.05	2.00 ± 0.01	0.43 ± 0.08
$\lvert g_x/g_z \rvert$	0.01 ± 0.02	3.00 ± 0.06	0.05 ± 0.02	1.00 ± 0.01	4.53 ± 0.86

Table 6.2: Transverse and longitudinal g factors g_x and g_z and the calculated g-factor anisotropy $|g_x/g_z|$ of heavy holes (hh) and electrons (e) located in the Γ or X valley of the (In,Al)As/AlAs QDs. The g factors of the direct exciton Γ_{Ex} are calculated via $g(\Gamma_{\mathrm{Ex}}) = g(\Gamma_{\mathrm{hh}}) - g(\Gamma_{\mathrm{e}})$, while the values for the indirect exciton X_{Ex} are taken from literature. The values from Ref. [29] were determined for $E_{\mathrm{exc}} = 1.636$ eV. The values from Ref. [47] are estimated for $E_{\mathrm{exc}} = 1.640$ eV.

The results for the X_{low} excitons, excited with the same energy, are given in Fig. 6.20 (b). It can be seen, that the average HWHM $B_{1/2} = (46 \pm 11)$ mT of the polarization curves is much broader than for the X_{high} excitons in (a). Moreover, the high-field limit ρ_0 of the polarization degree is decreasing only for very high θ.
The angle dependencies of ρ_0 for the X_{low} (blue) and the X_{high} excitons (green) are given in Fig. 6.20 (c). The values are taken from the Lorentz functions shown in (a) and (b). For X_{high} it can be seen that the dependence is similar to the cos function, while the dependence is highly asymmetric for X_{low}. The colored lines represent the equation

$$\rho_0 \sim \frac{\cos^2\theta}{\cos^2\theta + (g_x/g_z)^2 \sin^2\theta}, \tag{6.12}$$

taken from Ref. [112], which is fitted to the data points with the fitting parameter $g_x/g_z = 1.01$ for X_{high} and $g_x/g_z = 0.14$ for X_{low}. Here, the parameter g_x/g_z is the ratio between the transverse and the longitudinal g factor of the carrier. The application of this equation is justified later in this section.
In Fig. 6.20 (d), the fitting parameter g_x/g_z is plotted in dependence of the excitation energy. For the X_{high} excitons (green), measured with excitation energies between 1.70 and 1.77 eV, g_x/g_z is increasing slightly from 1.01 to 1.07 with an uncertainty of 0.02 each. However, these values can be described as constant in comparison with the results for the X_{low} excitons (blue). Here, g_x/g_z is increasing strongly from 0.06 ± 0.02 to 0.33 ± 0.04 when the excitation energy is increased from 1.66 to 1.73 eV. The red circles show the literature values $g_x/g_z = 1$ for the X electron (X_{e}), $g_x/g_z = 0.07$ for the direct exciton (Γ_{Ex}) and $g_x/g_z = 0.01$ for the heavy hole (Γ_{hh}), which are also given in Tab. 6.2. Since the relevant g factors were gained by spin-flip Raman scattering with an excitation energy of 1.636 eV, the literature values in 6.20 (d) are plotted at this energy.

Before discussing the results of Fig. 6.20, it is necessary to justify the applicability of Eq. (6.12) in the context described. In Ref. [112], the well known expression for the Hanle curve in tilted fields [67] is extended for the case of an anisotropic g factor. Equation (6.12) is the high field limit of this expression. Since nuclear fields are not considered, the extended equation (not shown here) is not suitable to describe the magnetic field dependence of the curves in Fig. 6.20 (a) and (b). However, for strong external fields, B_{N} becomes negligible and the dependence $\rho_0(\theta)$ is well described by Eq. (6.12).

As already indicated at the beginning of this section, the experimental results show that the circular polarization of the indirect X_{high} exciton is determined by the electron spin. This is reflected in the isotropic g factor, which is measured for X_{high} excitons, see green squares in Fig. 6.20 (d). It is assumed, that this effect is caused by the lack of electron-hole exchange interaction in indirect excitons.
The situation is less clear for the X_{low} excitons (blue squares), since g_x/g_z is not constant for different excitation energies. However, the slope of g_x/g_z with decreasing excitation energy is roughly in line with the literature values for the direct exciton Γ_{Ex} and the heavy hole (Γ_{hh}). Moreover, it should be noted that the decrease of the longitudinal heavy hole g factor $g_z(\Gamma_{\mathrm{hh}})$ with increasing excitation energy, and thus the increase of $g_x/g_z(\Gamma_{\mathrm{hh}})$ and $g_x/g_z(\Gamma_{\mathrm{Ex}})$, was already predicted in [29]. From the results in Sec. 6.3 it is known that the circular polarization degree of the X-exciton state is limited by the polarization of the Γ state. Thus, it is assumed that the strong g-factor anisotropy is a fingerprint of the preceding Γ state. In order to confirm this assumption, the polarization curves of X_{low} exciton are studied more detailed in the following section. Among other things, the reason for the large half width of these curves will be discussed.

6.5.4 Spin decoherence and hyperfine interaction in the Γ valley

In the previous section, it is demonstrated that the indirect X_{low} exciton exhibits a strong g-factor anisotropy, which indicates the impact of the primary, higher energetic Γ-exciton state. In this section, more thorough studies of the polarization curves will confirm that the polarization of the X_{low} exciton is mainly determined by effects during the lifetime of the Γ exciton state, which is limited by the relaxation time.

In order to investigate the magnetic field dependence of the circular polarization degree in more detail, Faraday and Voigt fields in the mT and the T range are applied. Examples of the polarization curves are shown in Fig. 6.21. In (a), the excitation energy is $E_{\mathrm{exc}} = 1.653$ eV and the X_{low} exciton is detected at $E = 1.636$ eV. In a strong longitudinal magnetic field the circular polarization degree increases from 5.5% at 0 T to 84% at 5 T. Around zero field, the circular polarization degree is measured in smaller steps, see inset. Between 0 and 140 mT it increases up to 11%. Due to this relatively sharp minimum around zero field, the combined data can not be described by a single Lorentz function. Instead, a combination of two Lorentz functions, with both centers at $B = 0$, is used to fit the data points (dashed and dotted curves). The cumulative curve is represented by the solid, dark blue line. The half widths and heights (H) of the two Lorentz curves are $B_{1/2} = (0.18 \pm 0.01)$ T and $H = 13\%$ for the turquoise curve and $B_{1/2} = (1.83 \pm 0.06)$ T and $H = 71\%$ for the magenta curve. The magenta curve shows a circular polarization degree of 19.5% for $B = 0$.
At certain energies, very narrow polarization curves, as shown for the X_{high} exciton in Fig. 6.20 (a), can also be observed for the X_{low} exciton. One example is shown in Fig. 6.21 (b). Here, the excitation energy is $E_{\mathrm{exc}} = 1.727$ eV and the PL peak of the X_{low} exciton is detected at $E = 1.669$ eV. The magnetic field dependence of the circular polarization degree is shown by the black squares for the case that the magnetic field is applied in approximate Faraday geometry ($\theta = 7.5°$) and by the black dots for exact Voigt geometry ($B \perp z$). Both polarization curves can be described by a wide and a narrow Lorentz function each with the centers at $B = 0$. The half widths, measured in approximate

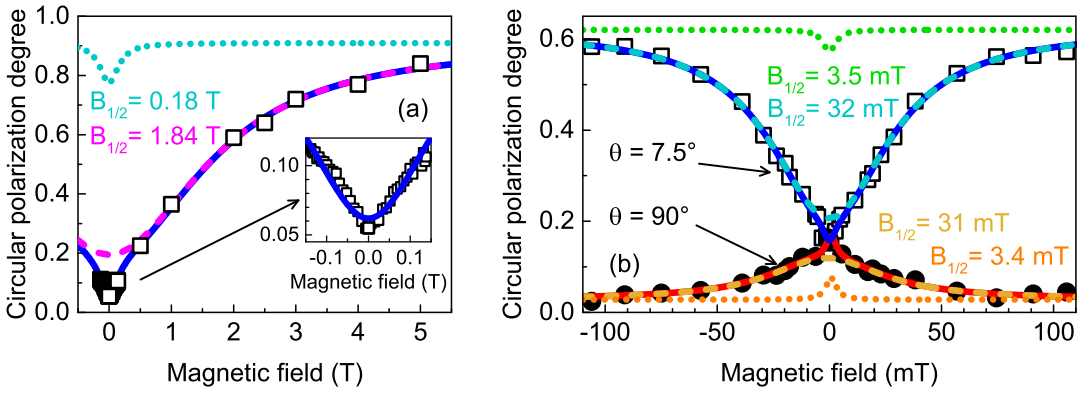

Figure 6.21: Circular polarization degree of the X_{low} exciton, measured for **(a)** $E_{\text{exc}} = 1.653$ eV and $E = 1.636$ eV in Faraday geometry ($B \parallel z$) and for **(b)** $E_{\text{exc}} = 1.727$ eV and $E = 1.669$ eV in 'close to' Faraday ($\theta = 7.5°$) and Voigt geometry ($\theta = 90°$). The dashed, colored lines show Lorentz curves that are fitted to the data points. The half widths $B_{1/2}$ are the respective fitting parameters. The cumulative curves are represented by the solid, red and dark blue lines. The inset of (a) shows a closeup of the area around zero field.

Faraday geometry, are $B_{1/2} = (32 \pm 2)$ mT (turquoise curve) and $B_{1/2} = (3.5 \pm 1.3)$ mT (green curve). In Voigt geometry, the half width are $B_{1/2} = (31 \pm 5)$ mT (yellow curve) and $B_{1/2} = (3.4 \pm 1.9)$ mT (orange curve). The heights of the two narrow curves (green and orange) are about 4.5% each, the heights of the wide curves (turquoise and yellow) are 41% in Faraday and 9% in Voigt geometry. The cumulative curves are represented by the red and dark blue solid lines.

All half widths, which are determined in Fig. 6.21, are plotted in Fig. 6.22 (a) together with further results for the X_{low} exciton (blue symbols) at different spectral energies. Moreover, half widths of polarization curves measured for the X_{high} exciton (green symbols) and for the direct exciton (red symbols) are given in the figure. Results, which were obtained in Faraday geometry, are marked with dots, results gained in Voigt geometry are marked with crosses.

The values of the half width are grouped in three different clusters: The three largest half widths of about 2 T were obtained for the direct excitons (red dots) and for the X_{low} excitons (blue dot) in Faraday geometry. They are assigned to cluster 1 and are constant for energies between 1.55 and 1.64 eV. In cluster 2, the half width decreases from 182 to 32 mT when spectral energy increases from 1.636 to 1.669 eV. These values were measured for the X_{low} excitons only. The lowest values, in cluster 3, are in the range of 1.5 mT. They are measured for X_{low} and X_{high} excitons. A local maximum with $B_{1/2} = 3.5$ mT is found for $E \approx E_{\Gamma X}^{\text{high}}$ (dashed green line). In cluster 2 and 3, the widths in Faraday (dots) and Voigt geometry (crosses) are about the same.

Figure 6.22 (b) shows the ratio of the heights H_2 and H_3 of composite polarization curves, which were measured for the X_{low} excitons in Voigt geometry. H_3 is the height of the narrow polarization curve from cluster 3 and H_2 is the height of the related, wider polarization curve from cluster 2. The ratio H_2/H_3 is decreasing with increasing spectral energy, which means that the height of the wide curve decreases in relation to the height

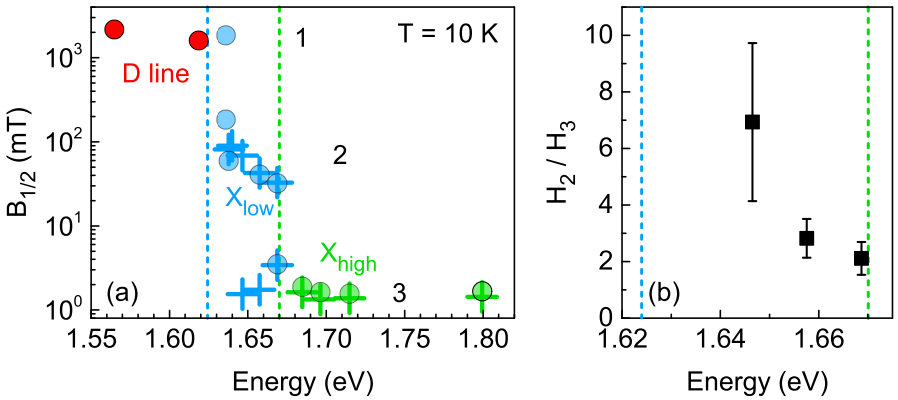

Figure 6.22: Properties of the polarization curves in dependence of the spectral energy: **(a)** Half widths $B_{1/2}$ measured in Faraday (circles) and Voigt geometry (crosses) for direct (D line, red) and indirect excitons (X_{low} and X_{high}, blue and green). Error bars are smaller than the symbol size. The numbers 1, 2 and 3 mark the three data clusters. **(b)** Ratio of the heights H_2 and H_3 of composite polarization curves, measured in Voigt geometry. The numbers 2 and 3 are related to the data clusters in (a). The dashed lines show the ΓX-transition energies $E_{\Gamma\mathrm{X}}^{\mathrm{low}}$ (blue) and $E_{\Gamma\mathrm{X}}^{\mathrm{high}}$ (green).

of the narrow curve.

The results presented in Fig. 6.22 (a) indicate that the spin polarization of the X_{low} exciton (blue) is determined by three different effects. These effects lead to different magnetic field dependencies of the circular polarization degree, characterized by the half widths $B_{1/2}$, which vary between three orders of magnitudes.
First, the situation in small magnetic fields (cluster 3) should be discussed. For $E \approx 1.65$ eV, it is possible to observe narrow polarization curves (blue symbols), which show the same half widths as the curves measured for the X_{high} exciton (green symbols). The polarization curves of the X_{high} exciton are the result of counteracting the nuclear field B_{N} with an external magnetic field. A characteristic feature of the hyperfine interaction is that the polarization curves, measured in Faraday and Voigt geometry, show the same half widths, see Sec. 6.5.1. This is demonstrated for the X_{low} exciton with the spectral energy of $E = 1.669$ eV, see Figs. 6.21 (b) and 6.22 (a). It is known from the sections above that the hyperfine interaction of the X_{high} exciton is mediated by the X electron. Therefore, it is no surprise that this effect is observed for both indirect exciton types X_{low} and X_{high}.

Next, the behavior of the X-exciton polarization in high magnetic fields (cluster 1) should be explained. Since the recombination time of the X excitons is much shorter than the spin relaxation time, ($\tau_{\mathrm{s}}/\tau_{\mathrm{r}} > 36$, see end of Sec. 6.5.1), magnetic field induced polarization should be negligible. Therefore, the increase of the circular polarization degree in a strong, longitudinal magnetic field, as demonstrated in Fig. 6.21 (a) for the X_{low} exciton, was not expected. However, this finding can be explained by the influence of the Γ-valley exciton on the polarization degree of the X_{low} exciton. It is shown in Sec. 6.3 that the circular polarization degree of the indirect exciton is limited by the circular

polarization degree of the direct exciton state, since the electron is relaxing from the Γ to the X valley of the conduction band. It is further shown in Sec. 6.4 that the circular polarization of the direct exciton can be increased strongly by applying a longitudinal magnetic field ($B \parallel z$). (This is based on the fact that the Zeeman splitting exceeds the anisotropic exchange splitting of the Γ-exciton spin states.) The related half widths of the polarization curves are in the range of 2 T. They are given in Fig. 6.22 (a) by the red dots. These values are comparable to the half width of 1.8 T, measured for the indirect exciton X_{low} (blue dot). Therefore, it is concluded for the X exciton that the longitudinal magnetic field dependence of the circular polarization degree is largely determined by the spin decoherence in the Γ state.

Finally, the polarization curves of the X_{low} excitons with intermediate half widths (cluster 2) should be discussed. Since the half widths are the same for Faraday and Voigt geometry, it can be concluded that the hyperfine interaction is determining the magnetic field dependence of the circular polarization degree here, see Sec. 6.5.1. Previous findings indicate that the polarization of the X_{low} exciton is strongly determined by the polarization of the Γ-exciton state. Thus, it is assumed that the hyperfine interaction of the Γ electron with the nuclei is responsible for these intermediate polarization curves. In the following, two arguments are presented to support this assumption:
1) In Figs. 6.21 (a) and (b) the turquoise polarization curves, measured in Faraday geometry, are assigned to cluster 2. The ratio $\rho_0/\rho_z(0)$ of these curves is $0.192/0.062 = 3.1$ in (a) and $0.620/0.206 = 3.0$ in (b). It is known, that $\rho_0/\rho_z(0) = 3$ is characteristic for isotropic hyperfine interaction [22] and that the hyperfine interaction in the Γ valley is isotropic. Therefore, it can be concluded, that the polarization curves with intermediate half widths are the result of the hyperfine interaction between the nuclei and the Γ electron.
2) Now the strongly different half widths of the polarization curves in cluster 2 and 3, $B_{1/2}^{(2)}$ and $B_{1/2}^{(3)}$, will be related to the different properties of the X- and the Γ-valley electrons. For $E(X_{\mathrm{low}}) = 1.647$ eV the ratio is $B_{1/2}^{(2)}/B_{1/2}^{(3)} = 44$, see Fig. 6.22 (a). As the polarization curves are determined by the hyperfine interaction, the half width $B_{1/2}$ of the Hanle curve is equal to $2\varepsilon B_{\mathrm{N}}$, see Eq. (2.50). From Eq. (2.46) it is known that the strength of the nuclear field B_{N}, along the axis of the respective valley, depends on the hyperfine coupling constant $A_{\mathrm{As}}^{\parallel}$ (A in the following), the nuclear spin I, the Volume V_0 of the primitive cell, the QD Volume V and the g factor along the axis. Furthermore, it is known from the results of Sec. 6.5.2 that the X electrons are located in the X_x or the X_y valley of the conduction band. Thus, the relevant g factor, along the X valley axis, is $g_x = g_y$ (g_x in the following). The wave function of the Γ electron has no preferred direction. For the polarization curves of X and Γ electrons, excited by the same excitation energy, the ratio of the half widths is given by

$$\frac{B_{1/2}^{(\Gamma)}}{B_{1/2}^{(X)}} = \frac{g_x^{(X)}}{g_x^{(\Gamma)}} \frac{\varepsilon^{(\Gamma)}}{\varepsilon^{(X)}} \frac{A^{(\Gamma)}}{A^{(X)}}, \tag{6.13}$$

since I, V_0 and V are material properties, which are equivalent for the same excitation energy. For the X electron it is $g_x^{(X)} = 2$, see Tab. 6.2. In Sec. 6.5.1, $\varepsilon^{(X)}$ is determined to 0.64 and $A^{(X)}$ is calculated to 10.4 μeV. For the Γ electron, excited with

$E_{\mathrm{exc}} = 1.675$ eV, it is $g_x^{(\Gamma)} = 0.25$ [47]. Furthermore it is $\varepsilon^{(\Gamma)} = 1$ and $A^{(\Gamma)} = 43.5$ μeV [63]. Thus, it follows $B_{1/2}^{(\Gamma)}/B_{1/2}^{(X)} = 52$, which is comparable to the experimental value $B_{1/2}^{(2)}/B_{1/2}^{(3)} = 44$, see above.

The two presented arguments support the assumption, that the polarization curves with intermediate half width (Fig. 6.22 (a), cluster 2) are determined by the hyperfine interaction of the electron in the Γ valley before it relaxes to the X valley. However, for the effective depolarization of the electron spin it is necessary that the electron remains in the Γ valley for a sufficiently long time. It is known from Sec. 6.3 that the relaxation time of the electrons from the Γ to the X valley is increasing with decreasing distance $\Delta E_{\Gamma X}$ between these two valleys. If the relaxation time is longer than the Larmor precession period Ω^{-1} of the Γ-electron spin around the nuclear field, the circular polarization degree decreases already before the electron relaxes to the X valley. If the relaxation time is shorter than Ω^{-1}, the transverse nuclear field components can not fully depolarize the electron spin and the impact of the Γ valley decreases.

To quantify these considerations, the Larmor precession period $\Omega^{-1} = \hbar/(|g_{\mathrm{e}}|\mu_{\mathrm{B}}B_{\mathrm{N}})$ is calculated for the exciton energy $E(X_{\mathrm{low}}) = 1.647$ eV, which is in the center of cluster 2. The related excitation energy is $E_{\mathrm{exc}} = 1.675$ eV and the g factor of the Γ electron for this energy is $g_{\mathrm{e}} = 0.25$ [47]. The strength of the nuclear field can be determined via Eq. (2.50) to $B_{\mathrm{N}} = B_{1/2}/(2\varepsilon)$, where $B_{1/2}$ is the half width of the Hanle curve. Since the wave functions of the Γ electron are of s type, the hyperfine interaction is isotropic ($\varepsilon = 1$). With $B_{1/2} = (68 \pm 4)$ mT it is $\Omega^{-1} = (1.3 \pm 0.1)$ ns. It follows, that the relaxation time τ_{relax} must be at least 1.3 ns at this exciton energy. This value seems to be high in comparison with usual relaxation times in QDs, which are in the range of picoseconds [113]. However, it should be recalled that the relaxation of the electron from the Γ to the X valley is not attained by the sole emission of energy but it requires also a change in momentum space, e.g. by phonon scattering or scattering at the QD edges. The results from Sec. 6.3.2 show, that the relaxation time is increased especially for excitation energies with $\Delta E_{\Gamma X} < 30$ meV, where the energy difference is smaller than the LO phonon energy.

The spectral dependence of the relaxation time can also explain the decrease of the ratio H_2/H_3, which is shown in Fig. 6.22 (b). For high exciton energies, the energy difference $\Delta E_{\Gamma X}$ is increased and the relaxation from the Γ to the X valley accelerates. When the relaxation time becomes faster than Ω^{-1}, which is in the range of 1 ns, the nuclei can not fully depolarize the Γ-electron spin. This leads to the decrease of H_2, which is assigned to the hyperfine interaction of the Γ electron. This is in line with the fact that for excitation energies higher than 1.727 eV ($E > 1.669$ eV), it becomes difficult to detect further polarization curves that can be assigned to the hyperfine interaction in the Γ valley (cluster 2).

Now, further features in Fig. 6.22 (a) are discussed. It can be seen, that the half widths of the polarization curves, which are caused by hyperfine interaction, (cluster 2 and 3) depend on the (excitation) energy. For cluster 2, a strong decrease by a factor of 5.5 is observed in the energy range between 1.636 eV and 1.669 eV, which corresponds to excitation energies between 1.653 eV and 1.727 eV. According to Eq. (2.50), the half width of the polarization curves is proportional to the strength of the nuclear field, which in turn is proportional to the reciprocal g factor g_x of the Γ electron, see Eq. (2.46). Indeed, it is shown in Ref. [47] that the transverse g factor of the Γ electron increases

from 0.20 to 0.38 in the considered energy range. However, as the factor $0.38/0.20 = 1.9$ is clearly smaller than 5.5, it is assumed that a second, unknown effect causes further decrease of $B_{1/2}$.
In cluster 3, a local maximum of the half width $B_{1/2}$ is observed for the X_{low} exciton at $E = 1.669$ eV. This energy is equal to the ΓX-transition energy $E_{\Gamma X}^{\mathrm{high}}$ (dashed green line). Therefore, the increase might be explained by a reabsorption process, in which the PL of the X_{low} exciton, excited with $E_{\mathrm{exc}} = 1.727$ eV, excites the mixed states of Γ and X_{high} electron in a larger QD. In this way a fraction of X electrons is converted to Γ electrons, which show a wider polarization curve. Since the probability of reabsorption is expected to be low, the fraction of Γ electrons is small and the increase of $B_{1/2}$ is weak.

In conclusion, it is demonstrated that the circular polarization degree of the indirect X_{low} exciton is determined by the hyperfine interaction of the Γ electron with the nuclei before the exciton relaxes to the X state. In addition, the circular polarization degree of the X_{low} exciton is reduced due to the short decoherence time of the linearly polarized Γ states. The hyperfine interaction of the X electron plays a relatively small role for the polarization of the X_{low} exciton, which is in contrast to the X_{high} exciton. All three effects can be counteracted in a sufficiently high Faraday field.

6.5.5 Conclusion

Now, the findings of this section are summarized. As it is mentioned at the beginning (p. 82), the circular polarization degree is actually the optical orientation degree under the present conditions. The optical orientation degree of the X exciton can be reduced by four different effects, which are presented schematically in Fig. 6.23. Already in the Γ valley the exciton spin can be depolarized 1.) due to the short decoherence time of the linearly polarized exciton levels, see Sec. 6.3, and 2.) due to the hyperfine interaction with the nuclei, see Sec. 6.5.4. After the relaxation, the electron spin is additionally depolarized by 3.) the hyperfine interaction in the X valley, see Sec. 6.5.1. By applying a longitudinal magnetic field it is possible to counteract these effects. In case of a large energy difference $\Delta E_{\Gamma X}$ between the Γ and the X valley, the optical orientation degree of the electron is reduced by 0.) the scattering during the energy relaxation. This effect is independent from the magnetic field strength. In principle, all four effects can occur during the lifetime of the exciton. In (a), the values ρ_{i}, ρ_{d}, ρ_{Γ} and ρ_X indicate the reduced optical orientation degree due to initial losses, decoherence, hyperfine interaction of the Γ electron and hyperfine interaction of the X electron respectively.
The impact of these effects on the optical orientation degree is determined by the ΓX splitting $\Delta E_{\Gamma X}$, which depends on the exciton energy. This dependence is shown in Fig. 6.23 (b). By plotting ρ_{i} (orange), ρ_{d} (red), ρ_{Γ} (blue) and ρ_X (green) in dependence of E it is possible to create a 'polarization map' for the (In,Al)As/AlAs QD ensemble. The ΓX-transition energies are shown by the two grey dots on the energy scale. For direct excitons with $E < E_{\Gamma X}^{\mathrm{low}}$ (left grey dot), the recombination time of the Γ exciton is longer than the decoherence time, thus the optical orientation is strongly reduced. For indirect excitons with $E > E_{\Gamma X}^{\mathrm{low}}$, ρ_{d} and ρ_{Γ} are increasing with increasing energy, which means that the impact of decoherence and hyperfine interaction in the Γ valley is decreasing. This can be explained by the reduction of the average time the electron remains in the Γ valley, see Sec. 6.3.2. These two effects can be neglected for energies higher than

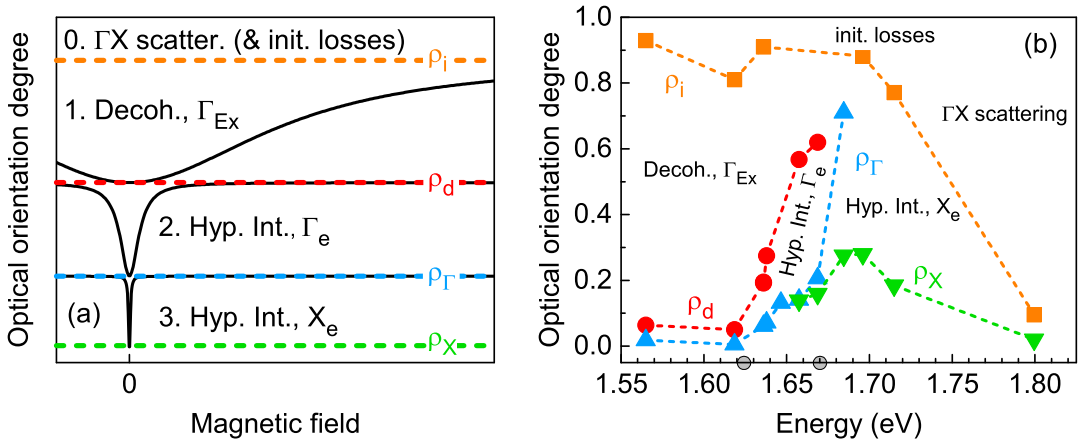

Figure 6.23: **(a)** Schematic presentation of three different PRCs (black lines) of excitons in indirect (In,Al)As/AlAs QDs, $B \parallel z$. The polarization curves are caused by counteracting (1.) the decoherence of the Γ exciton spin, (2.) the hyperfine interaction of the Γ electron and (3.) the hyperfine interaction of the X electron. (0.) Field independent depolarization due to ΓX scattering. The dashed, colored lines mark the zero-field limits ρ_i, ρ_d, ρ_Γ and ρ_X of the curves. **(b)** Optical orientation degrees ρ_i (orange), ρ_d (red), ρ_Γ (blue) and ρ_X (green), in dependence of the exciton energy. Dashed lines are guides for the eye. The reason for the decrease of the optical orientation degree from the upper to the lower value is given in respective area in between. The grey dots on the energy scale mark the ΓX-transition energies $E_{\Gamma X}^\mathrm{low} = 1.624$ eV and $E_{\Gamma X}^\mathrm{high} = 1.670$ eV.

1.69 eV. Instead, the upper limit of the optical orientation degree is strongly reduced by the scattering process from the Γ to the X valley (ρ_i) in this high-energy range. At the same time, the (relative) distance between ρ_X and the other values starts to increase, as the recombination time of the X exciton is increasing significantly above the Larmor precession time, which leads to the effective depolarization of the electron spin via hyperfine interaction, see section 6.5.2.

In conclusion, by determining the magnetic field dependence of the optical orientation degree, it is possible to distinguish between four different effects, which lead to the depolarization of the exciton spin in the (In,Al)As/AlAs QDs. Impact and magnetic field dependence of the respective effects change strongly with $\Delta E_{\Gamma X}$ and thus the energy range under consideration. The highest optical orientation degree of about 30% in zero field is measured for an exciton energy of $E \approx 1.69$ eV. By applying a small, longitudinal magnetic field of several mT the optical orientation degree can easily be increased up to 88% at this energy. At lower energies, the necessary field clearly exceeds 2 T and at higher energies, the maximum polarization is strongly reduced by losses during the energy relaxation. Therefore, it should be stressed once again that the ΓX splitting $\Delta E_{\Gamma X}$ is of decisive importance for the optical orientation degree in indirect QDs. This knowledge might be useful for the development of tailored QD samples.

6.6 (Spin) Dynamics under selective excitation

One of the main reasons for the investigation of QDs with an indirect band gap in momentum space is the long spin lifetime T_s, which is determined by the exciton recombination time τ_r and the spin relaxation time τ_s. Therefore, it is interesting to measure these times and study their dependencies from several parameters like magnetic field strength, temperature and size of the QDs.
In Sec. 6.2 and several previous works ([39], [28], [29]), the recombination times of direct and indirect excitons are studied under nonresonant conditions. Moreover, it is possible to determined the spin relaxation time τ_s under nonresonant excitation by the time-resolved measurement of the magnetic field induced polarization, which sets in for $t > \tau_s$. These experiments are presented in Ref. [88] for a sample that is similar to the samples studied in this thesis. However, the simultaneous excitation of the whole QD ensemble leads to the spectral overlap of various, partly unknown, PL features, see Secs. 6.1.1 and 6.2.1. This makes it difficult to clearly determine the characteristic times of the indirect excitons. Another aim is the temporal separation of the spectrally overlapping Γ exciton emission and the laser signal, which is only possible under resonant (selective) excitation.
The solution lies in the selective, pulsed excitation of the QDs and the time-resolved detection of their PL. This requires a pulsed laser with tunable output wavelength. The used laser system and the setup are described in Sec. 3.3, while the main challenges with the experiment are presented in Sec. 6.6.1. First results are presented and discussed in Sec. 6.6.2. The studied sample is AG 2890.

6.6.1 Experimental details and difficulties

For the correct analysis of the PL signal, two aspects of the used laser and fiber have to be considered, which are explained with the help of Fig. 6.24.
1.) Laser: As it can be seen in Fig. 6.24 (a), the intensity of the laser is not zero between two pulses. The 'off'-phase signal is about 7 orders of magnitudes smaller than the intensity of the main pulse and the reflected laser light is comparable to the intensity of the PL of the X excitons, see 6.24 (b). Two problems can arise from this fact. On the one hand, the polarized background excitation can, in principle, distort the spin dynamic measurement, especially for very long decay times. This would lead to another increase of the optical orientation degree. However, model calculations (not shown here) indicate that this increase does not disturb the determination of the spin relaxation time. On the other hand, it can be seen in (b) that the Γ exciton PL at the spectral position of the laser line is not detectable in the time integrated configuration. Therefore, it can be concluded that the temporal separation of the direct signal and the laser line is experimentally challenging. It might be possible with very long accumulation times and a high temporal resolution below 1 ns. However, the study of the (zero phonon) Γ line is beyond the scope of this thesis.
2.) Fiber: At $t = 464$ ns, a second pulse is observed in (a), which is 5 orders of magnitude smaller than the main pulse at $t = 3$ ns but also two orders of magnitude higher than the signal during the 'off' phase of the laser. The time of 464 ns is in good agreement with 500 ns, which is the time the light needs to pass through the 50 m long fiber twice, when the speed of light in the fiber is $2 \cdot 10^8$ m/s. Therefore, it can be concluded that

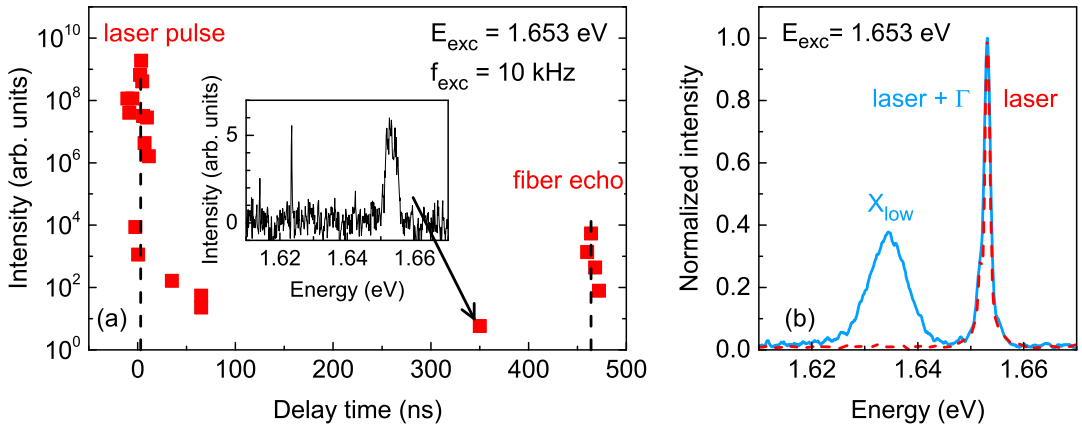

Figure 6.24: **(a)** Temporal development of the laser intensity (red squares). The laser beam is emitted by a picosecond OPA and guided to the setup by a 50 m long fiber. The laser energy is $E_{\mathrm{exc}} = 1.653$ eV and the repetition rate is 10 kHz. The dashed lines mark the time of the main pulse at $t = 3$ ns and the time of the fiber echo at $t = 464$ ns. The inset shows the signal during the 'off' phase of the laser. **(b)** Time integrated spectra of the laser signal (red), reflected form a black paper, and the sample signal (blue) with PL emission from the X_{low} exciton. PL from the Γ exciton is not visible.

the second peak is the reflection of the main laser pulse at the exit of the fiber, the 'fiber echo'. In principle, the fiber echo can cause additional PL and polarization, which might lead to misinterpretation of the data. In the studied case, the fiber echo is much smaller than the main pulse and can probably be neglected. However, the intensity losses in the fiber might scale with the wavelength of the laser light or properties of the fiber. Thus, this source of error should not be disregarded.
The main technical challenge is the low PL intensity of the X excitons, since selective excitation addresses only a small fraction of QDs in the ensemble. In addition, an adequate temporal resolution requires the limitation of the exposure time. Especially for long delay times after the laser pulse, when the optical orientation is decreasing, very high accumulation times are necessary to measure the small intensity differences for the two polarization directions. These long measurement times make the experiment more sensitive to unintentional changes in slowly fluctuating parameters such as temperature, laser power or background intensity.

6.6.2 Recombination and spin relaxation of the X exciton

Figure 6.25 (a) shows the temporal development of the PL intensity (dark blue squares) and the optical orientation degree (red circles), measured for the X_{low} exciton with $E = 1.636$ eV. The excitation energy is $E_{\mathrm{exc}} = 1.653$ eV, the longitudinal magnetic field is $B = 5$ T and the temperature is $T = 1.8$ K. Here, the decrease of the PL intensity can be described by an exponential decay (dark blue line) with the fitting parameter $\tau_{\mathrm{r}} = (100 \pm 14)$ ns, which is assigned as exciton recombination time. The optical orientation degree remains constant at about 80% up to 1000 ns. Its decrease can be described by an exponential decay (red line) with the fitting parameter $\tau_{\mathrm{s}} = (5 \pm 1)$ μs, which is assigned to the spin relaxation time.

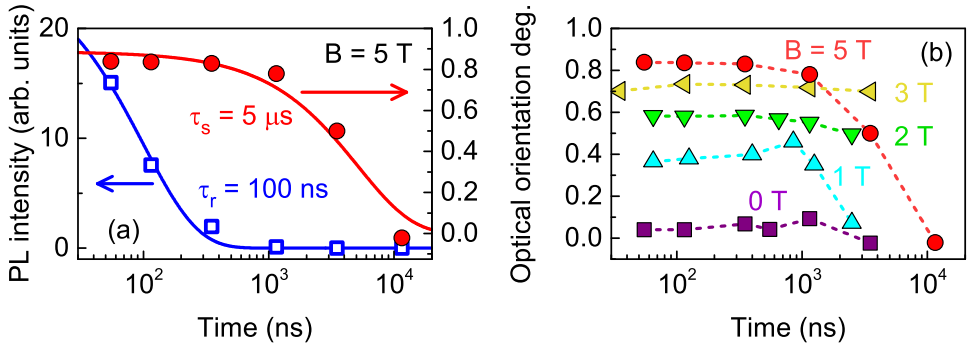

Figure 6.25: Dynamics of the X_{low} exciton with $E_{\mathrm{exc}} = 1.653$ eV and $E = 1.636$ eV: **(a)** PL intensity (dark blue squares) and the optical orientation degree (red dots) measured at $B = 5$ T ($B \parallel z$). τ_{r} and τ_{s} are the fitting parameters of the exponential functions (colored lines). **(b)** Optical orientation degree measured for different magnetic fields $B \parallel z$ between 0 and 5 T. Dashed lines are guides for the eye. $T = 1.8$ K.

When the magnetic field strength is decreased, the optical orientation degree is decreasing down to 4% at zero Tesla. This is shown in Fig. 6.25 (b). Due to the low PL intensity it was not always possible to observe the full decay of the optical orientation. However, from the slope of the curves it can be assumed, that the highest spin relaxation time can be found between 2 and 3 T.

The main results of Fig. 6.25 can be explained by the findings of the previous chapters. The exciton recombination time of the X_{low} exciton, $\tau_{\mathrm{r}} = 100$ ns, at $T = 1.8$ K is much longer than 4.5 ns, the value which is determined for the same emission energy at $T = 2.6$ K, see Sec. 6.2.1. Two reasons might cause the strong difference. On the one hand, it is possible that under nonresonant excitation the recombination time is reduced by the contribution of PL sources other than the indirect excitons. On the other hand, the recombination process is strongly temperature dependent at low temperatures. In Sec. 6.2.2, this behavior is attributed to the thermal activation of excitons from the dark to the bright state. The increase of τ_{r} with decreasing temperature (from 2.6 to 1.8 K) is in line with this model.
Due to the high optical orientation of the exciton spin, measured for the X excitons (Sec. 6.5.1) in a small magnetic field, it was already expected that the spin relaxation time τ_{s} is at least 36 times longer than the recombination time τ_{r}. In the studied case τ_{s} is 50 times longer than τ_{r}. The increase of the maximum optical orientation degree of the X_{low} exciton in a longitudinal magnetic field, see (b), is caused by the increase of the optical orientation degree of the preceding Γ state, which is presented in Sec. 6.4.1. This topic is also discussed in Secs. 6.3.2 and 6.5.4.
The spin relaxation time of $\tau_{\mathrm{s}} = 5$ μs for $B = 5$ T and $E = 1.636$ eV is about 10 times shorter than the value, which was gained in Ref. [88] under nonresonant excitation of a similar sample with $B = 5$ T and $E = 1.83$ eV. In this reference, the decrease of the spin relaxation time with increasing magnetic field strength, for $B > 4$ T, is attributed to acoustic phonon scattering that mediate the spin-flips. Here, a decrease of τ_{s} is observed between 3 and 5 T, see Fig. 6.25 (b), while τ_{s} seems to increase between 0 and 3 T. This increase can be explained by the Zeeman splitting of the degenerated exciton

states, which is discussed in the following.
The situation for the indirect QD excitons in a longitudinal magnetic field is comparable to the one for the indirect GaAs-QW excitons, since the relation between the longitudinal g factors of electrons and holes are the same for the two structures: $g_\mathrm{h} > g_\mathrm{e} > 0$. Therefore, the fine-structure splitting and the spin-flip rates can be described by the scheme in Fig. 5.3. However, under selective and circularly polarized excitation the generation of excitons occurs only in the respective bright energy level. The application of the kinetic spin model (Sec. 2.4.1) to the spin dynamics of the indirect QD excitons is beyond the scope of this thesis and would require more thorough measurements. Therefore, the following discussion is of qualitative nature.
Due to the lack of electron-hole exchange interaction, the indirect exciton states are degenerated in absence of an magnetic field. A longitudinal field splits them by the Zeeman energy ΔE_Z. The spin relaxation rate $w_\mathrm{s} = \tau_\mathrm{s}^{-1}$ of the exciton is given by the sum of the two spin flip rates to the upper an the lower spin level. In case of σ^+ polarized light, the created exciton can go to the higher energetic dark state via an electron spin flip or to the lower energetic dark state via a hole spin flip, see Fig. 5.3 (a) and (b). Thus the spin relaxation rate of the exciton is given by

$$w_\mathrm{s} = w_\mathrm{s,down} + w_\mathrm{s,up} = w_\mathrm{h} + \alpha w_\mathrm{e}, \tag{6.14}$$

where the electron spin-flip rate to the upper level is proportional to the Boltzmann factor α, see Eq. (2.23). For simplification it is assumed that the spin relaxation rates of electron and hole are equal ($w_\mathrm{e} = w_\mathrm{h}$). Then, the spin relaxation time of the exciton is given by

$$\tau_\mathrm{s}(B) = \frac{\tau_\mathrm{s,e}}{1 + \exp\left(\frac{-g_\mathrm{e}\mu_\mathrm{B}B}{k_\mathrm{B}T}\right)}, \tag{6.15}$$

and describes also the case of σ^- polarized excitation (with g_h instead of g_e). If the spin-flip rates of electron and hole differ from one another ($w_\mathrm{e} \neq w_\mathrm{h}$), $\tau_\mathrm{s}(B)$ depends form the polarization of the excitation (σ^+ or σ^-) and is described by two different equations. However, the quantitative outcome is the same. For $B = 0$, Eq. (6.15) is $\tau_\mathrm{s} = \tau_\mathrm{s,e}/2$ and for $B \to \infty$, it is $\tau_\mathrm{s} = \tau_\mathrm{s,e}$. Thus, the spin relaxation time increases with increasing field strength, as it is observed experimentally in Fig. 6.25 (b) for 0 T $< B <$ 3 T.
For sufficiently high field strength, the splitting of the Zeeman levels overcomes the thermal energy of the electrons and the spin relaxation time approaches $\tau_\mathrm{s,e}$. With $g_\mathrm{e} = 2$ and $T = 2$ K it is $g_\mathrm{e}\mu_\mathrm{B}B > 3/2k_\mathrm{B}T$ for $B > 2.2$ T. Above this field strength, Eq. (6.15) depends only weakly from B and a stronger effect with opposite field dependence starts to dominate τ_s. This is the acceleration of the exciton spin-flip rate by acoustic phonon scattering with a $\tau_\mathrm{s} \propto B^{-5}$ dependence [92], which was already mentioned above. Thus, the maximum of τ_s, which is indicated in Fig. 6.25 (b) for 2 T $< B <$ 3 T, is explained by the occurrence of the two effects described.

6.6.3 Conclusion

In conclusion, it was possible for the first time to measure the recombination and spin relaxation times of indirect excitons under selective excitation. With this technique, the falsification of the results due to nonresonant PL contributions (see Sec. 6.1.1) can be

excluded. For a longitudinal magnetic field strength of $B_z = 5$ T, the spin relaxation time is 5 μs and the recombination time is 100 ns. The nonmonotonic dependence from the field strength is explained by the interplay of two different effects. On the one hand, the increasing distance between the Zeeman levels reduces the spin flip rates of electron an holes to the high energetic dark exciton state, which leads to the increase of the exciton spin relaxation time. On the other hand, the decrease in spin relaxation time in a longitudinal magnetic field is typical of exciton spin flips that are mediated by acoustic phonon scattering.

The presented measurements show only a small part of the possibilities this experimental method offers. Due to the small PL intensities under selective excitation, the time-resolved measurement of the optical orientation degree is technically challenging and requires further improvements of the setup. However, more thorough measurements may allow the application of the kinetic spin model (Sec. 2.4), which could reveal the spin relaxation times of electrons and holes in indirect QDs. Moreover, the role of dynamical nuclear polarization, which can be important already on timescales exceeding tens of nanoseconds [22], is still unclear.

7 Conclusions

In this thesis it is demonstrated for the first time in experiments (to the best of the author's knowledge) that the electron-hole exchange interaction is suppressed for excitons in (type-I) semiconductors with an indirect band gap in momentum space. This effect was predicted theoretically for bulk excitons by G. E. Pikus and G. L. Bir in 1971.
The suppression of the electron-hole exchange interaction is observed in different fine-structure experiments like the evidence of optical orientation or the direct measurement of the anisotropic exchange splitting. Related effects on the spin dynamics are studied for two different heterostructures, a type-II GaAs/AlAs QW and an (In,Al)As/AlAs QD ensemble. The spin polarization of the indirect excitons in the samples is strongly affected by the suppression, since the four X exciton spin states, $|\pm 1\rangle$ and $|\pm 2\rangle$, are fully degenerated in absence of the exchange splitting. Splitting and mixing of the states occurs only in external magnetic fields and can be controlled by its strength and direction. However, a fundamental difference between the two studied structures is the ratio of the spin relaxation and the exciton recombination time. As a result, different polarization effects are observed:

For the ultrathin QW with type-II alignment, the exciton recombination is much slower than the spin relaxation. As a result, the spin dynamics between dark and bright exciton levels has a strong effect on the polarization degree, which is reflected in its nonmonotonic dependencies on magnetic field and temperature. The spin dynamics is governed by the relations of the g factor tensor components of electron and hole, since these relations define the order of the exciton Zeeman states and the magnitudes of their splittings. Moreover, the g factors determine the spin-flip rates of electron and hole from lower to higher energetic exciton states, which causes the nonmonotonic temperature and field dependencies of the circular polarization degree. The comparison of the experimental results and the kinetic spin model yields the heavy-hole g factor and the spin relaxation time of the X electron.
The C_{2v} symmetry of the QW leads to the mixing of heavy hole and light hole states, which is reflected in the activation of the dark states. The mixing of heavy and light hole states also leads to an intrinsic linear polarization of the QW exciton and a finite transverse g factor of the hole, which are determined by the comparison with the kinetic spin model. A small supplement to this model is made, which enables a better understanding of the spin dynamics and reveals the relation between important sample parameters and the characteristic field strength at which the circular polarization degree reaches its maximum.

For the indirect (In,Al)As/AlAs QD excitons, the spin relaxation time clearly exceeds the exciton recombination time. This enables the observation of optical orientation and the study the associated depolarization mechanisms, like the hyperfine interaction between the X electron and the nuclei. The investigation of the QD ensemble, with direct and

indirect QDs, clearly shows the suppression of the electron-hole exchange interaction for indirect band-gap excitons, when the conduction band minimum shifts from the Γ to the X point for a specific QD size. As the exchange interaction splits and mixes the pure exciton spin states, its suppression is reflected in the occurrence of optical orientation of the exciton spin and in the strong decrease of the exchange splitting at the ΓX mixing energy.

Four different depolarization mechanisms, which reduce the optical orientation of the indirect exciton, were identified: Already in the Γ valley the spin polarization is lowered by the decoherence of the linearly polarized exciton states. The hyperfine interaction between the Γ electron and the nuclei as well as the phonon assisted scattering from the Γ to the X valley cause additional depolarization. In the X valley, the electron is further exposed to the hyperfine interaction, where it experiences a different coupling to the Overhauser field than in the Γ valley. The impact of these effects strongly depends on the ΓX splitting, which turns out to be a crucial parameter for the optical orientation of indirect QD excitons. The influence of the direct state on the indirect excitons can also be seen in the thermal redistribution dynamics. Two complementary models are proposed and discussed. They describe the thermal activation of the direct excitons from the dark to the bright Γ states and the redistribution between direct and indirect exciton levels.

Moreover, time-resolved measurements with selective excitation of indirect QDs were successfully carried out for the first time. It turns out that the spin relaxation time of the indirect exciton in a moderate, longitudinal magnetic field is most likely determined by the spin dynamics between dark and bright states, which should be describable by the kinetic spin model. Another interesting perspective for future studies is the possibly long spin-coherence time of the indirect exciton state, indicated by the strong optical alignment, since the long-lasting coherence of two spin states is a key property in quantum technology.

8 Outlook

Although the findings of this thesis and previous works deliver already a detailed understanding of the indirect (In,Al)As/AlAs QD ensemble, some effects are not explained yet and the investigation of the underlying physical origins might complete the picture. One example is the impact of the optical orientation on the nuclear spin system and possible feedback mechanisms between nuclei and the indirect excitons, which is disregarded in this thesis. Two promising experimental approaches are presented in this section.

Splitting of the polarization recovery curve

The study of the hyperfine interaction via the PRC (Faraday) and Hanle (Voigt) curves of the X exciton exhibits an interesting temperature effect, which is shown in Fig. 8.1. The circular polarization degree ρ_c^+ of the X_{high} exciton is measured in the optical-orientation setting, like it is defined in Eq. (3.3). The excitation energy is $E_{\text{exc}} = 1.698$ eV. It was already discussed in Sec. 6.5.1 that the increase of the sample temperature above 30 K leads to the increase of the width of the Hanle curve, see Fig. 6.17 (b). However, the PRC was not studied in this context. Figure 8.1 shows that for $T = 10$ K (blue), the PRC curve is slightly unsymmetrical and shifted to negative magnetic fields. At 40 K (red) the curve broadens and splits. The effect reminds of the splitting of the Hanle curve in oblique fields [67]. However, this model can not be applied to the present finding. Since the splitting appears at the temperature at which the spin lifetime is equal to the Larmor frequency in the nuclear field, see Fig. 6.17 (b), a spin-resonance effect as described in Ref. [108] might be a possible explanation.

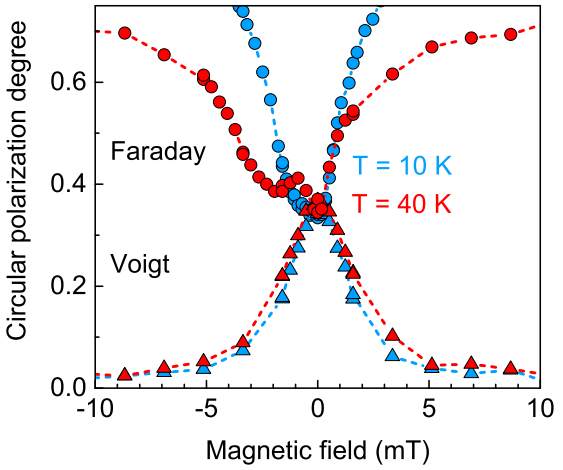

Figure 8.1: PRC (dots) and Hanle curves (triangles) measured for the X_{high} exciton at two different temperatures. Dashed lines are guides for the eye.

Induced circular polarization in weak magnetic fields

The high optical orientation degree of indirect excitons in steady-state experiments is caused by the fact that the spin relaxation time is much longer than the exciton recombination time. This relation is confirmed for the indirect excitons by time resolved

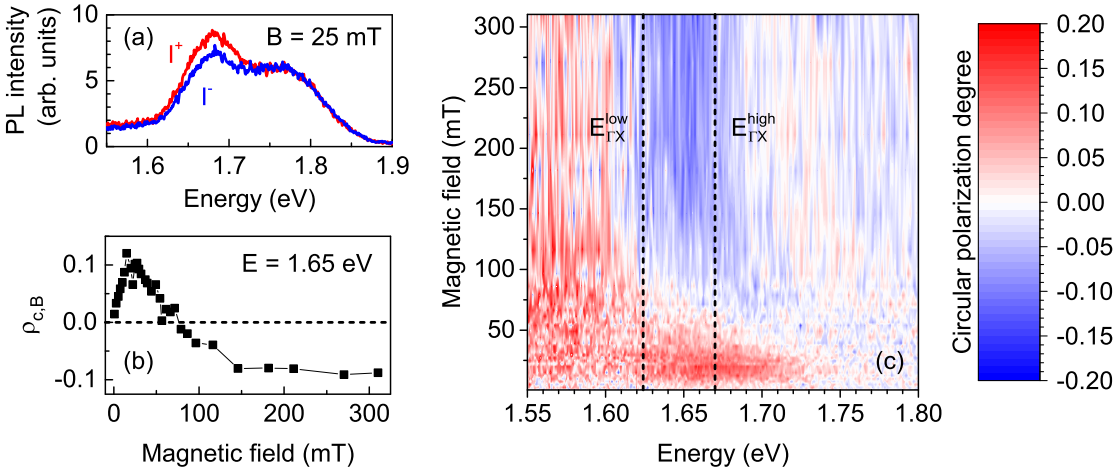

Figure 8.2: **(a)** Circularly polarized PL spectra under pulsed, nonresonant excitation, measured at $B = 25$ mT (Faraday). **(b)** Magnetic field dependence of the circular polarization degree, measured at $E = 1.65$ eV. **(c)** Circular polarization degree in dependence of the magnetic field strength and spectral energy. The dashed lines mark the ΓX transition energies. $T = 2$ K.

measurements in Sec. 6.6.2, revealing a factor of 50 for τ_s/τ_r. However, for delay times exceeding the spin relaxation time, magnetic field induced circular polarization $\rho_{c,B}$ is observable.

The circular polarization was measured under nonresonant, pulsed excitation with an integration time between 1 and 6 μs after the laser pulse. Small magnetic fields up to 300 mT are applied in Faraday geometry. The results are shown in Fig. 8.2. $\rho_{c,B}$ varies between -10 and 15% and shows changes of sign in dependence of the spectral energy and the magnetic field strength. On the spectral scale, the change of sign interferes with the ΓX-transition energy $E^{\text{low}}_{\Gamma X}$, see (c). For energies above $E^{\text{low}}_{\Gamma X}$, the change of sign occurs for magnetic field strengths between 25 and 100 mT. For energies below $E^{\text{low}}_{\Gamma X}$, the circular polarization degree shows no change of sign.

The nonmonotonic dependencies of the circular polarization degree on the spectral energy and the longitudinal magnetic field strength are not fully understand so far. However, the change of sign with increasing field strength in (b) is probably connected with the hyperfine interaction between the Γ electron and the nuclei, since it occurs for fields between 25 and 100 mT, which agrees well with the widths of the related polarization curves in Sec. 6.5.4, see blue symbols in Fig. 6.22 (a). Thus, the unusual spin dynamics might be related to the dynamical nuclear polarization, which has not been considered in this thesis. This effect becomes relevant for delay times that exceed the characteristic times of the nuclear spin dynamics [22].

Bibliography

[1] M. Grundmann, *The Physics of Semiconductors*, Third Edition, DOI: 10.1007/978-3-319-23880-7 (Springer International Publishing, 2016).

[2] T. J. Seebeck, "Über die magnetische Polarisation der Metalle und Erze durch Temperatur-Differenz", Annalen der Physik **82**, 1–20 (1826).

[3] M. Faraday, "XX. Experimental researches in electricity.— fourth series", Philosophical Transactions of the Royal Society of London, 507–522 (1833).

[4] F. Bloch, "Über die Quantenmechanik der Elektronen in Kristallgittern", Zeitschrift für Physik **52**, 555–600 (1929).

[5] R. Kronig and W. G. Penney, "Quantum mechanics of electrons in crystal lattices", Proceedings of the Royal Society of London. Series A **130**, 499–513 (1931).

[6] M. I. Dyakonov, ed., *Spin Physics in Semiconductors*, DOI: 10.1007/978-3-319-65436-2 (Springer International Publishing, 2017).

[7] T. Schäpers, *Semiconductor Spintronics*, DOI: 10.1515/9783110425444 (De Gruyter, 2016).

[8] D. Bimberg, ed., *Semiconductor Nanostructures*, DOI: 10.1007/978-3-540-77899-8 (Springer Berlin Heidelberg, 2008).

[9] F. Henneberger and O. Benson, eds., *Semiconductor Quantum Bits*, ISBN: 9789814241199 (Taylor and Francis Ltd., Apr. 19, 2016), 516 pp.

[10] A. V. Khaetskii and Y. V. Nazarov, "Spin relaxation in semiconductor quantum dots", Physical Review B **61**, 12639–12642 (2000).

[11] A. V. Khaetskii and Y. V. Nazarov, "Spin-flip transitions between Zeeman sublevels in semiconductor quantum dots", Physical Review B **64**, 125316 (2001).

[12] R. Cingolani and K. Ploog, "Frequency and density dependent radiative recombination processes in III-V semiconductor quantum wells and superlattices", Advances in Physics **40**, 535–623 (1991).

[13] T. S. Shamirzaev, A. M. Gilinsky, A. K. Bakarov, A. I. Toropov, D. A. Ténné, K. S. Zhuravlev, C. von Borczyskowski, and D. R. T. Zahn, "Millisecond photoluminescence kinetics in a system of direct-bandgap InAs quantum dots in an AlAs matrix", Journal of Experimental and Theoretical Physics Letters **77**, 389–392 (2003).

[14] T. S. Shamirzaev, A. M. Gilinsky, A. K. Kalagin, A. V. Nenashev, and K. S. Zhuravlev, "Energy spectrum and structure of thin pseudomorphic InAs quantum wells in an AlAs matrix: Photoluminescence spectra and band-structure calculations", Physical Review B **76**, 155309 (2007).

[15] V. V. Mitin, D. I. Sementsov, and N. Z. Vagidov, *Quantum Mechanics for Nanostructures*, ISBN: 0521763665 (Cambridge University Press, Jan. 8, 2018), 448 pp.

[16]N. Włodzimierz, "Effective masses of electrons and heavy holes in GaAs, InAs, AlAs and their ternary compounds", Physica B: Condensed Matter **210**, 1–25 (1995).

[17]R. Braunstein and E. O. Kane, "The valence band structure of the III-V compounds", Journal of Physics and Chemistry of Solids **23**, 1423–1431 (1962).

[18]M. Bayer, G. Ortner, O. Stern, A. Kuther, A. A. Gorbunov, A. Forchel, P. Hawrylak, S. Fafard, K. Hinzer, T. L. Reinecke, S. N. Walck, J. P. Reithmaier, F. Klopf, and F. Schäfer, "Fine structure of neutral and charged excitons in self-assembled In(Ga)As/(Al)GaAs quantum dots", Physical Review B **65**, 195315 (2002).

[19]R. Winkler, *Spin-orbit Coupling Effects in Two-dimensional Electron and Hole Systems*, ISBN: 3540011870 (Springer-Verlag GmbH, Oct. 10, 2003).

[20]G. E. W. Bauer and T. Ando, "Exciton mixing in quantum wells", Physical Review B **38**, 6015–6030 (1988).

[21]G. E. Pikus and F. G. Pikus, "The mechanism of heavy and light hole mixing in GaAs/AlAs superlattices", Solid State Communications **89**, 319–322 (1994).

[22]M. M. Glazov, *Electron and nuclear spin dynamics in semiconductor nanostructures*, ISBN: 9780198807308 (Oxford University Press, Oxford New York, NY, 2018).

[23]W. Nolting, *Theoretical Physics 7*, DOI: 10.1007/978-3-319-63324-4 (Springer International Publishing, 2017).

[24]C. Klingshirn, *Semiconductor Optics* (Springer Berlin Heidelberg, 2007).

[25]A. Zrenner, P. Leeb, J. Schäfer, G. Böhm, G. Weimann, J. M. Worlock, L. T. Florez, and J. P. Harbison, "Indirect excitons in coupled quantum well structures", Surface Science **263**, 496–501 (1992).

[26]T. S. Shamirzaev, A. V. Nenashev, A. K. Gutakovskii, A. K. Kalagin, K. S. Zhuravlev, M. Larsson, and P. O. Holtz, "Atomic and energy structure of InAs/AlAs quantum dots", Physical Review B **78**, 085323 (2008).

[27]T. S. Shamirzaev, D. S. Abramkin, A. V. Nenashev, K. S. Zhuravlev, F. Trojánek, B. Dzurňák, and P. Malý, "Carrier dynamics in InAs/AlAs quantum dots: lack in carrier transfer from wetting layer to quantum dots", Nanotechnology **21**, 155703 (2010).

[28]T. S. Shamirzaev, J. Debus, D. S. Abramkin, D. Dunker, D. R. Yakovlev, D. V. Dmitriev, A. K. Gutakovskii, L. S. Braginsky, K. S. Zhuravlev, and M. Bayer, "Exciton recombination dynamics in an ensemble of (In,Al)As/AlAs quantum dots with indirect band-gap and type-I band alignment", Physical Review B **84**, 155318 (2011).

[29]J. Debus, T. S. Shamirzaev, D. Dunker, V. F. Sapega, E. L. Ivchenko, D. R. Yakovlev, A. I. Toropov, and M. Bayer, "Spin-flip Raman scattering of the Γ-X mixed exciton in indirect band gap (In,Al)As/AlAs quantum dots", Physical Review B **90**, 125431 (2014).

[30]G. E. Pikus and G. L. Bir, "Exchange interaction in excitons in semiconductors", Sov. Phys. JETP **33**, 108 (1971).

[31]T. S. Shamirzaev, J. Debus, D. R. Yakovlev, M. M. Glazov, E. L. Ivchenko, and M. Bayer, "Dynamics of exciton recombination in strong magnetic fields in ultrathin GaAs/AlAs quantum wells with indirect band gap and type-II band alignment", Physical Review B **94**, 045411 (2016).

[32]P. Dawson, K. J. Moore, C. T. Foxon, G. W. 't. Hooft, and R. P. M. van Hal, "Photoluminescence decay time studies of type II GaAs/AlAs quantum-well structures", Journal of Applied Physics **65**, 3606–3609 (1989).

[33]M. Maaref, F. F. Charfi, D. Scalbert, C. B. à la Guillaume, and R. Planel, "Recombination Processes in Short-Period GaAs/AlAs Superlattices of Type II", physica status solidi (b) **170**, 637–651 (1992).

[34]F. Hatami, M. Grundmann, N. N. Ledentsov, F. Heinrichsdorff, R. Heitz, J. Böhrer, D. Bimberg, S. S. Ruvimov, P. Werner, V. M. Ustinov, P. S. Kop'ev, and Z. I. Alferov, "Carrier dynamics in type-II GaSb/GaAs quantum dots", Physical Review B **57**, 4635–4641 (1998).

[35]A. F. van Driel, G. Allan, C. Delerue, P. Lodahl, W. L. Vos, and D. Vanmaekelbergh, "Frequency-Dependent Spontaneous Emission Rate from CdSe and CdTe Nanocrystals: Influence of Dark States", Physical Review Letters **95**, 236804 (2005).

[36]T. Berstermann, T. Auer, H. Kurtze, M. Schwab, D. R. Yakovlev, M. Bayer, J. Wiersig, C. Gies, F. Jahnke, D. Reuter, and A. D. Wieck, "Systematic study of carrier correlations in the electron-hole recombination dynamics of quantum dots", Physical Review B **76**, 165318 (2007).

[37]A. F. van Driel, I. S. Nikolaev, P. Vergeer, P. Lodahl, D. Vanmaekelbergh, and W. L. Vos, "Statistical analysis of time-resolved emission from ensembles of semiconductor quantum dots: Interpretation of exponential decay models", Physical Review B **75**, 035329 (2007).

[38]T. Bartel, M. Dworzak, M. Strassburg, A. Hoffmann, A. Strittmatter, and D. Bimberg, "Recombination dynamics of localized excitons in InGaN quantum dots", Applied Physics Letters **85**, 1946–1948 (2004).

[39]T. S. Shamirzaev, A. V. Nenashev, and K. S. Zhuravlev, "Coexistence of direct and indirect band structures in arrays of InAs/AlAs quantum dots", Applied Physics Letters **92**, 213101 (2008).

[40]X. Chen, B. Henderson, and K. P. O'Donnell, "Luminescence decay in disordered low-dimensional semiconductors", Applied Physics Letters **60**, 2672–2674 (1992).

[41]R. Kohlrausch, "Theorie des elektrischen Rückstandes in der Leidener Flasche", Annalen der Physik und Chemie **167**, 179–214 (1854).

[42]T. S. Shamirzaev, J. Rautert, D. R. Yakovlev, J. Debus, A. Y. Gornov, M. M. Glazov, E. L. Ivchenko, and M. Bayer, "Spin dynamics and magnetic field induced polarization of excitons in ultrathin GaAs/AlAs quantum wells with indirect band gap and type-II band alignment", Physical Review B **96**, 035302 (2017).

[43]T. S. Shamirzaev, J. Rautert, D. R. Yakovlev, M. M. Glazov, and M. Bayer, "Intrinsic and magnetic-field-induced linear polarization of excitons in ultrathin indirect-gap type-II GaAs/AlAs quantum wells", Physical Review B **99**, 155301 (2019).

[44]G. L. Bir and G. E. Pikus, *Symmetry and strain-induced effects in semiconductors*, ISBN: 9780470073216 (Wiley, New York, 1974).

[45]E. L. Ivchenko, *Optical Spectroscopy of Semiconductor Nanostructures*, ISBN: 9781842 651506 (Alpha Science, Harrow, U.K, 2005).

[46]I. Vurgaftman, J. R. Meyer, and L. R. Ram-Mohan, "Band parameters for III-V compound semiconductors and their alloys", Journal of Applied Physics **89**, 5815 (2001).

[47]I. A. Yugova, A. Greilich, D. R. Yakovlev, A. A. Kiselev, M. Bayer, V. V. Petrov, Y. K. Dolgikh, D. Reuter, and A. D. Wieck, "Universal behavior of the electron g factor in GaAs/$Al_xGa_{1-x}As$ quantum wells", Physical Review B **75**, 245302 (2007).

[48]X. Marie, T. Amand, P. L. Jeune, M. Paillard, P. Renucci, L. E. Golub, V. D. Dymnikov, and E. L. Ivchenko, "Hole spin quantum beats in quantum-well structures", Physical Review B **60**, 5811 (1999).

[49]D. Pines, J. Bardeen, and C. P. Slichter, "Nuclear Polarization and Impurity-State Spin Relaxation Processes in Silicon", Physical Review **106**, 489–498 (1957).

[50]L. M. Woods, T. L. Reinecke, and Y. Lyanda-Geller, "Spin relaxation in quantum dots", Physical Review B **66**, 161318 (2002).

[51]X. Linpeng, T. Karin, M. V. Durnev, R. Barbour, M. M. Glazov, E. Y. Sherman, S. P. Watkins, S. Seto, and K.-M. C. Fu, "Longitudinal spin relaxation of donor-bound electrons in direct band-gap semiconductors", Physical Review B **94**, 125401 (2016).

[52]I. L. Aleiner and E. L. Ivchenko, "Anistropic exchange splittingin type II GaAs/AlAs superlattices", Pis'ma Zh. Eksp. Teor. Fiz. [JETP Lett.] **55**, 692 (1992).

[53]E. L. Ivchenko, A. Y. Kaminski, and U. Rössler, "Heavy-light hole mixing at zinc-blende (001) interfaces under normal incidence", Physical Review B **54**, 5852–5859 (1996).

[54]Y. G. Kusrayev, A. V. Koudinov, I. G. Aksyanov, B. P. Zakharchenya, T. Wojtowicz, G. Karczewski, and J. Kossut, "Extreme In-Plane Anisotropy of the Heavy-Hole g Factor in (001)-CdTe/CdMnTe Quantum Wells", Physical Review Letters **82**, 3176–3179 (1999).

[55]A. V. Koudinov, N. S. Averkiev, Y. G. Kusrayev, B. R. Namozov, B. P. Zakharchenya, D. Wolverson, J. J. Davies, T. Wojtowicz, G. Karczewski, and J. Kossut, "Linear polarization of the photoluminescence of quantum wells subject to in-plane magnetic fields", Physical Review B **74**, 195338 (2006).

[56]J. Singh, *Electronic and Optoelectronic Properties of Semiconductor Structures*, DOI: 10.1017/cbo9780511805745 (Cambridge University Press, 2003).

[57]M. S. Kuznetsova, J. Rautert, K. V. Kavokin, D. S. Smirnov, D. R. Yakovlev, A. K. Bakarov, A. K. Gutakovskii, T. S. Shamirzaev, and M. Bayer, "Electron-nuclei interaction in the X valley of (In,Al)As/AlAs quantum dots", Physical Review B **101**, 075412 (2020).

[58]A. Abragam, *The Principles of Nuclear Magnetism*, ISBN: 019852014X (Oxford University Press, 1961).

[59]E. I. Gryncharova and V. I. Perel, "Relaxation of nuclear spins interacting with holes in semiconductors", Sov. Phys. Semicond. **11**, 997 (1977).

[60]I. D. Avdeev and D. S. Smirnov, "Hyperfine interaction in atomically thin transition metal dichalcogenides", Nanoscale Advances **1**, 2624 (2019).

[61] A. V. Shchepetilnikov, D. D. Frolov, Y. A. Nefyodov, I. V. Kukushkin, D. S. Smirnov, L. Tiemann, C. Reichl, W. Dietsche, and W. Wegscheider, "Nuclear magnetic resonance and nuclear spin relaxation in AlAs quantum well probed by ESR", Physical Review B **94**, 241302 (2016).

[62] P. Blaha, K. Schwarz, G. Madsen, D. Kvaniscka, and J. Luitz, *WIEN2k An Augmented Plane Wave Plus Local Orbitals Program for Calculating Crystal Properties* (Vienna University of Technology, Vienna, 2001).

[63] E. A. Chekhovich, A. Ulhaq, E. Zallo, F. Ding, O. G. Schmidt, and M. S. Skolnick, "Measurement of the spin temperature of optically cooled nuclei and GaAs hyperfine constants in GaAs/AlGaAs quantum dots", Nature Materials **16**, 982 (2017).

[64] I. A. Merkulov, A. L. Efros, and M. Rosen, "Electron spin relaxation by nuclei in semiconductor quantum dots", Physical Review B **65**, 205309 (2002).

[65] This relation was determined in a discussion with D. S. Smirnov, who developed the microscopic model.

[66] D. H. Goldstein, *Polarized Light*, ISBN: 143983041X (Taylor and Francis Ltd., Dec. 19, 2017), 808 pp.

[67] F. Meier and B. P. Zakharchenya, *Optical Orientation*, ISBN: 0444867414 (North-Holland Sole distributors for the U.S.A. and Canada, Elsevier Science Pub. Co, Amsterdam New York New York, 1984).

[68] M. P. Fontana and D. B. Fitchen, "Magnetic Circular Polarization of F-Center Emission", Physical Review Letters **23**, 1497–1499 (1969).

[69] C. Zhang, D. Sun, Z.-G. Yu, C.-X. Sheng, S. McGill, D. Semenov, and Z. V. Vardeny, "Field-induced spin splitting and anomalous photoluminescence circular polarization in $CH_3NH_3PbI_3$ films at high magnetic field", Physical Review B **97**, 134412 (2018).

[70] D. Dunker, "Recombination and spin dynamics of excitons in indirect (In,Al)As/AlAs quantum dots", DOI: 10.17877/DE290R-15149, PhD thesis (Technical University of Dortmund, 2013).

[71] E. Finkman, M. D. Sturge, and M. C. Tamargo, "X-point excitons in AlAs/GaAs superlattices", Applied Physics Letters **49**, 1299–1301 (1986).

[72] G. Danan, B. Etienne, F. Mollot, R. Planel, A. M. Jean-Louis, F. Alexandre, B. Jusserand, G. L. Roux, J. Y. Marzin, H. Savary, and B. Sermage, "Optical evidence of the direct-to-indirect-gap transition in GaAs-AlAs short-period superlattices", Physical Review B **35**, 6207–6212 (1987).

[73] K. J. Moore, P. Dawson, and C. T. Foxon, "Effects of electronic coupling on the band alignment of thin GaAs/AlAs quantum-well structures", Physical Review B **38**, 3368–3374 (1988).

[74] P. Dawson, C. T. Foxon, and H. W. van Kesteren, "Nature of the lowest confined electron state in GaAs/AlAs type II quantum wells as a function of AlAs thickness", Semiconductor Science and Technology **5**, 54–59 (1990).

[75] D. Scalbert, J. Cernogora, C. B. à. Guillaume, M. Maaref, F. F. Charfi, and R. Planel, "Nature of the lowest electron states in short period GaAs-AlAs superlattices of type II", Solid State Communications **70**, 945–949 (1989).

[76]L. P. Fu, F. T. Bacalzo, G. D. Gilliland, R. Chen, K. K. Bajaj, J. Klem, and D. J. Wolford, "Microscopic mechanisms governing exciton-decay kinetics in type-II GaAs/AlAs superlattices", Physical Review B **52**, 2682–2687 (1995).

[77]W. A. J. A. van der Poel, A. L. G. J. Severens, H. W. van Kesteren, and C. T. Foxon, "Spin relaxation in type-II GaAs/AlAs quantum wells", Physical Review B **39**, 8552–8555 (1989).

[78]H. W. van Kesteren, E. C. Cosman, W. A. J. A. van der Poel, and C. T. Foxon, "Fine structure of excitons in type-II GaAs/AlAs quantum wells", Physical Review B **41**, 5283–5292 (1990).

[79]C. Gourdon and P. Lavallard, "Fine structure of heavy excitons in GaAs/AlAs superlattices", Physical Review B **46**, 4644–4650 (1992).

[80]I. V. Mashkov, C. Gourdon, P. Lavallard, and D. Y. Roditchev, "Exciton quantum beats in type-II GaAs/AlAs superlattices in longitudinal and in-plane magnetic fields", Physical Review B **55**, 13761–13770 (1997).

[81]R. I. Dzhioev, H. M. Gibbs, E. L. Ivchenko, G. Khitrova, V. L. Korenev, M. N. Tkachuk, and B. P. Zakharchenya, "Determination of interface preference by observation of linear-to-circular polarization conversion under optical orientation of excitons in type-II GaAs/AlAs superlattices", Physical Review B **56**, 13405–13413 (1997).

[82]O. Madelung, ed., *Physics of Group IV Elements and III-V Compounds*, ISBN: 9783540106104 (Springer-Verlag, Berlin New York, 1982).

[83]D. S. Abramkin, A. K. Gutakovskii, and T. S. Shamirzaev, "Heterostructures with diffused interfaces: Luminescent technique for ascertainment of band alignment type", Journal of Applied Physics **123**, 115701 (2018).

[84]P. Dawson, Z. Ma, K. Pierz, and E. O. Göbel, "Microsecond carrier recombination times in InAs/AlAs quantum dots", Applied Physics Letters **81**, 2349 (2002).

[85]P. Dawson, E. O. Göbel, and K. Pierz, "Spectroscopy and recombination dynamics of InAs/AlAs quantum dots", Journal of Applied Physics **98**, 013541 (2005).

[86]T. S. Shamirzaev, K. S. Zhuravlev, M. Larsson, and P. O. Holtz, "Photoluminescence of a single InAs/AlAs quantum dot", Phys. Status Solidi (C) **5**, 2528 (2008).

[87]J.-W. Luo, A. Franceschetti, and A. Zunger, "Quantum-size-induced electronic transitions in quantum dots: Indirect band-gap GaAs", Physical Review B **78**, 035306 (2008).

[88]J. Debus, "Spin-flip Raman scattering in low dimensional semiconductors", DOI: 10.17877/DE290R-14291, PhD thesis (Technical University of Dortmund, 2012).

[89]M. Nirmal, D. J. Norris, M. Kuno, M. G. Bawendi, A. L. Efros, and M. Rosen, "Observation of the "Dark Exciton" in CdSe Quantum Dots", Physical Review Letters **75**, 3728–3731 (1995).

[90]L. Biadala, E. V. Shornikova, A. V. Rodina, D. R. Yakovlev, B. Siebers, T. Aubert, M. Nasilowski, Z. Hens, B. Dubertret, A. L. Efros, and M. Bayer, "Magnetic polaron on dangling-bond spins in CdSe colloidal nanocrystals", Nature Nanotechnology **12**, 569–574 (2017).

[91]V. Y. Ivanov, T. S. Shamirzaev, D. R. Yakovlev, A. K. Gutakovskii, Ł. Owczarczyk, and M. Bayer, "Optically detected magnetic resonance of photoexcited electrons in (In,Al)As/AlAs quantum dots with indirect band gap and type-I band alignment", Physical Review B **97**, 245306 (2018).

[92]M. Kroutvar, Y. Ducommun, D. Heiss, M. Bichler, D. Schuh, G. Abstreiter, and J. J. Finley, "Optically programmable electron spin memory using semiconductor quantum dots", Nature **432**, 81–84 (2004).

[93]J. L. Cheng, M. W. Wu, and C. Lü, "Spin relaxation in GaAs quantum dots", Physical Review B **69**, 115318 (2004).

[94]D. Keller, D. R. Yakovlev, B. König, W. Ossau, T. Gruber, A. Waag, L. W. Molenkamp, and A. V. Scherbakov, "Heating of the magnetic ion system in (Zn, Mn)Se/(Zn, Be)Se semimagnetic quantum wells by means of photoexcitation", Physical Review B **65**, 035313 (2001).

[95]U. Rössler, S. Jorda, and D. Broido, "Fine structure of quantum well excitons", Solid State Communications **73**, 209–214 (1990).

[96]P. G. Baranov, I. V. Mashkov, N. G. Romanov, P. Lavallard, and R. Planel, "Optically detected magnetic resonance of excitons and carriers in pseudodirect GaAs/AlAs superlattices", Solid State Communications **87**, 649–654 (1993).

[97]I. A. Ostapenko, G. Hönig, S. Rodt, A. Schliwa, A. Hoffmann, D. Bimberg, M.-R. Dachner, M. Richter, A. Knorr, S. Kako, and Y. Arakawa, "Exciton acoustic-phonon coupling in single GaN/AlN quantum dots", Physical Review B **85**, 081303 (2012).

[98]M. Gurioli, A. Vinattieri, M. Colocci, C. Deparis, J. Massies, G. Neu, A. Bosacchi, and S. Franchi, "Temperature dependence of the radiative and nonradiative recombination time in GaAs/$Al_xGa_{1-x}As$ quantum-well structures", Physical Review B **44**, 3115–3124 (1991).

[99]C. de Mello Donegá, M. Bode, and A. Meijerink, "Size- and temperature-dependence of exciton lifetimes in CdSe quantum dots", Physical Review B **74**, 085320 (2006).

[100]M.-Z. Huang and W. Y. Ching, "A minimal basis semi-ab initio approach to the band structures of semiconductors", Journal of Physics and Chemistry of Solids **46**, 977–995 (1985).

[101]D. Gammon, E. S. Snow, B. V. Shanabrook, D. S. Katzer, and D. Park, "Fine Structure Splitting in the Optical Spectra of Single GaAs Quantum Dots", Physical Review Letters **76**, 3005–3008 (1996).

[102]E. L. Ivchenko, "Fine Structure of Excitonic Levels in Semiconductor Nanostructures", physica status solidi (a) **164**, 487–492 (1997).

[103]M. Paillard, X. Marie, P. Renucci, T. Amand, A. Jbeli, and J. M. Gérard, "Spin Relaxation Quenching in Semiconductor Quantum Dots", Physical Review Letters **86**, 1634–1637 (2001).

[104]A. V. Khaetskii, D. Loss, and L. Glazman, "Electron Spin Decoherence in Quantum Dots due to Interaction with Nuclei", Physical Review Letters **88**, 186802 (2002).

[105]R. Seguin, A. Schliwa, S. Rodt, K. Pötschke, U. W. Pohl, and D. Bimberg, "Size-Dependent Fine-Structure Splitting in Self-Organized InAs/GaAs Quantum Dots", Physical Review Letters **95**, 257402 (2005).

[106]E. A. Chekhovich, M. N. Makhonin, A. I. Tartakovskii, A. Yacoby, H. Bluhm, K. C. Nowack, and L. M. K. Vandersypen, "Nuclear spin effects in semiconductor quantum dots", Nature Materials **12**, 494–504 (2013).

[107]B. Urbaszek, X. Marie, T. Amand, O. Krebs, P. Voisin, P. Maletinsky, A. Högele, and A. Imamoglu, "Nuclear spin physics in quantum dots: An optical investigation", Reviews of Modern Physics **85**, 79–133 (2013).

[108]P. Schering, G. S. Uhrig, and D. S. Smirnov, "Spin inertia and polarization recovery in quantum dots: Role of pumping strength and resonant spin amplification", Physical Review Research **1**, 033189 (2019).

[109]M. W. Wu, J. H. Jiang, and M. Q. Weng, "Spin dynamics in semiconductors", Physics Reports **493**, 61–236 (2010).

[110]S. Blundell, *Magnetism in condensed matter*, ISBN: 9780198505921 (Oxford University Press, Oxford New York, 2001).

[111]J. Fischer, W. A. Coish, D. V. Bulaev, and D. Loss, "Spin decoherence of a heavy hole coupled to nuclear spins in a quantum dot", Physical Review B **78**, 155329 (2008).

[112]Y. G. Kusrayev, B. R. Namozov, I. V. Sedova, and S. V. Ivanov, "Optically induced spin polarization and g-factor anisotropy of holes in CdSe/ZnSe quantum dots", Physical Review B **76**, 153307 (2007).

[113]V. I. Klimov, A. A. Mikhailovsky, D. W. McBranch, C. A. Leatherdale, and M. G. Bawendi, "Mechanisms for intraband energy relaxation in semiconductor quantum dots: The role of electron-hole interactions", Physical Review B **61**, 13349–13352 (2000).

Symbols and Abbreviations

a	Lattice constant
A	Hyperfine coupling constant
AG 2890	Quantum dot sample (multi layer)
α	Boltzmann factor for the electron spin flip
Al	Aluminum
As	Arsenic
a.u.	Arbitrary units
a_X	Slope of the indirect exciton energy with increasing excitation energy
b	Bright
B, $\boldsymbol{B}$	Magnetic field strength, magnetic field vector
$B_{1/2}$	Half width at half maximum of a polarization curve
β	Boltzmann factor for the heavy hole spin flip
$B_{\max}$	Magnetic field of maximal circular polarization
B_{N}	Effective nuclear field
C	Angle depended coefficient
C_{2v}	Point group
CB	Conduction band
CCD	Charge-coupled device
C_{d}	Radiative contribution of dark excitons
cw	Continuous wave
d	Dark
d	Thickness of the diffused layer in heterostructures
D (line)	Acoustic phonon replica of the direct exciton recombination
D	Angle depended coefficient
$\mathcal{D}(\mathbf{r})$	Orbital function
D_{2d}	Point group
δ_0	Isotropic electron-hole exchange splitting between dark and bright exciton states
δ_1	Anisotropic electron-hole exchange splitting (bright exciton states)
δ_2	Isotropic electron-hole exchange splitting (dark exciton states)
Δ_α	Relative hyperfine coupling constant ($\alpha = x, y, z$)
Δ_{i}	Zeeman splitting (i = electron, hole)
Δ_{so}	Split-off energy
$\Delta E_{\Gamma X}$	Energetic splitting between the Γ and the X valley in a quantum dot

e	electron
E	Energy; Electric field
E_g	Band gap
ε	Hyperfine-anisotropy factor
Ex	Exciton
E_exc	Excitation energy or laser energy
E_exch	Exchange energy
$E_{\Gamma X}$	Transition energy between direct and indirect quantum dots
E_Z	Zeeman splitting
f	Occupancy of a spin level
FWHM	Full width at half maximum
g	g factor or Landé factor
G, $\tilde{G}$	Generation rate, effective generation rate
Ga	Gallium
γ	Characteristic parameter of the Distribution function
Γ	Symmetry point of the Brillouin zone
$G(\tau_\mathrm{r})$	Distribution of exciton recombination times
h	hole
h	Planck constant, $4.136 \cdot 10^{-16}$ eVs
$\hbar$	Reduced Planck constant, $6.582 \cdot 10^{-16}$ eVs
H	Height of circular polarization curve $\rho_\mathrm{c}(B)$
$\hat{\mathcal{H}}$	Spin Hamiltonian
$\mathcal{H}_\mathrm{hf}$	Hyperfine Hamiltonian
hh	heavy hole
HWHM	Half width at half maximum
H_Z	Zeeman Hamiltonian
I	Intensity of the photoluminescence; Nuclear spin
In	Indium
j	Total angular momentum
k	Wave vector
k_B	Boltzmann constant, $8.617 \cdot 10^{-5}$ eV/K
l	Orbital angular momentum
L	Thickness of a quantum well or quantum dot
λ_dB	de Broglie wavelength
LO	Longitudinal optical phonon
m_0	Free electron mass, $9.109 \cdot 10^{-31}$ kg
m, m_j, m_s	Projections of the angular momentum along z

m^*	Effective mass
MCA	Multichannel analyzer
μ_B	Bohr magneton, $5.788 \cdot 10^{-5}$ eV/T
μPL	Microphotoluminescence
n	Radial quantum number
N	Number of nuclei interacting with an electron
Nd:YVO_4	Neodymium-doped yttrium orthovanadate
n_e, n_o	Index of refraction of the extraordinary and ordinary beam
NP	No-phonon line
nr	nonradiative
NR (band)	Photoluminescence of unknown source
ω	Angular velocity
Ω	Larmor precession frequency
OPA	Optical parametric amplifier
p	Momentum
$\mathcal{P}(\mathbf{r})$	Orbital function
PL	Photoluminescence
φ	Angle between the optical axis of a half-wave plate and the direction of the electrical field
PMT	Photomultiplier tube
PRC	Polarization recovery curve
Ψ	Wave function
QD	Quantum dot
QW	Quantum well
$\boldsymbol{r}$	Vector between nucleus and electron
R	Recombination operator
rad	Radiative
RC 1517	Quantum dot sample (single layer)
Ref.	Reference
ρ, ρ_z	Polarization degree
ρ^0	Initial polarization of carriers
ρ_0	Restored circular polarization degree
ρ_c	Circular polarization degree
$\rho_{\mathrm{c},B}$	Magnetic field induced circular polarization degree
ρ_i	Initial polarization degree
ρ_int	Intrinsic polarization degree
ρ_l	Linear polarization degree
ρ_oa	Optical alignment degree
ρ_oo	Optical orientation degree
s	Spin quantum number
$\mathcal{S}(\mathbf{r})$	Orbital function

S_{low}, S_{high}	Static PL features
Sec.	Section
σ	Pauli spin matrix
σ^+, σ^-	Right- and left-handed circular polarization
t	Time
t_{delay}	Delay time (after laser pulse)
t_{gate}	Exposure time
T	Temperature
TA	Transverse acoustic phonon
τ_0	Average exciton recombination time
τ_d	Decoherence time
τ_r	Exciton recombination time or lifetime
τ_{rad}	Radiative recombination time
τ_{nr}	Nonradiative recombination time
τ_s	Spin relaxation or spin-flip time
T_g	Growth temperature
θ	Angle between magnetic field direction and growth axis
Ti	Titanium
T_s	Spin lifetime
V	Quantum dot volume
V_0	Volume of the primitive cell
VB	Valence band
w, w'	Radiative and nonradiative recombination rates
w_e, w_h	Spin-flip rates of electron and hole
W	Spin-flip rate
x	Cartesian coordinate; Indium concentration
X	Symmetry point of the Brillouin zone
$\|X\rangle$	Linearly polarized state of the direct exciton
X_{low}, X_{high}	Indirect exciton
ξ	Depolarization factor
y	Cartesian coordinate
$\|Y\rangle$	Linearly polarized state of the direct exciton
z	Cartesian coordinate and growth axis
ZP	Zero-phonon line

List of publications

1) T. S. Shamirzaev, J. Rautert, D. R. Yakovlev, J. Debus, A. Yu. Gornov, M. M. Glazov, E. L. Ivchenko and M. Bayer, "Spin dynamics and magnetic field induced polarization of excitons in ultrathin GaAs/AlAs quantum wells with indirect band gap and type-II band alignment", Physical Review B **96**, 035302 (2017).

2) T. S. Shamirzaev, J. Rautert, D. R. Yakovlev, M. M. Glazov and M. Bayer, "Intrinsic and magnetic-field-induced linear polarization of excitons in ultrathin indirect-gap type-II GaAs/AlAs quantum wells", Physical Review B **99**, 155301 (2019).

3) J. Rautert, T. S. Shamirzaev, S. V. Nekrasov, D. R. Yakovlev, P. Klenovský, Yu. G. Kusrayev and M. Bayer, "Optical orientation and alignment of excitons in direct and indirect band gap (In,Al)As/AlAs quantum dots with type-I band alignment", Physical Review B **99**, 195411 (2019).

4) J. Rautert, M. V. Rakhlin, K. G. Belyaev, T. S. Shamirzaev, A. K. Bakarov, A. A. Toropov, I. S. Mukhin, D. R. Yakovlev and M. Bayer, "Anisotropic exchange splitting of excitons affected by ΓX mixing in (In,Al)As/AlAs quantum dots: Microphotoluminescence and macrophotoluminescence measurements", Physical Review B **100**, 205303 (2019).

5) M. S. Kuznetsova, J. Rautert, K. V. Kavokin, D. S. Smirnov, D. R. Yakovlev, A. K. Bakarov, A. K. Gutakovskii, T. S. Shamirzaev and M. Bayer, "Electron-nuclei interaction in the X valley of (In,Al)As/AlAs quantum dots", Physical Review B **101**, 075412 (2020).

Acknowledgments

Now it is the time to thank the people who contributed to this thesis.
I am grateful that I could spend my PhD time at the chair of *Prof. Manfred Bayer*, which offers excellent scientific conditions, a great working atmosphere and many opportunities to learn, travel and have fun.
I would like to thank my supervisor *Prof. Dmitri R. Yakovlev*, who, despite his many projects, always takes the time to patiently discuss or explain topics. Moreover, I thank my 'lab supervisor' *Prof. Timur S. Shamirzaev* for his contagious efficiency and energy, which resulted in many fruitful measurements during his stays in Dortmund. My work in the lab was also supported by *Dr. Dion Braukmann* and of course *Dr. Dennis Kudlacik*, whom I thank for his tremendous helpfulness.
A big part of the presented work was done at the Ioffe Institute in Saint Petersburg and I am happy that I had the opportunity to work at the chairs of *Prof. Yury G. Kusrayev* and *Prof. Alexey I. Toropov*, where I experienced a lot of hospitality. In particular, I would like to thank *Dr. Sergey V. Nekrasov* for his care and for being a great colleague during the four month we worked together. It was also a pleasure to sit in the darkness with *Dr. Maxim V. Rakhlin* and *Dr. Kirill G. Belyaev*, which turned out to be very efficient. During this time in Saint Petersburg I was lucky to live with *Dr. Felix Spitzer*, his girlfriend *Laura Fischer*, *Erik Kirstein* and *Dr. Matthias Salewski*. These are really great memories. Here, I also got to know *Dr. Demid S. Abramkin*, who played some rock song on his jaw harp the first day we met. With his enthusiasm and competence he was a great support for our little QD team.
For helpful discussions I would like to thank *Prof. Mikhail M. Glazov*, *Dr. Dmitry S. Smirnov*, *Dr. Maria S. Kuznetsova* and *Dr. Petr Klenovský*. Further, I thank *Dr. Jörg Debus*, who encouraged me to start at the 'E2' chair and who introduced me to my PhD topic.
All our experiments would not be possible without the constant supply of helium and advice from *Lars Wieschollek*, *Klaus Wiegers*, and *Daniel Tüttmann*. I think Lars and I can now disassemble the green cryostat blindfolded. Further thanks to *Thomas Stöhr* for fixing electrical problems and to *Michaela Wäscher*, *Nina Collette*, *Katharina Sparka* and *Manuela Maria Brück* for the administrative support.
I always had a great time with my office colleagues *Janina Schindler*, *Henning Moldenhauer* and *Eiko Evers* and with all other members of 'E2'. I will keep this time in very good memory!

Outside of university life, I would like to thank my mother *Edeltraud Rautert*, who taught me that girls can (almost) everything that boys can (and more) and I thank my father *Klaus Rautert* for sparking my interest in the coherences of nature. In this way, both of them contributed to this thesis. Finally, I thank my boyfriend *Dimitry Michejew*, whom I met on day one at the university and who has been by my side ever since.